Development of Soret Forced Rayleigh Scattering Apparatus to Measure Soret Coefficient in Binary and Ternary Liquid Mixtures

February 2019

Hiroaki Matsuura

A Thesis for the Degree of Ph.D. in Engineering

Development of Soret Forced Rayleigh Scattering Apparatus to Measure Soret Coefficient in Binary and Ternary Liquid Mixtures

Keio University

1858

CALAMVS GLADIO FORTIOR

February 2019

Graduate School of Science and Technology
Keio University

Hiroaki Matsuura

Contents

1. Introduction

2. Design and construction of instrument for ternary systems

List of Figures

List of Tables

Nomenclature

Roman symbols

a	Thermal diffusivity	$m^2 \cdot s^{-1}$
A	Amplitude factor for the diffracted light intensity	–
c_i	Mass fraction	–
C_p	Specific heat at constant pressure	$J \cdot kg^{-1} \cdot K^{-1}$
d	Length of optical path	m
D	Mass diffusion coefficient in binary mixtures	$m^2 \cdot s^{-1}$
D_{11}, D_{22}	Main diffusion coefficient in ternary mixtures	$m^2 \cdot s^{-1}$
D_{12}, D_{21}	Cross diffusion coefficient in ternary mixtures	$m^2 \cdot s^{-1}$
$\hat{D}_1, \hat{D}_2$	Diffusion eigenvalue	$m^2 \cdot s^{-1}$
$\mathbf{D}$	Diffusion matrix	–
$D_{T,i}$	Thermodiffusion coefficient	$m^2 \cdot s^{-1} \cdot K^{-1}$
$D'_{T,i}$	Thermodiffusion coefficient (containing concentration factor)	$m^2 \cdot s^{-1} \cdot K^{-1}$
D_{sq}	Amplitude factor for the scattered light intensity	–
g	Acceleration of gravity	$m \cdot s^{-2}$
I_i	Moment of inertia of component i	$kg \cdot m^2$
I_h	Intensity of heating laser	$W \cdot m^{-2}$
I_λ	Intensity of diffracted light	$W \cdot m^{-2}$
$\mathbf{J}_i$	Mass flux of component i	$kg \cdot m^{-2} \cdot s^{-1}$
J_λ	Heat flux	$W \cdot m^{-2}$
$\mathbf{J}'_q$	Net heat flux	$W \cdot m^{-2}$
L	Length	m
L_{ik}	Phenomenological coefficient	–
M_i	Molecular mass of component i	–
n_λ	Refractive index	–
$\mathbf{N_c}$	Refractive index matrix	–
$\partial n_\lambda / \partial c_i$	Optical contrast factor (concentration derivative)	–

$\partial n_\lambda/\partial T$	Optical contrast factor (temperature derivative)	K^{-1}
p	Pressure	Pa
$P'_{T,\lambda}$	Parameter related to thermodiffusion coefficient	$m^2 \cdot s^{-1} \cdot K^{-1}$
$P'_{S,\lambda}$	Parameter related to Soret coefficient	K^{-1}
q	Wavenumber	m^{-1}
Q'^*_i	Reduced heat of transport for component i	$J \cdot kg^{-1}$
$\mathbf{r}$	Position	–
R	Gas constant	$J \cdot K^{-1} \cdot mol^{-1}$
$S_{T,i}$	Soret coefficient	K^{-1}
$S'_{T,i}$	Soret coefficient (containing concentration factor)	K^{-1}
t	Time	s
t_0	Initial time	s
T	Temperature	K
$u(x)$	Standard uncertainty of x	–
$\mathbf{v}$	Velocity	$m \cdot s^{-1}$
V	Output voltage	V
W	Normalized weight	–
x_i	Mole fraction of component i	–
X_i	Thermodynamic forces	–

Greek symbols

α	Absorption coefficient	m^{-1}
β	Thermal expansion coefficient	K^{-1}
δ	Solubility parameter	$(MPa)^{1/2}$
η	Kinematic viscosity	$m^2 \cdot s^{-1}$
θ	Angle	rad
λ	Wavelength	m
Λ	Fringe spacing	m
μ	Chemical potential	$J \cdot mol^{-1}$
ρ	Density	$kg \cdot m^{-3}$

τ_a	Characteristic time of heat diffusion	s
τ_D	Characteristic time of mass diffusion	s
ψ	Phase difference	rad
ω	Beam spot size	m

Acknowledgments

First of all, I would like to express my appreciation to my advisor Prof. Yuji Nagasaka for his enthusiasm and support during my six years in his group. He has provided me the ideal environment for my research and I fortunately got the opportunity to find the excitement in experimental studies on thermophysical properties. I consider it a privilege to have been his student and it was an honor to be able to work with him.

I would also like to thank Prof. Yoshihiro Taguchi, for his selfless supports at all hours. In addition, I would like to express my appreciation to the other members of my thesis committee, Prof. Atsushi Nakajima, Prof. Kenji Yasuoka, for their valuable and helpful suggestions.

This thesis was only possible because of the super-talented colleagues with whom I had the opportunity to work and interact. I would like to thank Shintaro Iwaasa for his unlimited kindness to explain me all important things to start my research life. I am grateful to Masayuki Fujita, Daichi Tokuda, and Taichi Murai, who enjoyed experiments on diffusion projects together. The significant improvement of the experimental technique could not be realized without useful and stimulating discussions with them. I also would like to thank Takuya Hoshino and Ryohei Konno who kindly taught me how to use the infrared laser system.

I would like to express my regards to other members in our group, who always cheer me up. I am especially grateful to Kota Tomioka and Makoto Kamata, who worked together in our laboratory for six years.

Lastly I would like to thank my family for their support and encouragement. To my parents who sacrificed so much for my education, I cannot thank you enough.

1

Introduction

1.1 The Soret effect (thermodiffusion)

Mass transport phenomena play central roles in our daily lives and in engineering processes [1]. Diverse phenomena such as the transport in living cells, the efficiency of distillation, and dispersal of pollutants can be described using diffusion equations [1]. The Soret effect, also known as Ludwig-Soret effect, thermodiffusion, thermophoresis or thermal diffusion, describes mass transport flows driven by temperature gradients [2–4], whereas the driving force of the mass diffusion is the concentration gradient. The Soret effect which results from diffusion in a temperature gradient is an example of a cross-effect, in analogy with the thermo-electric effects known as Seebeck/Peltier effect [5]. The discovery of thermodiffusion was reported in a one-page paper by Ludwig in 1856 [6], which was just one year later after Fick presented the law of diffusion in 1855 [7]. After more than 20 years from the first observation by Ludwig, Soret reported more systematic studies on thermodiffusion in various salt solutions [8–10]. His name is attached to thermodiffusion due to his pioneering works and contributions, although Soret was probably not aware of the work of Ludwig, according to the short biography of Soret by Platten and Costesèque [11].

Although usually the Soret effect does not seem to be apparent to our eyes, this phenomenon can be significant depending on the spatial or time scale of the systems. One early application was the separation of uranium isotopes during World War II, using Clusius-Duckel columns [12,13]. In petroleum reservoirs, the Soret effect changes the oil compositions over geological time scales [14–16]. Also, isotope fractionation in silicate melts in magmatic systems is assumed to be associated with the Soret effect [17–21]. In addition, the Soret effect as well as the mass diffusion is considered to be important to design the solution casting processes to fabricate polymer films, where temperature and concentration distributions are formed in the casting solutions with micro-nano meter scale thickness [22,23]. As another interesting example,

1

the accumulation of the prebiotic molecules by the combination of the Soret effect and convection in hydrothermal pores in ancient sea might explain the unrevealed origin-of-life problem [24–28].

The Soret effect in liquid mixtures is still not well understood [2,3]. Thermodiffusion in gaseous mixtures can be described by the Chapman-Enskog theory [29–31], but this classical theory for gases cannot be applied to liquid systems where interactions make the description complexed [2,3]. Therefore, the experimental approach to the Soret effect is important for the understanding and applications. In the last twenty years, remarkable progress was made on binary systems, including the Fontainebleau benchmark campaign to provide reliable values for the Soret coefficient in binary organic mixtures [32]. Experiments were performed on the three binary mixtures of 1,2,3,4-tetrahydronaphthalene (THN), isobutylbenzene (IBB), and n-dodecane (nC12) with the mass fraction of 0.5 at a temperature of T = 298.15 K, by five groups using different methods including the holographic grating technique [33,34] and thermogravitational column technique [35–37]. From the result, the benchmark values of the Soret coefficient, thermodiffusion coefficient, and the mass diffusion coefficient were proposed. New techniques can refer to the benchmark values to confirm the validity. For example, the optical digital interferometry (ODI) [38], the optical beam deflection (OBD) [39], thermogravitational micro-column [40], thermogravitational micro-column applying digital interferometry technique [41] and the light scattering from non-equilibrium fluctuations [42] were validated by the measurement of the Fontainebleau benchmark systems. Experimental studies on binary systems lead to some interesting findings, including the change in signs of the Soret coefficient in water/alcohol mixtures [39,43], the molar mass independence of thermodiffusion in polymer solutions [44–46], the isotope Soret effect [47–51], and the concept of thermophobicity [52,53].

More recently, the research focus has shifted to ternary systems. Measurement of ternary mixtures is not straightforward, because there are two independent components and mass transport is described by six independent transport coefficients: four diffusion coefficients and two thermodiffusion coefficients. In mixtures composed of more than two components, the mass flux of one component is influenced by the concentration of other components (cross-diffusion) [54]. Due to the cross-diffusion, the flux of the first component can be accelerated by as much as an order of magnitude [54]. Because the liquids of practical interest usually contain more than two components, approach to ternary mixtures is important to understand mass transport phenomena in multicomponent systems.

The first systematic measurement of thermodiffusion in ternary systems was performed in 2005 on ternary hydrocarbon systems using the convective coupling technique of thermogravitational column (TGC) [55–57]. Subsequently, Köhler *et al.* [58,59] built the two-color optical beam deflection (OBD) instrument based on the two-color detection scheme proposed by Haugen and Firoozabadi [60]. Also, two-color optical experiments of the optical digital interferometry (ODI) technique by the Shevtsova group [61] were successfully carried out. These techniques contributed to the ternary benchmark campaign [62], which has been promoted within the framework of the DCMIX (diffusion coefficient measurements in mixtures) project [61,63,64]. The benchmark values of the Soret coefficient, thermodiffusion coefficinet, and diffusion eigenvalues were proposed in 2015 [62] for the ternary mixture of THN/IBB/nC12 with mass fractions of 0.8/0.1/0.1 at a temperature of $T = 298.15$ K. Themodiffusion coefficients and the Soret coefficients were measured under the ground conditions by the ODI [61], OBD [65], and TGC [66] technique. The four diffusion coefficients were measured by the Taylor dispersion (TD) technique [61], the open ended capillary (OEC) technique [67], and the sliding symmetric tubes (SST) technique [66]. The values of mass diffusion coefficient measured by TD were used to calculate thermodiffusion coefficient by ODI technique [61]. Also, Soret coefficient by TGC technique were determined using the values of mass diffusion coefficient by SST [66]. In addition to these ground experiments, the microgravity experiments to reduce the effect of the convection in the SODI (selectable optical diagnostic instrument) installation [61] were conducted and the raw interferometric images of ODI were analyzed independently by the four laboratories [61,67–69]. The Soret coefficient and thermodiffusion coefficient of THN/IBB/nC12 in a broader composition range were measured using TGC [70] and OBD [71].

Although the situation has significantly improved recently, experimental data for complex systems such as ternary mixtures are available for only particular systems. The understanding of the Soret effect is still limited and there is as yet no comprehensive microscopic description of the Soret effect in multicomponent liquid mixtures. Probably due to this lack of understanding, knowledge of the Soret effect is not widely utilized in industry, although the thermodiffusion can play dominant roles in some systems. This thesis deals with the development of the new instruments to measure the Soret coefficient in complex systems, with the aim to open up the option to gain broader knowledge of mass transport phenomena.

1.2 Soret coefficients in binary and ternary systems

1.2.1 Linear laws and phenomenological equations

The description of the mass transport including the Soret effect and the mass diffusion is dealt with the linear non-equilibrium thermodynamics. In the following, the relationship between the mass transport coefficients and the description based on the non-equilibrium thermodynamics by de Groot [5] is briefly outlined.

The Fick's law says that the mass flux is in proportion to the concentration gradient. Also, according to the Fourier's law, the heat flux is in proportion to the temperature gradient. On the other hand, the Soret effect describes the mass flux generated by the temperature gradient. The mass flux considering the Soret effect can be expressed empirically by adding a term concerning the temperature gradient to the equation of the Fick's law. Also, the heat flux considering the Dufour effect, which is known as the transport of heat by the concentration gradient, can be described by adding a term of the concentration gradient to the Fourier's law. These empirical formula can be generalized to be the following phenomenological relation (linear laws) concerning the independent fluxes J_i and thermodynamic forces X_i.

$$J_i = \sum_{k=1}^{N} L_{ik} X_k. \tag{1.1}$$

The coefficients L_{ik} are independent of thermodynamic forces and called the phenomenological coefficients. L_{ii} are proportionality factors of conjugate flux and force, whereas L_{ik} ($i = k$) are quantities concerning cross effects such as the Soret effect and the Dufour effect. Onsager demonstrated the following reciprocal relations [72, 73] in 1931.

$$L_{ik} = L_{ki}. \tag{1.2}$$

The phenomenological equations on the reduced heat flux $\mathbf{J}'_q$, which is the heat flux without the contribution of the mass transport, and the mass flux $\mathbf{J}_i$ (for component i) in the mixtures composed of N components of the temperature T without convection, chemical reactions, pressure gradient, and eternal forces can be written in a barycentric reference system as:

$$\mathbf{J}'_q = -L_{qq} \frac{\nabla T}{T^2} - \sum_{k=1}^{N-1} L_{qk} \frac{\nabla(\mu_k - \mu_N)_{p,T}}{T}, \tag{1.3}$$

$$\mathbf{J}_i = -L_{iq}\frac{\nabla T}{T^2} - \sum_{k=1}^{N-1} L_{ik}\frac{\nabla(\mu_k - \mu_N)_{p,T}}{T}, \quad (i,k=1,2,\cdots,N-1). \tag{1.4}$$

The phenomenological coefficients L_{qq} and L_{ik} represent the heat conduction and the mass diffusion. Also, L_{iq} and L_{qk} are related to the Soret effect and the Dufour effect. Because the chemical potential μ_k is function of the concentration, μ_k can be described with the mass fraction c_i:

$$(\nabla\mu_k)_{p,T} = \sum_{i=1}^{N-1}\left(\frac{\partial\mu_k}{\partial c_i}\right)_{p,T.c_j}\nabla c_i, \quad (k=1,2,\cdots,N-1). \tag{1.5}$$

1.2.2 Binary systems

For the binary systems ($N=2$), the reduced heat flux $\mathbf{J}'_q$ and mass flux $\mathbf{J}_i$ can be calculated from the Eqs. (1.3)–(1.5).

$$\mathbf{J}'_q = -L_{qq}\frac{1}{T^2}\nabla T - L_{q1}\frac{(\partial\mu_1/\partial c_1)_{p,T}}{c_2 T}\nabla c_1. \tag{1.6}$$

$$\mathbf{J}_1 = -L_{1q}\frac{1}{T^2}\nabla T - L_{11}\frac{(\partial\mu_1/\partial c_1)_{p,T}}{c_2 T}\nabla c_1. \tag{1.7}$$

After defining the mass diffusion coefficient D and thermodiffusion coefficient D_T as,

$$D = \frac{L_{11}}{\rho c_2 T}\left(\frac{\partial\mu_1}{\partial c_1}\right)_{p,T}, \tag{1.8}$$

$$D_T = \frac{L_{1q}}{c_1 c_2 \rho T^2}, \tag{1.9}$$

Eq. (1.6) can be written in a known form which is convenient to describe the actual experiments [53].

$$\mathbf{J}_1 = -\rho D\nabla c_1 - \rho c_1(1-c_1)D_T\nabla T, \tag{1.10}$$

where $\mathbf{J}_1$ is the mass flux of the component 1 ($\mathbf{J}_1 + \mathbf{J}_2 = 0$), c_1 is the mass fraction of the component 1 ($c_1 + c_2 = 1$), and ρ is the density.

In the stationary state where the mass flux by the mass diffusion and the Soret effect balance ($\mathbf{J}_1 = \mathbf{J}_2 = 0$), the ratio of the concentration gradient and the temperature gradient can be described as [32]:

$$\frac{\nabla c_1}{\nabla T} = -\frac{D_T}{D}c_1(1-c_1). \tag{1.11}$$

The Soret coefficient S_T is defined as the ratio of D_T to D.

$$S_T \equiv \frac{D_T}{D}. \tag{1.12}$$

With the Soret coefficient S_T, Eq. (1.11) can be written as Eq. (1.13).

$$\frac{\nabla c_1}{\nabla T} = -S_T c_1 (1 - c_1). \tag{1.13}$$

The magnitude of the separation by the Soret effect is characterized by the Soret coefficient S_T. When the sign of the S_T is positive, the component 1 is transported to the cold side.

1.2.3 Ternary systems

In ternary systems, there are two independent components. The mass fluxes of the component 1 and 2 are described as [62]:

$$\mathbf{J}_1 = -\rho D_{11} \nabla c_1 - \rho D_{12} \nabla c_2 - \rho D'_{T,1} \nabla T, \tag{1.14}$$

$$\mathbf{J}_2 = -\rho D_{21} \nabla c_1 - \rho D_{22} \nabla c_2 - \rho D'_{T,2} \nabla T. \tag{1.15}$$

D_{11} and D_{22} are the main diffusion coefficient. D_{12} and D_{21} are called as the cross diffusion coefficient, which characterize the mass diffusion influenced by the concentration of other components (cross-diffusion). $D'_{T,i}$ is the thermodiffusion coefficient of the component i. Mass flux and mass fraction of the dependent component 3 are described as,

$$c_3 = 1 - c_1 - c_2, \tag{1.16}$$

$$\mathbf{J}_3 = -\mathbf{J}_1 - \mathbf{J}_2. \tag{1.17}$$

The Soret coefficients of the component i are defined as the ratio of the concentration gradient to the temperature gradient in the stationary state, as in the binary case (cf. Eq. (1.13)):

$$\frac{\nabla c_i}{\nabla T} = -S'_{T,i} \tag{1.18}$$

From Eqs. (1.14) and (1.15) with $\mathbf{J}_1 = \mathbf{J}_2 = \mathbf{0}$, the Soret coefficients can be obtained as:

$$S'_{T,1} = \frac{D'_{T,1} D_{22} - D'_{T,1} D_{12}}{D_{11} D_{22} - D_{12} D_{21}}, \tag{1.19}$$

$$S'_{T,2} = \frac{D'_{T,2} D_{11} - D'_{T,1} D_{21}}{D_{11} D_{22} - D_{12} D_{21}}. \tag{1.20}$$

The Soret coefficient and thermodiffusion coefficient of the dependent component 3 are described as:

$$S'_{T,3} = -S'_{T,1} - S'_{T,2}, \quad D'_{T,3} = -D'_{T,1} - D'_{T,2}. \tag{1.21}$$

Note that thermodiffusion and Soret coefficients with a prime ($D'_{T,i}$ and $S'_{T,i}$) contain the

concentration factor $c_1 \times c_2$ in a widely accepted definition for ternary systems, while in the binary case the concentrations of the two components are usually factored out [58]. The binary thermodiffusion coefficient D_T and the Soret coefficient S_T can be converted to that with a prime $D'_{T,1}$ and $S'_{T,1}$, using the following equations [58].

$$D'_{T,1} = c_1(1-c_1)D_T . \tag{1.22}$$

$$S'_{T,1} = c_1(1-c_1)S_T . \tag{1.23}$$

In ternary systems, the positive Soret coefficient also indicates the transport to the cold side, as in binary systems. However, the sign of the Soret coefficient $S'_{T,i}$ does not always corresponds to that of thermodiffusion coefficient $D'_{T,i}$ in multicomponent systems of more than two components, because the sign of the cross diffusion coefficient can be positive or negative.

1.3   Experimental findings for binary systems

Although the microscopic mechanism of the Soret effect in liquid is still not well understood, a number of interesting findings based on experimental approaches were reported. In the following, part of them, mostly limited to binary systems, will be described.

1.3.0 Soret effect in gaseous mixture

Enskog and Chapman independently derived the thermodiffusion coefficient for gases by the Boltzmann equation [29–31]. In this classical theory for hard spheres, it was described that the heavier or larger component moves to the cooler region. The theoretical prediction was experimentally confirmed by Chapman and Dootson in 1917 [74]. Note that the attempts to extend the Chapman-Enskog theory to liquid state have not been successful [75].

1.3.1 Additive contributions due to difference in mass and moment of inertia

The effect of deuteration on the Soret coefficient was experimentally investigated by Debuschewitz and Köhler [47] for binary mixtures of benzene/cyclohexane and by Wittko and Köhler [48–50] for a large number of different organic liquids with cyclohexane. They found that the isotope substitution caused constant shift of the Soret coefficient depending neither on the composition nor on the mixing partner. It was shown that the Soret coefficient can be split into

three terms [47]:

$$S_T = a_M \frac{M_2 - M_1}{M_2 + M_1} + b_I \frac{I_2 - I_1}{I_2 + I_1} + S_T^0, \tag{1.24}$$

where a_M and b_I are constants, M_i is the molecular mass of species i, I_i is its moment of inertia, and S_T^0 is the so-called 'chemical' contribution to the Soret coefficient. Note that the isotopic part, the first and second terms of Eq. (1.24), was introduced by Schirdewahn *et al.* [76] for gaseous isotopic mixtures of hydrogen. It is assumed that the chemical contribution S_T^0, which includes all the compositional dependence of the Soret coefficient, is due to interparticle interactions in the system [2].

Hartmann *et al.* [51] measured the Soret coefficient of the binary mixtures composed of the homologous series of halobenzenes and halobenzenes in toluene and cyclohexane, and it was shown that the isotopic contribution can be applied not only to truly isotopic systems, but also to mixtures of chemically similar molecules.

1.3.2 Thermophobicity concept

Hartmann *et al.* [52] measured the Soret coefficients of 41 equimolar mixtures of ten different organic solvents and found an additive rule for the heats of transport, which are defined as the heat transported by the mass flows.

$$\mathbf{J}'_q = \sum_{k=1}^{n-1} Q'^*_k \mathbf{J}_k = \sum_{k=1}^{n} Q'^*_{k,\text{abs}} \mathbf{J}_k^{\text{abs}}. \tag{1.25}$$

$Q'^*_{k,\text{abs}}$ is the absolute reduced heat of transport and $Q'^*_k = Q'^*_{k,\text{abs}} - Q'^*_{n,\text{abs}}$ is the reduced heat of transport. $\mathbf{J}_k^{\text{abs}}$ is the absolute mass flux in the laboratory system,

$$\mathbf{J}_k^{\text{abs}} = \rho_k \mathbf{v}_k = \mathbf{J}_k + \rho_k \mathbf{v}, \tag{1.26}$$

where $\mathbf{v}_k$ is the absolute velocity of component k in the laboratory system and $\mathbf{v}_k$ is the barycentric velocity. For binary systems, the reduced heat of transport is expressed by the phenomenological coefficients as:

$$Q'^*_1 = Q'^*_{1,\text{abs}} - Q'^*_{2,\text{abs}} = \frac{L_{1q}}{L_{11}}. \tag{1.27}$$

From Eqs. (1.8), (1.9), (1.12), and (1.27), the reduced heat of transport is related to the Soret coefficient as:

$$S_T = \frac{Q'^*_1}{c_1 T (\partial \mu_1 / \partial c_1)_{p,T}}. \tag{1.28}$$

Using the molar absolute reduced heat of transport $Q_{k,\text{abs}}$, Eq. (1.28) can be expressed as [52]:

$$S_T = \frac{Q_{1,\text{abs}} - Q_{2,\text{abs}}}{RT^2 \left[1 + (\partial \ln \gamma_1 / \partial \ln x_1)_{p,T} \right]}.$$

(1.29)

γ_1 is the activity coefficient of component 1, x_1 is the mole fraction of component 1, and R is the gas constant.

Hartmann *et al*. [52] showed that a single value of the heat of transport $Q_{k,\text{abs}}$ can be assigned to every pure substance, which determines its tendency to be transported towards the cold side (thermophobicity). It was shown that ten organic solvents [52] (later extended to 23 solvents [53]) can be sorted according to their thermophobicity based on the heats of transport, similar to the standard electrode potential.

1.3.3 Change in signs of Soret coefficient

In liquid systems with specific interactions such as hydrogen bonds, changes in signs of the Soret coefficient at certain temperatures and/or compositions are frequently observed [2,3]. A typical example is the mixture of ethanol/water [39,43]. Iacopini *et al*. [77] reported sign reversals of the Soret coefficient as a function of temperature in protein solutions. Prigogine *et al*. [78] explained qualitatively the sign change of the Soret coefficient in alcoholic mixtures of methanol/benzene, ethanol/cyclohexane, cyclohexanol/cyclohexane, and ethanol/dioxane using a free energy concept. However, this phenomenological approach does not lead to a microscopic understanding of the Soret effect [3].

1.3.4 Molar mass independence of thermodiffusion coefficient of polymers

Schimpf and Giddings [45,46] investigated the influence of molar mass on the thermodiffusion coefficient of polystyrene, poly(α-methyl)styrene, polymethyl methacrylate, and polyisoprene in several solvents, and reported that the thermodiffusion coefficient did not depend on the molecular weight of polymers. Brochard and De Gennes [79] gave the explanation of the molar mass independence of the thermodiffusion coefficient by the idea based on the combination of non-equilibrium thermodynamics and hydrodynamic concepts.

1.4 Existing experimental techniques to measure Soret coefficient

There are several experimental techniques which have different excitation methods of the Soret effect, detection schemes, and diffusion lengths. In the following, existing experimental techniques to measure the Soret effect will be overviewed.

1.4.1 Thermogravitational column (TGC)

The thermogravitational column (TGC) technique is based on the principle of the Clusius-Dickel separation discovered in 1938 [12,80], which amplifies the separation of components by coupling thermodiffusion and natural convection. In TGCs, a sample mixture is put in a vertically long column which consists of two vertical plates or concentric cylinders [4]. Figure 1.1 shows a schematic of a parallelepipedic TGC. Copper plates separated by a small gap to create a horizontal temperature gradient are maintained at two different temperatures by circulating water. Usually, the temperature difference of about 5 K is kept for 24–48 hours [4], before extracting a small amount of sample (1–2 mL) from sampling taps to analyze the compositional distribution formed vertically by the Clusius-Dickel separation. The analysis of the composition of the extracted sample is carried out by the measurement of the refractive index or the density for the measurement of binary systems. In the measurement of ternary systems, both the refractive index and the density are analyzed to determine the composition [55]. Naumann *et al.* [40] developed a thermogravitational micro-column with an interferometric contactless detection system. Recently, Lapeira *et al.* [41] applied the optical digital interferometry technique to thermogravitational micro-column technique, which enabled to determine the complete concentration profile inside the micro-column.

From the Furry-Jones-Onsager theory [81], the vertical concentration gradient $\partial c_i / \partial y$ formed in a TGC is given by [66],

$$\frac{\partial c_i}{\partial y} = -\frac{504}{gL_x^{\,4}} \frac{D'_{T,i}\eta}{\beta},$$ (1.30)

where g is the gravity acceleration, η is the kinematic viscosity, β is the cubic thermal expansion coefficient. L_x is the gap of the column. In the ternary benchmark campaign, two types of TGCs with (i) $L_x = 1 + 0.005$ mm and the height of $L_y = 500$ mm, and (ii) $L_x = 1.02 + 0.005$ mm and $L_y = 980$ mm were employed [66].
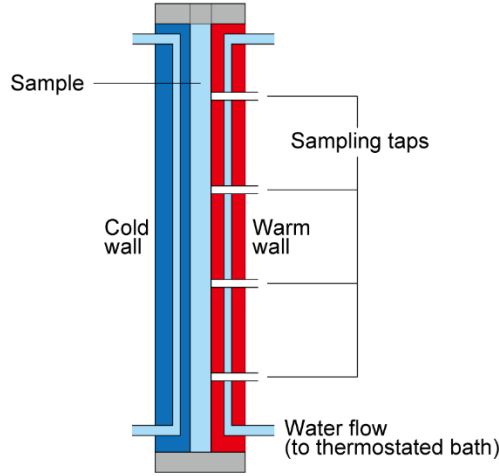
Figure 1.1: Schematic of a thermogravitational column (TGC).

It is pointed out that instabilities may make measurements difficult or even impossible for the system with the negative Soret coefficient of the denser component [2,82]. In addition, mechanical precision of TGCs can affect the reliability of measurements, because uncertainties may be generated by the length of the gap L_x, which is included in the form of L_x^4 in Eq. (1.30). Note that only thermodiffusion coefficients $D'_{T,i}$ can be obtained by Eq. (1.30) in TGC experiments. To determine the Soret coefficient, the mass diffusion coefficient obtained by other means is required.

1.4.2 Optical beam deflection (OBD)

The optical beam deflection (OBD) technique optically detects thermodiffusion in a Soret cell. As shown in Figure 1.2, a Soret cell consists of two horizontal parallel plates with different temperatures to form a vertical temperature gradient in a sample between the plates. In Soret cells, a vertical concentration distribution is formed by the Soret effect. Experimental studies employing Soret cells were started in 1920s by Tanner [83,84]. The analytical solution for binary mixtures in the Soret cell has been derived by Haugen and Firrozabadi [85].

$$\frac{c(y,t)-c_0}{-S'_T \Delta T / L} = y + \frac{1}{2}\sum_{m=-N}^{N}(-1)^m(y-m)\left\{\operatorname{erf}\left(\frac{2y-(2m+1)}{4\sqrt{t}}\right)-\operatorname{erf}\left(\frac{2y-(2m+1)}{4\sqrt{t}}\right)\right\}$$

$$+\sqrt{\frac{t}{\pi}}\sum_{m=-N}^{N}(-1)^m\left\{\exp\left(-\frac{2y-(2m+1)^2}{16t}\right)-\exp\left(-\frac{2y-(2m+1)^2}{16t}\right)\right\}, \quad (1.31)$$

where y is the vertical position, L is the vertical spacing, and ΔT is the temperature difference

between two plates.

In the OBD technique, the Soret effect in a Soret cell is detected by the deflection of a laser beam which enters the sample horizontally. Due to the vertical refractive index gradient induced by the Soret effect, the laser is deflected. The displacement of the deflected laser beam at the detector $\Delta y(t)$ is the function of the refractive index gradient $\partial n(t)/\partial y$.

$$\Delta y(t) = \frac{\partial n(t)}{\partial y} d \left(\frac{d}{2n} + \frac{d_{\text{w}}}{n_{\text{w}}} + \frac{d_{\text{air}}}{n_{\text{air}}} \right), \tag{1.32}$$

where n, n_{w}, n_{air} are the refractive index of the sample, exit window and air, respectively. Also, d, d_{w}, d_{air} are the length of the optical path in the sample, thickness of the exit window, and the distance between the exit window and the detector, respectively. For binary systems, the refractive index gradient $\partial n(t)/\partial y$ can be written as [39]:

$$\frac{\partial n(t)}{\partial y} = \left(\frac{\partial n}{\partial T} \right)_{p,c_1} \frac{\partial T(t)}{\partial y} + \left(\frac{\partial n}{\partial c_1} \right)_{p,T} \frac{\partial c_1(t)}{\partial y}, \tag{1.33}$$

$\partial T(t)/\partial y$ and $\partial c_1(t)/\partial y$ are calculated from the heat equation and the diffusion equation, respectively [39]. Thus, the Soret coefficient can be obtained by analyzing the time history of the displacement signal $\Delta y(t)$. Note that the optical contrast factors $\partial n/\partial T$ and $\partial n/\partial c_1$ are required to determine the Soret coefficient. The optical contrast factors can be measured by an Abbe refractometer or interferometric method [33,86].
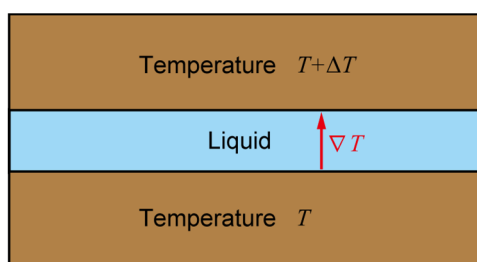
Figure 1.2: Schematic of a Soret cell.
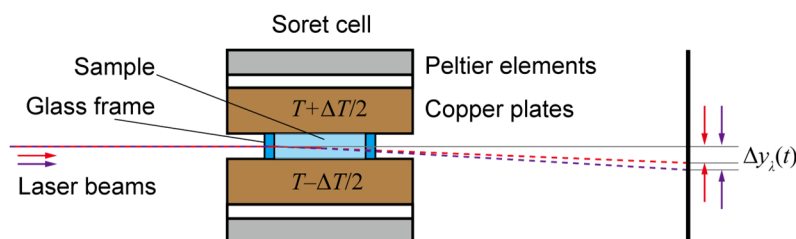
Figure 1.3: Schematic of the two-color optical beam deflection (OBD) apparatus.

As Haugen and Firrozabadi [60] suggested, measurement of ternary systems can be carried out by employing two readout lasers of different wavelengths λ, because the refractive index is dependent on the wavelength. For ternary systems, the refractive index gradient $\partial n(t)/\partial y$ can be written as [58]:

$$\frac{\partial n_\lambda(t)}{\partial y} = \left(\frac{\partial n_\lambda}{\partial T}\right)_{p,c_1,c_2} \frac{\partial T(t)}{\partial y} + \left(\frac{\partial n_\lambda}{\partial c_1}\right)_{p,c_2,T} \frac{\partial c_1(t)}{\partial y} + \left(\frac{\partial n_\lambda}{\partial c_2}\right)_{p,c_1,T} \frac{\partial c_2(t)}{\partial y}. \quad (1.34)$$

By using two lead out lasers, independent two displacement signals $\Delta y_\lambda(t)$ are obtained. This enables to determine the time dependent concentration profiles of all three components [58,60].

Figure 1.3 shows the schematic of the two-color OBD apparatus to measure ternary systems. In the OBD instruments for ternary systems developed by the group of Köhler [65], the readout lasers of $\lambda = 405$ nm and $\lambda = 635$ nm have been employed, whereas one readout laser of $\lambda = 637$ nm was used to measure binary mixtures of water/ethanol [39]. Temperature of the copper plates is controlled using Peltier elements. In the measurement of the ternary benchmark system [65], the time dependent OBD signals in 1–2 h were obtained under the temperature difference between two plates ΔT of 1.0 K, using the sample cell with the length of optical path $d = 10.0$ mm and with the vertical spacing of $h = 1.43$ mm.

1.4.3 Optical digital interferometry (ODI)

The optical digital interferometry technique also employs a Soret cell, but the cell height is larger (5–10 mm) to observe the mass transport by means of the Mach-Zehnder interferometer. The ODI technique was developed by Mialdun and Shevtsova for the ESA (European Space Agency) project of IVIDIL (influence of vibrations on diffusion in liquids) [87].

Figure 1.4 shows the schematic of the ODI apparatus. A beam splitter splits the expanded laser beam into two beams. One of them enters the Soret cell and the other is used as a reference beam. Two beams interfere at the second beam splitter. The interference fringes are observed by a CCD camera. In the measurement of binary benchmark systems [38], a He-Ne laser with the wavelength of $\lambda = 632.8$ nm was employed to detect the mass transport in a Soret cell with the cell height of $h = 6.3$ mm and optical path of $d = 18.0$ mm. For the binary benchmark systems, the characteristic time of the measurement τ_D is calculated by the cell height and the diffusion coefficient as $\tau_D = h/D \approx 12$ h [38], which means that ODI requires more than ten hours for the mixtures of small molecules with D in several 10^{-10} m^{2}s^{-1} due to the larger diffusion length.
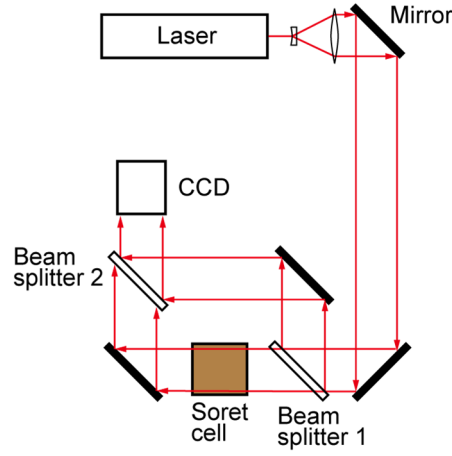
Figure 1.4: Schematic of the optical digital interferometry (ODI) apparatus.

By performing image processing based on 2-D Fourier transform technique to interference patterns recorded by a CCD, optical phase information can be extracted. The variation of the refractive index is obtained from the phase difference $\Delta\psi_\lambda$ [38],

$$\Delta n_\lambda(x,y,t) = n_\lambda(x,y,t) - n_\lambda(x,y,t_0) = \frac{\lambda}{2\pi d}\Delta\psi_\lambda(x,y,t). \qquad (1.35)$$

Here, x is the horizontal position perpendicular to the optical axis, y is the vertical position, and d is the length of the optical path. The variation of the refractive index is the function of the temperature and the mass fraction [38].

$$\Delta n_\lambda(x,y,t) = \left(\frac{\partial n_\lambda}{\partial T}\right)\Delta T(x,y,t) + \left(\frac{\partial n_\lambda}{\partial c_1}\right)\Delta c_1(x,y,t). \qquad (1.36)$$

Thus, the compositional profile over the entire two-dimensional cross section of the cell can be traced by the ODI technique.

Similar to the OBD technique, ternary systems can be measured by employing another probing laser. In the ground measurement of ternary benchmark system, two lasers with the wavelengths of $\lambda = 670$ nm and $\lambda = 925$ nm were used [61]. Measurement of ternary benchmark system by ODI was also performed under microgravity conditions in the selectable optical diagnostic instrument (SODI) instrument with the laser wavelengths of $\lambda = 670$ nm and $\lambda = 935$ nm [61].

1.4.4 Thermal field flow fractionation (ThFFF)

The field flow fractionation is an analytical technique for separating and characterizing macromolecules, supramolecular assemblies, colloids and particles [88], which was developed by Giddings in 1966 [89]. In this technique, an external field is applied perpendicularly to the direction of the flow of solutions or suspensions in a channel. A temperature gradient is used as a field in the thermal field flow fractionation (TFFF or ThFFF) technique.

Figure 1.5 shows the principle of ThFFF. A laminar parabolic flow profile is formed when the sample liquid flows through a thin channel under a temperature gradient [88]. Due to the Soret effect, sample particles of positive Soret coefficient are forced to the cold wall. As the result of the balance of the Soret effect and the mass diffusion, the concentration profile is built up in the direction of the temperature gradient. The special distribution of the particles in the steady-state is characterized by the effective layer thickness l, which approximately denotes the distance between the accumulation wall and the center of gravity of the particles. This parameter l and the velocity of the particles are related to the Soret coefficient. The retention ratio R, which is defined as the ratio of the average velocity of the analyte zone to the average velocity of the carrier liquid, is given by [45],

$$R = \frac{t_0}{t_r} = 6\frac{l}{w}\left\{\coth\left(\frac{1}{2(l/w)}\right) - 2\frac{l}{w}\right\}, \tag{1.37}$$

where w is the thickness of the channel. t_r is the retention time and t_0 is the passage time without external forces. The relationship between l and the Soret coefficient S_T is given by [45],

$$\frac{l}{w} = \frac{1}{(S_T + \beta)\Delta T}, \tag{1.38}$$

where β is thermal expansion coefficient, and ΔT is the temperature difference. By the measurement of the retention time t_r, the Soret coefficient is obtained with Eqs. (1.37) and (1.38). In the experiment by Schimpf and Giddings [45], a channel with the thickness of $w = 76$ μm, the breadth of 2.3 cm, and tip-to-tip length of 34 cm was employed. The temperature difference between the hot wall and the cold wall was $\Delta T = 30$ K [45].

Although ThFFF has been successfully used for polymers solutions, this technique is less suitable for mixtures of small molecules because too strong temperature gradients would be required [2]. In addition, to determine thermodiffusion coefficient, the mass diffusion coefficient should be obtained by other means.
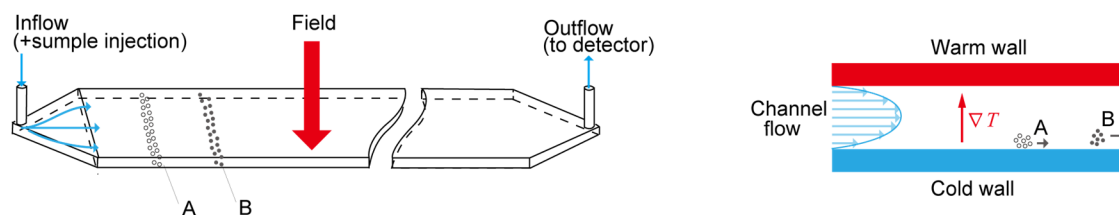
Figure 1.5: Principle of the thermal field flow fractionation (ThFFF) technique.
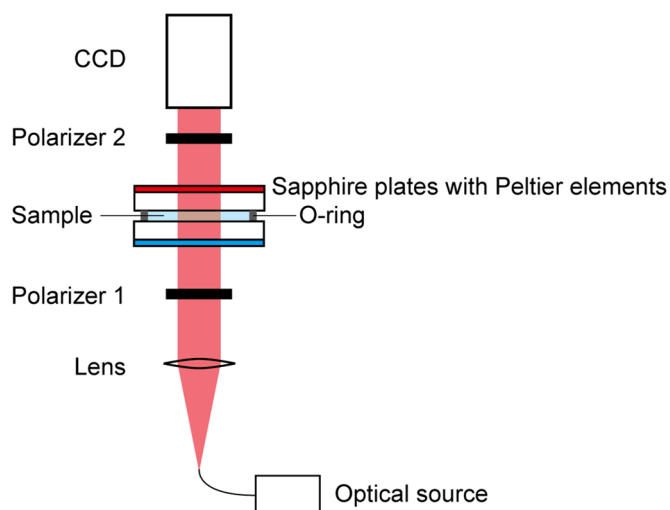
Figure 1.6: Instrument of the light scattering from non-equilibrium fluctuations (LS-NEF) technique.

1.4.5 Light scattering from non-equilibrium fluctuations (LS-NEF)

When a fluid is subjected to a stationary temperature gradient, long-range non-equilibrium fluctuations (NEFs) arise from a coupling between microscopic velocity fluctuations and the macroscopic temperature gradient [90]. Experimental analysis of the dynamics of non-equilibrium fluctuations by light scattering methods enables measurement of the Soret coefficient and the mass diffusion coefficient [42].

Figure 1.6 shows an optical setup for shadowgraph experiments. The non-equilibrium fluctuations in a thermodiffusion cell is observed by a low coherence light with the wavelength λ = 680 ± 10 nm and a charge coupled device (CCD) sensor [42]. The liner polarizer is employed to set the beam polarization before the light entering the Soret cell. The second linear polarizer

after the cell enables to control the average transmitted light intensity. The Soret cell consists of two sapphire plates maintained at different temperatures by Peltier elements. In the measurement of binary benchmark systems [42], the cell thickness (length of optical path for sample liquid) was $d = 1.3$ mm or $d = 1.53$ mm [42] and the temperature difference was 8–20 K.

In this technique, shadowgraph images are acquired after reaching the steady state. Quantity obtained from the analysis of the images is the so-called structure function which is given by [42]:

$$\left\langle \left| \Delta I_m(\mathbf{q}, \Delta t) \right|^2 \right\rangle = 2 A \left\{ T(\mathbf{q}) I_s(\mathbf{q}) \left[1 - ISF(\mathbf{q}, \Delta t) \right] + B(\mathbf{q}) \right\}, \tag{1.39}$$

$\Delta I_m(\mathbf{q}, \Delta t)$ is the spatial Fourier transformation of $\Delta i_m(\mathbf{r}, \Delta t)$, which is the difference of the measured intensity $\Delta i_m(\mathbf{r}, \Delta t) = i_m(\mathbf{r}, t) - i_m(\mathbf{r}, t + \Delta t)$ between a delay time Δt ($\mathbf{r}$ is the position). $\mathbf{q}$ is the wave number related to the scattering angle, A is a renormalization constant, $I_s(\mathbf{q})$ is the ensemble averaged scattered light, $T(\mathbf{q})$ is the transfer function of the imaging optics, and $B(\mathbf{q})$ is the noise of the measurement. For binary systems, the intermediate scattering function (ISF) is modeled as a single exponential decay due to the concentration NEF [42],

$$ISF(q, t) = \exp\left(-\frac{\Delta t}{\tau(q)} \right), \tag{1.40}$$

$\tau(q)$ is the relaxation time constant for the concentration component in the presence of gravity [42],

$$\tau(q) = \frac{1}{D q^2 \left\{ 1 + (q_c / q)^4 \right\}}, \tag{1.41}$$

q_c is the gravitational critical wave number which is related to the Soret coefficient as [42]:

$$S'_T = \frac{q_c^4 \eta D d}{\left\{ 1 / \rho (\partial \rho / \partial c) \right\} \Delta T}, \tag{1.42}$$

where η is kinematic viscosity, D is the mass diffusion coefficient, and d is the cell thickness. $1 / \rho \, (\partial \rho / \partial c)$ denotes the solutal expansion coefficient. By fitting analysis of the experimental structural function with Eqs. (1.39)–(1.42), the Soret coefficient and the mass diffusion coefficient can be obtained.

Non-equilibrium fluctuations in the ternary benchmark mixture were observed on a ground condition [91] and the good agreement between theory developed by Ortiz de Zárate [92] and the experiments for the larger wave numbers was obtained, which validated theory for the microgravity conditions. It was not possible to distinguish the two eigenvalues of the mass

diffusion matrix in the ternary benchmark mixture [91], but the two eigenvalues of the ternary polymer mixture composed of polystyrene, toluene, and *n*-hexane were well separated with the accuracy in the order of 1% [93].

1.4.6 Thermal lensing (TL)

In thermal lensing (TL) technique, both the excitation and detection of the Soret effect are carried out optically. Figure 1.7 shows the principle of thermal lens technique. The absorption of the laser generates the refractive index distribution in the sample. Due to the Gaussian profile of the laser beam, the refractive index distribution works as a laser induced lens (thermal lens). Following the formation of the temperature distribution in the sample, the Soret effect creates the concentration distribution, which also acts as a Soret lens. In the experiment by Polyakov and Wiegand [94], an infrared laser with the wavelength of $\lambda = 980$ nm was employed to investigate the Soret effect in the sample cell thickness of $d = 0.2$ mm and 1.0 mm. The distance between the sample cell and the beam waist was 3–4 mm [94]. When the sample cell placed 4 mm before the beam waist, the beam size ω was about 54 μm [94]. The temperature difference formed by the laser absorption was in the order of 0.05 K [94].

The mass transport can be evaluated by the intensity change after the sample on the optical axis. The intensity in a thermal lens experiment $I(t)$ is given by [95]:

$$\frac{I(t)}{I(0)} = \left[1 + \frac{\theta_{\text{th}}}{1 + \tau_{\text{th}}/t} + \frac{\theta_{\text{Soret}}}{1 + \tau_{\text{Soret}}/t} + 0.5 \left(\frac{\theta_{\text{th}}}{1 + \tau_{\text{th}}/t} + \frac{\theta_{\text{Soret}}}{1 + \tau_{\text{Soret}}/t} \right)^2 \right]^{-1}, \qquad (1.43)$$

$\tau_{\text{th}} = \omega^2/(4a)$ and $\tau_{\text{Soret}} = \omega^2/(4D)$ are characteristic time constants of the formation of thermal lens and the Soret lens, respectively, in which ω is the beam spot size, a is thermal diffusivity, and the D is the mass diffusion coefficient. θ_{th} and θ_{Soret} are strengths of thermal and Soret lens, which are related to the focal length of each lens [95],
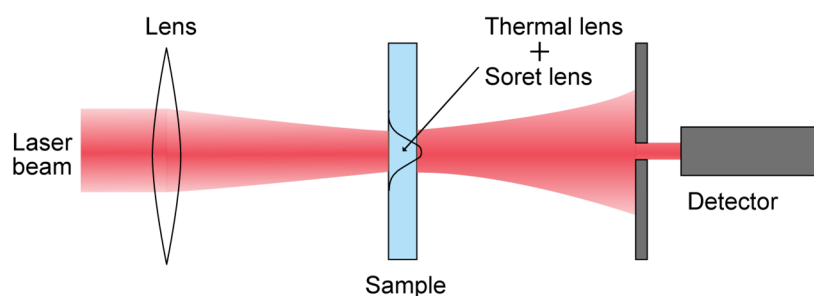
Figure 1.7: Principle of thermal lens technique.

$$\theta_{th} = -0.52 \frac{\alpha P d}{(\rho a C_p)\lambda} \frac{\partial n}{\partial T}, \tag{1.44}$$

$$\theta_{Soret} = -0.52 \frac{\alpha P d}{(\rho a C_p)\lambda} \frac{\partial n}{\partial c} S'_T, \tag{1.45}$$

where α is the absorption coefficient, P is the laser power, d is the cell thickness, ρ is the density, C_p is the specific heat at constant pressure, and λ is the wavelength of the laser. The numerical factor of 0.52 is introduced when the parabolic lens model gets extended [95,96]. Optical contrast factors are required to determine the Soret coefficient.

Careful consideration of convection is required in thermal lens experiments. In the measurement by Voit [97] on the binary benchmark mixutre n-dodecane/1,2,3,4 tetrahydronaphthalene, the Soret coefficient was 40% smaller than the benchmark value, which can be explained by the convection [94]. Measurement of systems with very small mass diffusion coefficient can be difficult, because convection might disturbs the concentration distribution by the Soret effect before reaching the stationary state [95,98]. In addition, it is pointed out that the optical distortion of the probing beam can be a problem [95].

1.4.7 Holographic grating technique (HGT)

The transient holographic grating technique is one of all optical techniques, similar to thermal lens technique, in which both excitation and detection are performed optically. The laser induced dynamic grating [99] is applied to the measurement of the Soret coefficient in this technique.

Figure 1.8 illustrates the principle of the holographic grating technique. The sinusoidal temperature distribution is formed by the absorption of the heating laser beams interfering in the sample. The Soret effect is subsequently induced by generated temperature grating with the interference fringe. In this process, the sample works as a form of diffraction grating because the spatially sinusoidal distribution of a refractive index is generated by the heat and mass transport. The mass transport can be evaluated by the intensity of the diffracted beam of a different laser, because the diffraction efficiency includes information on the compositional change.

The first observation of the Soret effect by this technique was reported by Thyagarajan and Lallemand on CS_2/ethanol mixtures in 1978 [100]. Köhler *et al.* [101–103] significantly improved the transient holographic grating technique using heterodyne detection schemes, and their improved method is known as the thermal diffusion forced Rayleigh scattering (TDFRS). To convert the interference pattern to the temperature grating, addition of small amount of inert
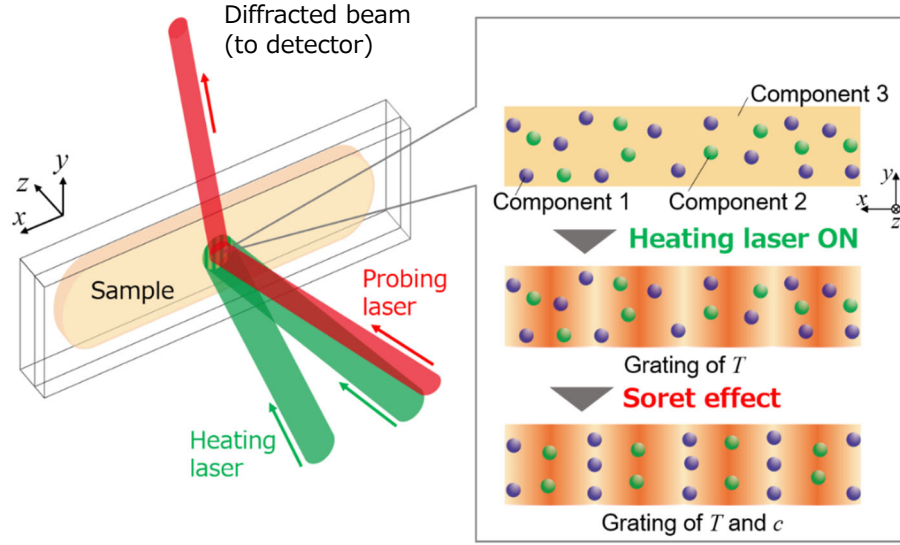
Figure 1.8: Principle of holographic grating technique.

dye to the sample is required in measurement by TDFRS setup employing a heating laser of visible wavelength [103]. Wiegand *et al.* [104] has been developed the infrared thermal diffusion forced Rayleigh scattering (IR-TDFRS) setup, employing an infrared laser with the wavelength of $\lambda = 980$ nm. This enables measurement of transparent samples without doping a dye.

The normalized heterodyne diffraction intensity to be detected in TDFRS experiments is given by [103]:

$$\zeta_{het}(t) = 1 - \exp\left(-\frac{t}{\tau_a}\right) - \frac{1}{\tau_D - \tau_a}\left(\frac{\partial n}{\partial c}\right)_{p,T}\left(\frac{\partial n}{\partial c}\right)_{p,c}^{-1} S_T c_0 (1 - c_0)$$

$$\times \left[\tau_D\left\{1 - \exp\left(-\frac{t}{\tau_D}\right)\right\} - \tau_a\left\{1 - \exp\left(-\frac{t}{\tau_a}\right)\right\}\right], \qquad (1.46)$$

$\tau_{th} = 1/(aq^2)^{-1}$ and $\tau_D = 1/(Dq^2)$ are characteristic time constant of heat and mass diffusion, respectivel. q is the wavenumber of grating $q = 2\pi/\Lambda$ and Λ is the fringe spacing. The optical contrast factors are required to determine the Soret coefficient.

TDFRS is very sensitive technique which is able to detect the relative change of concentration below 10^{-5} induced by the temperature grating with the amplitude of 10 to 100 mK [103]. The characteristic time of the measurement is very short due to the fringe spacing in μm order. However, signal averaging in several thousands of times is required to increase the signal to noise ratio [2,102].

1.5 Motivation and objectives

Table 1.1 compares the experimental techniques employed to measure the Soret coefficient. Each technique has its advantages, but there is no established method feasible to all kinds of samples. So far, only three techniques of TGC [55,70], OBD [58,59,71], and ODI [61] have been successfully employed to determine the Soret coefficient in ternary systems. Although two eigenvalues of the mass diffusion matrix in the ternary polymer solution of polystyrene + toluene + hexane were obtained by the analysis of NEFs, but Soret coefficients were not provided from the single wavelength experiments [93]. It is suggested that a two-wavelength shadowgraph experiment is required for the determination of the Soret coefficients in ternary systems [93]. The two-wavelength technique for ternary systems can be also applied to thermal lens technique [95], but no such experiments have been reported.

Table 1.1: Comparison of experimental techniques to investigate the Soret effect.

Method	Measured quantity (for binary systems)	Diffusion length	Temperature difference	Temperature gradient	Characteristic time of measurement	Sample cell volume
TGC	D_T	(convection coupling)[a]	10 K [70]	10^4 K/m	24–48 h [4]	30 mL [41]
OBD	S_T, D_T, D	1.43 mm [65]	1 K [65]	$\sim 7 \times 10^2$ K/m	~ 1 h [65]	~ 0.3 mL [105]
ODI	S_T, D_T, D	6.06 mm [38]	5.994 K [38]	$\sim 10^3$ K/m	~ 16 h [38]	~ 0.6 mL [38]
ThFFF	S_T	76 μm[b] [45]	30 K [45]	$\sim 4 \times 10^5$ K/m	10^1–10^2 min [88]	0.65 mL[c] [45]
LS-NEF	S_T, D_T, D	2 mm [91]	16 K [91]	$\sim 8 \times 10^3$ K/m	0.035–35 s[d] [91]	~ 1 mL [91]
TL	S_T, D_T, D	27 μm [94]	~ 0.05 K [94]	$\sim 2 \times 10^3$ K/m	$\sim 10^2$ s [95]	~ 0.3 mL [95]
HGT (TDFRS)	S_T, D_T, D	~ 10 μm [2]	10–100 mK [103]	10^0 –10^1 K/m	0.03 s [95]	0.06 mL [95]

[a] The diffusion length in TGC experiments may not be defined, although the gap between two walls with different temperature was, for example, 1 mm [66]. [b] The thickness of the flow channel. [c] Sample injection volume was 3 μL [45]. [d] Correlation time.

The transient holographic grating technique has not been established for ternary systems, although this method has been successfully used in the measurement of binary systems, including polymer solutions [101,102,106,107], polymer blends [108–110], isotopic systems [47–51], and aqueous solutions [28,104,111–120]. One feature of the transient holographic grating technique is the very short characteristic time of the measurement, on the order of milliseconds for mixtures of small molecules, which is several orders faster than other measurement techniques. In addition, it is possible to investigate samples with high viscosity, such as concentrated polymer solutions [106,107], which may be difficult to measure with convective coupling techniques such as TGC. Moreover, the small amplitude of the temperature modulation (sub-milliKelvin) of the grating to induce thermodiffusion allows for measurement of samples close to the critical point, where precise temperature control is important [110]. Therefore, measurements of ternary systems by the holographic grating technique can contribute to gain broader knowledge of mass transport in multicomponent systems.

The concept of the two-color TDFRS to measure ternary systems was proposed by Köhler *et al.* [58,121]. The result of a single measurement by the two-color TDFRS is available in Königer's PhD thesis [121], although it does not include a schematic or detailed description of the experimental apparatus. In the two-color TDFRS experiment using the readout lasers with wavelengths of 405 nm and 633 nm [121], the Soret coefficients of the ternary mixture composed of THN, IBB, and nC12 were obtained in the same sign and magnitude with the measured values by the two-color OBD technique. Königer, however, reported that reliability was limited because of some experimental problems [121]. For example, the experiments by the two readout lasers were not carried out simultaneously [121].

In this study, with the aim to measure the Soret coefficient in ternary systems by the optical holographic grating, an experimental apparatus has been developed based on the instrument independently built by the group of Nagasaka [122–125] in parallel with the use of the forced Rayleigh scattering (FRS) technique to measure thermal diffusivity of liquids [126]. The direct (homodyne) detection scheme instead of the heterodyne scheme is adopted, which enabled to measure the mass diffusion coefficient by the signal averaging of only 16 times with a simpler configuration of the instrument [125]. This technique has been called as the Soret forced Rayleigh scattering (SFRS) by the Nagasaka group, although the principle is basically identical to that of the TDFRS technique.

The remaining part of this thesis is organized as follows: Chapter 2 describes the working equations to measure the Soret coefficient in ternary systems by the Soret forced Rayleigh scattering employing the homodyne detection scheme. In addition, the instrument designed and built for the simultaneous detection by the two detection lasers with the wavelengths of 403 nm and 639 nm is presented. It is important to design the optical path to detect each signal of the two probing lasers independently at the same time, because in the two-color detection scheme [60], two parameters obtained independently by each signal of the probing laser are used together to determine the two independent Soret coefficients. By using the homodyne detection scheme of the SFRS technique, design of the optical system for simultaneous detection of two-wavelength signals can be less complicated, because the reference beam for heterodyne detection is not required.

Chapter 3 describes experiments to evaluate the validity of the newly developed instrument, which were carried out on the binary and ternary benchmark systems composed of 1,2,3,4-tetrahydronaphthalene, isobutylbenzene, and *n*-dodecane.

Chapter 4 reports the application of this technique to the measurement of three Soret coefficients of ternary mixtures dissolving a polymer, which has not been successfully achieved by any techniques so far. Understanding the thermophysical properties of polymer solutions is of great significance in engineering, because polymer materials are generally dissolved in solvents in fabrication process of polymer films, fibers and other products [127]. In solution casting to make polymer films, sometimes two or more solvents are used to control the drying rate, which affects the quality of the products. Because mass transport phenomena can play dominant roles in the drying process [23], knowledge of the mass transport properties is important to optimize the fabrication process. The ternary polymer solutions of practical interest in engineering were selected as samples in this study, which were composed of cellulose acetate butyrate (CAB), styrene monomer, and 2-butanone. CAB is widely used material for functional polymer films [125, 128,129], and styrene monomer and 2-butanone are good solvents of CAB.

Chapter 5 describes the development of another instrument employing a CO_2 laser to measure the Soret coefficient in aqueous systems. Understanding of the Soret effect in aqueous systems, where the mass transport can be complicated due to the presence of hydrogen bonding, is considered to promote applications in the field of biotechnology. In drug delivery systems, for instance, knowledge of the Soret effect can help the design of drug delivery vehicles which are

targeted to warmer sites of inflammation. Although SFRS instrument presented in Chapter 2 requires addition of dye for the absorption of the heating laser with visible wavelength, it is difficult to find a suitable dye for aqueous systems. Employing an infrared wavelength as the heating laser can solve this problem. The validity of this IR-SFRS technique employing the homodyne detection scheme is tested by the measurement of a binary solution of water/ethanol, as a first step to examine more complexed systems. The IR-SFRS can be potentially extended to measure the Soret coefficient in ternary systems, by applying the two-wavelength detection technique.

Lastly, chapter 6 presents the conclusion of this study.

2

Design and construction of instrument for ternary systems

2.1 Concept

The strategy to measure the Soret coefficient in ternary system in this study is based on the integration of the two-wavelength detection scheme [60] and the holographic grating technique of the Soret forced Rayleigh scattering (SFRS) developed by Nagasaka *et al.*, which adopts the homodyne detection scheme [125]. Figure 2.1 illustrates the concept of the SFRS with two-wavelength detection scheme for measurement of ternary systems.
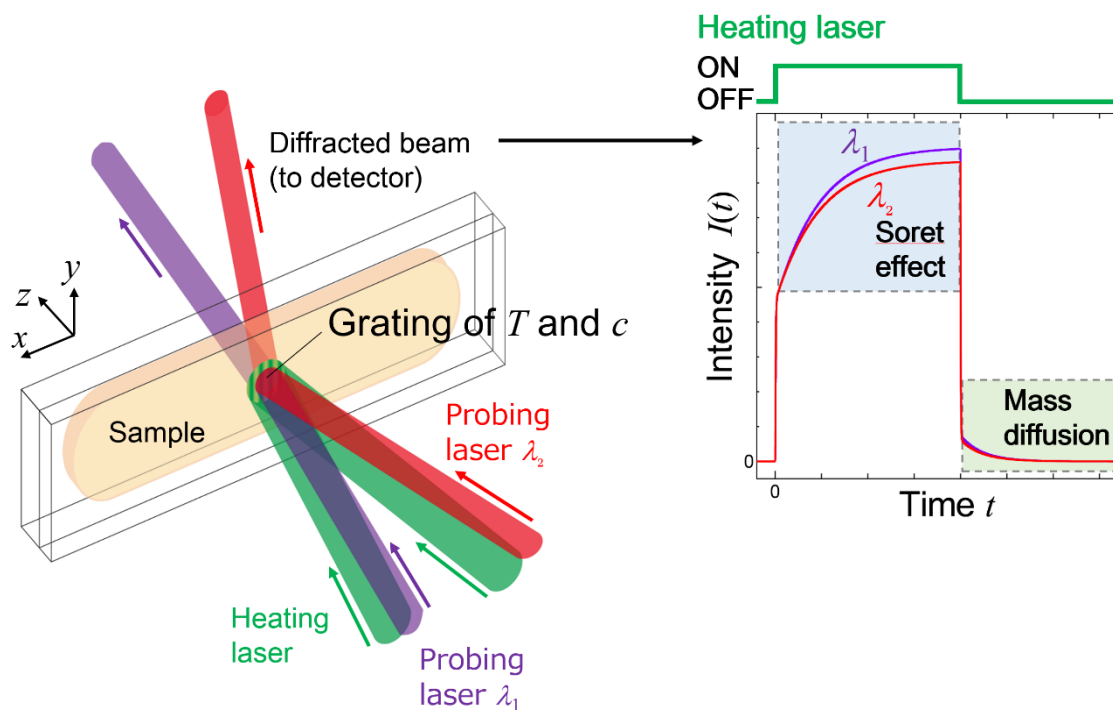
Figure 2.1: Concept of Soret forced Rayleigh scattering (SFRS) technique with two-wavelength detection scheme for measurement of ternary systems.

In the holographic grating technique, the probing laser detects the contrast of the refractive index grating modulated by the temperature and concentration gratings which are formed by the heating laser [103,125]. Typical examples of the signal intensity in SFRS experiments, which is proportional to the diffracted light intensity at the detector, are also shown in Figure 2.1. The sharp intensity change after the start of the heating ($t = 0$) indicates the formation of the temperature distribution corresponding to the interference fringe. The relatively slow change after the formation of the temperature distribution indicates the formation of the concentration distribution by the Soret effect. The sharp descent after the end of the heating indicates the decay of the temperature distribution. The gradual descent after the decay of the temperature distribution indicates the decay of the concentration distribution due to the mass diffusion. Because of the dependence of the refractive index on wavelength, two independent signals can be obtained by employing two probing laser of different wavelengths, which enables the measurement of the Soret coefficients in ternary systems.

In this chapter, the working equations for homodyne detection schemes and the SFRS instrument with two probing lasers of different wavelengths developed for ternary systems will be presented. A detailed description of the working equations is important for the evaluation of the uncertainty based on the GUM (guide to the expression of uncertainty in measurement) [130].

2.2   Working equations for binary systems

Because the SFRS instrument of the Nagasaka group adopting homodyne detection scheme was not validated for the measurement of the Soret coefficient, the working equations to measure the Soret coefficient in binary systems should be presented before moving on to ternary systems. For the measurement of the Soret coefficient, the formation signals due to the Soret effect as well as the relaxation signals due to the mass diffusion should be analyzed, while only relaxation signals were evaluated in the previous SFRS technique to obtain the mass diffusion coefficient in binary systems [125], which inherited the FRS technique to measure the thermal diffusivity from the relaxation signals due to the heat diffusion [126]. The idea to improve the SFRS technique to investigate the Soret effect is to analyze the formation signal to determine the Soret coefficient, with the value of the mass diffusion coefficient obtained in advance from the analysis of the

relaxation signal.

In the SFRS technique, the intensity of the diffracted beam of the probing laser for the Bragg condition is in proportion to the squares of the amplitude of the refractive index grating $\Delta n(t)$ [125,131]. For small temperature and concentration modulation in binary systems, $\Delta n(t)$ is given by [103, 125]:

$$\Delta n(t) = \left(\frac{\partial n}{\partial T}\right)_{p,c} \Delta T(t) + \left(\frac{\partial n}{\partial c}\right)_{p,T} \Delta c(t), \qquad (2.1)$$

where $\Delta T(t)$ and $\Delta c(t)$ are the amplitude of the sinusoidal temperature distribution and concentration distribution, respectively. $\partial n/\partial T$ and $\partial n/\partial c$ are so-called optical contrast factors related to the dependence of the refractive index n on the temperature T and the mass fraction c at constant pressure p, respectively.

2.2.1 Formation process by Soret effect

The amplitude of the temperature distribution $\Delta T(t)$ after the start of the heating at $t = 0$ can be calculated by the one-dimensional heat conduction equation in an x-coordinate, under the assumption that the fringe spacing is small compared with the sample thickness, the absorption length of the sample, and the diameter of the heated area [126]:

$$\frac{\partial T(x,t)}{\partial t} = a\frac{\partial^2 T(x,t)}{\partial x^2} + \frac{\alpha}{\rho C_p} I_h(x), \qquad (2.2)$$

where $T(x,t)$ is the temperature, t is the time, a is the thermal diffusivity, α is the absorption coefficient at the wavelength of the heating laser, ρ is the density, and C_p is the specific heat at constant pressure. $I_h(x)$ is the intensity of the heating beams by the two interfering heating laser beams of equal intensity $I_{h,0}/2$,

$$I_h(x) = I_{h,0}(1 + \cos qx), \qquad (2.3)$$

where $q = 2\pi/\Lambda$ is the wavenumber of the interference pattern with the fringe spacing Λ. The solution of Eq. (2.2) is obtained as [125]:

$$T(x,t) = T_m(t) + \Delta T(t)\cos qx + T_0, \qquad (2.4)$$

T_0 is the initial uniform temperature, and $T_m(t)$ is the mean temperature rise of the sample in the course of laser heating,

$$T_{\mathrm{m}}(t) = \frac{\alpha I_{\mathrm{h},0}}{\rho C_p} t, \tag{2.5}$$

The amplitude of the temperature $\Delta T(t)$ in Eq. (2.4) is described as:

$$\Delta T(t) = \frac{\alpha I_{\mathrm{h},0}}{\rho C_p} \tau_a \left\{ 1 - \exp\left(-\frac{t}{\tau_a}\right) \right\}, \tag{2.6}$$

where τ_a is the decay time constant of heat conduction,

$$\tau_a = \frac{1}{aq^2} = \frac{1}{a}\left(\frac{\Lambda}{2\pi}\right)^2. \tag{2.7}$$

The amplitude of the concentration distribution $\Delta c(t)$ can be obtained by the following one-dimensional diffusion equation in an x-coordinate [125]:

$$\frac{\partial c(x,t)}{\partial t} = D\frac{\partial^2 c(x,t)}{\partial x^2} + D_T c(x,t)\{1 - c(x,t)\}\frac{\partial^2 T(x,t)}{\partial x^2}, \tag{2.8}$$

in which $c(x,t)$ is the mass fraction of the solute. D is the diffusion coefficient and D_T is the thermodiffusion coefficient. For small concentration change in SFRS experiments, $c(x,t)\{1 - c(x,t)\} \approx c_0(1 - c_0)$, with c_0 being the initial mass fraction. By solving Eq. (2.8), the solution is given by [125]:

$$c(x,t) = \frac{\alpha I_{\mathrm{h},0}}{\rho C_p}\frac{D_T}{a - D}c_0(1 - c_0)$$

$$\times \left[\tau_a\left\{1 - \exp\left(-\frac{t}{\tau_a}\right)\right\} - \tau_D\left\{1 - \exp\left(-\frac{t}{\tau_D}\right)\right\} \right]\cos\left(\frac{2\pi x}{\Lambda}\right) + c_0, \tag{2.9}$$

where τ_D is the decay time constant of mass diffusion,

$$\tau_D = \frac{1}{Dq^2} = \frac{1}{D}\left(\frac{\Lambda}{2\pi}\right)^2. \tag{2.10}$$

Under reasonable assumptions for liquid mixtures $D \ll a$ ($\tau_D \gg \tau_a$), Eq. (2.9) for a sufficient amount of time after the formation of the temperature distribution ($t \gg \tau_a$) can be sufficiently approximated by [125],

$$c(x,t) = -\frac{\alpha I_{\mathrm{h},0}}{\rho C_p}S_T c_0(1 - c_0)\tau_a\left\{1 - \exp\left(-\frac{t}{\tau_D}\right)\right\}\cos qx + c_0. \tag{2.11}$$

Comparing Eq. (2.11) to Eq. (2.12), the amplitude of the concentration distribution $\Delta c(t)$ is given by Eq. (2.13) [125],

$$c(x,t) = \Delta c(t)\cos(qx) + c_0, \tag{2.12}$$

28

$$\Delta c(x,t) = -\frac{\alpha I_{h,0}}{\rho C_p} S_T c_0 (1-c_0) \tau_a \left\{ 1 - \exp\left(-\frac{t}{\tau_D}\right) \right\}. \tag{2.13}$$

From Eqs. (2.1), (2.6) and (2.13), the intensity of the diffracted light $I(t) \propto [\Delta n(t)]^2$ in the formation process of the concentration distribution by the Soret effect ($t \gg \tau_a$) is expressed as follows:

$$I(t) \propto \left[\frac{\partial n}{\partial T} - S_T c_0 (1-c_0) \left\{ 1 - \exp\left(-\frac{t}{\tau_D}\right) \right\} \frac{\partial n}{\partial c} \right]^2, \tag{2.14}$$

where $S_T = D_T/D$ is the Soret coefficient.

2.2.2 Relaxation process by mass diffusion

For simplicity, time $t = 0$ is set at the end of heating, when describing the relaxation process after the heating laser is switched off. After the heating laser pulse duration time t_h, the relaxation of the thermal grating is expressed by [125]:

$$T(x,t) = T_m(t) + \Delta T(t_h) \exp\left(-\frac{t}{\tau_a}\right) \cos qx + T_0. \tag{2.15}$$

The relaxation of the concentration grating following the decay of the thermal grating ($t \gg \tau_a$) is expressed by [125]:

$$c(x,t) = \Delta c(t_h) \exp\left(-\frac{t}{\tau_D}\right) \cos qx + c_0. \tag{2.16}$$

Similarly to the formation process, the intensity of the diffracted light $I(t)$ in the relaxation process of the concentration distribution by the mass diffusion is expressed as follows [125]:

$$I(t) \propto \exp\left(-\frac{t}{\tau_D}\right)^2. \tag{2.17}$$

2.2.3 Fitting models for data evaluation

In the analysis of the detected signal obtained in the SFRS experiments, the effect of the coherent and incoherent scattered light superimposed over the diffracted light should be considered. The output voltage $V(t)$, which is proportional to the light intensity at the detector, is described as [99]:

$$V(t) \propto I(t) + 2\sqrt{I(t)I_c} \cos\psi + I_c + I_{inc}, \tag{2.18}$$

where I_c is the intensity of the coherent scattered light and I_{inc} is that of the incoherent scattered light. ψ is the phase difference between the diffracted light and the coherent scattered light.

From Eqs. (2.17) and (2.18), the fitting model of the output intensity for the relaxation process by the mass diffusion ($t \gg \tau_a$) is given by [125]:

$$V(t) - V(\infty) = A \exp\left(-\frac{2t}{\tau_D}\right) + D_{sc} \exp\left(-\frac{t}{\tau_D}\right), \tag{2.19}$$

with

$$D_{sc} = 2\sqrt{AV(\infty)} \cos\psi . \tag{2.20}$$

Here, A is the amplitude factor for the diffracted light and D_{sc} is that for the coherent scattered light. $V(\infty)$ is the output voltage, which is proportional to the total scattered light. The fitting parameters are A, D_{sc}, $V(\infty)$, and the decay time constant of mass diffusion τ_D. After evaluating τ_D by the fitting analysis, the mass diffusion coefficient can be determined by Eq. (2.10).

The output for the formation process by the Soret effect ($t \gg \tau_a$) can be derived from Eq. (2.14) and Eq. (2.18) as:

$$V(t) - V(\infty) = A'\left[\{1 - \zeta(t)\}^2 + \frac{1}{A/D_{sc}} \zeta(t_h)\{1 - \zeta(t)\}\right], \tag{2.21}$$

with

$$\zeta(t) = S_T c_0 (1 - c_0)\left(\frac{\partial n}{\partial c}\right) \cdot \left(\frac{\partial n}{\partial T}\right)^{-1} \left\{1 - \exp\left(-\frac{t}{\tau_D}\right)\right\}, \tag{2.22}$$

in which A' is the factor of proportionality. Using the values of τ_D, A, D_{sc}, and $V(\infty)$ determined from the analysis of the relaxation process by the mass diffusion, the number of the fitting parameters can be reduced to two: S_T and A'. The optical contrast factors $\partial n/\partial T$ and $\partial n/\partial c$ should be evaluated by a refractometer in advance.

After evaluating the Soret coefficient, the thermodiffusion coefficient D_T can be determined by the relationship $D_T = S_T \cdot D$ (Eq. (1.12)).

2.3 Derivation of Working equations for ternary solutions by direct detection scheme

In the following, the working equations on the formation and relaxation process for ternary systems will be derived, in a similar way to the binary systems. The data evaluation method to determine the Soret coefficient and the thermodiffusion coefficient in ternary systems, applying the two-wavelength detection technique, will be also presented.

The intensity of the diffracted beam $I_\lambda(t)$ of the probing laser with the wavelength λ is in proportion to the square of the amplitude of the sinusoidal refractive index distribution $\Delta n_\lambda(t)$. $\Delta n_\lambda(t)$ in the experiments on the ternary systems can be expressed as:

$$\Delta n_\lambda(t) = \left(\frac{\partial n_\lambda}{\partial c_1}\right)_{p,T,c_2} \Delta c_1(t) + \left(\frac{\partial n_\lambda}{\partial c_2}\right)_{p,T,c_1} \Delta c_2(t) + \left(\frac{\partial n_\lambda}{\partial T}\right)_{p,c_1,c_2} \Delta T(t),$$ (2.23)

where c_i is the mass fraction of the component i.

2.3.1 Formation process by Soret effect

The extended diffusion equations for ternary systems in the x-axis are described as:

$$\frac{\partial c_1(x,t)}{\partial t} = D_{11} \frac{\partial^2 c_1(x,t)}{\partial x^2} + D_{12} \frac{\partial^2 c_2(x,t)}{\partial x^2} + D'_{T,1} \frac{\partial^2 T(x,t)}{\partial x^2},$$ (2.24)

$$\frac{\partial c_2(x,t)}{\partial t} = D_{21} \frac{\partial^2 c_1(x,t)}{\partial x^2} + D_{22} \frac{\partial^2 c_2(x,t)}{\partial x^2} + D'_{T,2} \frac{\partial^2 T(x,t)}{\partial x^2},$$ (2.25)

in which t is the time, $c_i(x,t)$ is the mass fraction of the component i, D_{ij} is the diffusion coefficient, and $D'_{T,i}$ is the thermodiffusion coefficient. The concentration amplitudes $\Delta c_i(t)$ for a sufficient amount of time after the formation of the temperature distribution ($t \gg \tau_a$, $t = 0$ is set at the start of heating) are obtained by solving the diffusion equations of Eqs. (2.24), (2.25):

$$\Delta c_1(t) = \frac{\alpha I_{h,0}}{\rho C_p} \frac{1}{aq^2} \left\{ \begin{array}{l} -\dfrac{D'_{T,1} - S'_{T,1}\hat{D}_2}{\hat{D}_2 - \hat{D}_1} \exp(-\hat{D}_1 q^2 t) \\[2em] +\dfrac{D'_{T,1} - S'_{T,1}\hat{D}_1}{\hat{D}_2 - \hat{D}_1} \exp(-\hat{D}_2 q^2 t) - S'_{T,1} \end{array} \right\},$$ (2.26)

$$\Delta c_2(t) = \frac{\alpha I_{h,0}}{\rho C_p} \frac{1}{aq^2} \left\{ \begin{array}{l} -\dfrac{D'_{T,2} - S'_{T,2}\hat{D}_2}{\hat{D}_2 - \hat{D}_1} \exp(-\hat{D}_1 q^2 t) \\[2em] +\dfrac{D'_{T,2} - S'_{T,2}\hat{D}_1}{\hat{D}_2 - \hat{D}_1} \exp(-\hat{D}_2 q^2 t) - S'_{T,2} \end{array} \right\}, \tag{2.27}$$

in which $\hat{D}_1$ and $\hat{D}_2$ are the eigenvalues of the diffusion matrix [62].

$$\hat{D}_1 = \frac{1}{2}\left\{ (D_{11} + D_{22}) - \sqrt{(D_{11} - D_{22})^2 + 4D_{12}D_{21}} \right\}, \tag{2.28}$$

$$\hat{D}_2 = \frac{1}{2}\left\{ (D_{11} + D_{22}) + \sqrt{(D_{11} - D_{22})^2 + 4D_{12}D_{21}} \right\}. \tag{2.29}$$

Substituting the concentration amplitudes in Eqs. (2.26) and (2.27) and the temperature amplitude in Eq. (2.6) into Eq. (2.23), $\Delta n_\lambda(t)$ can be calculated. From the relation of $I_\lambda(t) \propto \{\Delta n_\lambda(t)\}^2$, the intensity of the diffracted beam $I_\lambda(t)$ during the formation process of the concentration distribution by the Soret effect can be derived as:

$$I_\lambda(t) \propto \left[\begin{array}{l} -\dfrac{1}{\hat{D}_2 - \hat{D}_1}\left(P'_{T,\lambda} - P'_{S,\lambda}\hat{D}_2 \right)\exp(-\hat{D}_1 q^2 t) \\[2em] +\dfrac{1}{\hat{D}_2 - \hat{D}_1}\left(P'_{T,\lambda} - P'_{S,\lambda}\hat{D}_1 \right)\exp(-\hat{D}_2 q^2 t) + \dfrac{\partial n_\lambda}{\partial T} - P'_{S,\lambda} \end{array} \right]^2. \tag{2.30}$$

Here, $P'_{S,\lambda}$ and $P'_{T,\lambda}$ are defined as follows:

$$P'_{S,\lambda} = \left(\frac{\partial n_\lambda}{\partial c_1} \right) S'_{T,1} + \left(\frac{\partial n_\lambda}{\partial c_2} \right) S'_{T,2}, \tag{2.31}$$

$$P'_{T,\lambda} = \left(\frac{\partial n_\lambda}{\partial c_1} \right) D'_{T,1} + \left(\frac{\partial n_\lambda}{\partial c_2} \right) D'_{T,2}. \tag{2.32}$$

Note that the terms in the square bracket of Eq. (2.30) are in the same form as the heterodyne signal of TDFRS (Eq.(23) in Ref. 59), when normalized. Also, $P'_{S,\lambda}$ and $P'_{T,\lambda}$ are related to the asymptotic plateau a, and the initial slope b in Ref. 59, respectively.

2.3.2 Relaxation process by mass diffusion

The concentration amplitudes $\Delta c_i(t)$ in the relaxation process of the concentration distribution ($t \gg \tau_a$) are obtained as Eqs. (2.33) and (2.34). For simplicity, time $t = 0$ is set at the end of heating,

when describing the relaxation process after the heating laser is switched off.

$$\Delta c_1(t) = -\frac{\left(D_{11} - \hat{D}_2\right)\Delta c_1(t_h) + D_{12}\Delta c_2(t_h)}{\hat{D}_2 - \hat{D}_1}\exp(-\hat{D}_1 q^2 t)$$

$$+\frac{\left(D_{11} - \hat{D}_1\right)\Delta c_1(t_h) + D_{12}\Delta c_2(t_h)}{\hat{D}_2 - \hat{D}_1}\exp(-\hat{D}_2 q^2 t), \qquad (2.33)$$

$$\Delta c_2(t) = -\frac{\left(D_{22} - \hat{D}_2\right)\Delta c_2(t_h) + D_{21}\Delta c_1(t_h)}{\hat{D}_2 - \hat{D}_1}\exp(-\hat{D}_1 q^2 t)$$

$$+\frac{\left(D_{22} - \hat{D}_1\right)\Delta c_2(t_h) + D_{21}\Delta c_1(t_h)}{\hat{D}_2 - \hat{D}_1}\exp(-\hat{D}_2 q^2 t). \qquad (2.34)$$

$\Delta c_i(t_h)$ on the right-hand side of Eqs. (2.33) and (2.34) are the concentration amplitudes formed during the heating time t_h. Substituting $t = t_h$ into Eqs. (2.26) and (2.27), $\Delta c_i(t_h)$ in Eqs. (2.33) and (2.34) are obtained. The intensity of the diffracted beam $I_\lambda(t)$ for the diffusion signal can be calculated in the same way as the formation process:

$$I_\lambda(t) \propto \left\{W_\lambda \exp\left[-\hat{D}_1 q^2 t\right] + (1 - W_\lambda)\exp\left[-\hat{D}_2 q^2 t\right]\right\}^2, \qquad (2.35)$$

where the normalized weight W_λ is expressed as

$$W_\lambda = \beta_\lambda + \gamma_\lambda \chi_{1,\lambda}(t_h). \qquad (2.36)$$

β_λ, γ_λ, and $\chi_{1,\lambda}(t_h)$ are described as

$$\beta_\lambda = \frac{-D_{22} + \hat{D}_2 - \left\{(\partial n_\lambda/\partial c_1)/(\partial n_\lambda/\partial c_2)\right\}D_{12}}{\hat{D}_2 - \hat{D}_1}, \qquad (2.37)$$

$$\gamma_\lambda = \frac{-D_{11} + D_{22} - \left\{(\partial n_\lambda/\partial c_2)/(\partial n_\lambda/\partial c_1)\right\}D_{21} + \left\{(\partial n_\lambda/\partial c_1)/(\partial n_\lambda/\partial c_2)\right\}D_{12}}{\hat{D}_2 - \hat{D}_1}, \qquad (2.38)$$

$$\chi_{1,\lambda}(t_h) = \frac{(\partial n_\lambda/\partial c_1)\Delta c_1(t_h)}{(\partial n_\lambda/\partial c_1)\Delta c_1(t_h) + (\partial n_\lambda/\partial c_2)\Delta c_2(t_h)}. \qquad (2.39)$$

Note that Eqs. (2.36)–(2.39) are expressed in forms similar to the equations used in the Rayleigh and Gouy optical interferometric technique [132, 133], and the Taylor dispersion technique [134] for the measurement of the ternary diffusion coefficients.

2.3.3 Fitting models for data evaluation

Considering both homodyne and heterodyne contributions, the fitting model of the output intensity for the relaxation process by the mass diffusion ($t \gg \tau_a$) can be derived from Eqs. (2.18) and (2.35) as:

$$V_\lambda(t) - V_\lambda(\infty) = A \left\{ \begin{matrix} W_\lambda \exp(-\hat{D}_1 q^2 t) \\ +\left(1 - W_\lambda\right) \exp(-\hat{D}_2 q^2 t) \end{matrix} \right\}^2 + D_{\text{sc}} \left\{ \begin{matrix} W_\lambda \exp(-\hat{D}_1 q^2 t) \\ +\left(1 - W_\lambda\right) \exp(-\hat{D}_2 q^2 t) \end{matrix} \right\}, \quad (2.40)$$

in which A is the amplitude factor for the diffracted light, and D_{sc} is that for coherent scattered light. $V(\infty)$ is the baseline output due to the scattered light. The fitting parameters are $\hat{D}_1$, $\hat{D}_2$, W_λ, A, D_{sc}, and $V_\lambda(\infty)$.

For the formation process by the Soret effect ($t \gg \tau_a$), the fitting model can be derived from Eqs. (2.18) and (2.30):

$$V_\lambda(t) - V_\lambda(\infty) = A' \left(\begin{matrix} \left[(\partial n_\lambda / \partial T) + F_\lambda(t)\right]^2 \\ +\left(A / D_{\text{sc}}\right)^{-1} F_\lambda(t_h)\left[(\partial n_\lambda / \partial T) + F_\lambda(t)\right] \end{matrix} \right), \quad (2.41)$$

with

$$F_\lambda(t) = -P'_{S,\lambda} - \frac{1}{\hat{D}_2 - \hat{D}_1} \left(P'_{T,\lambda} - P'_{S,\lambda} \hat{D}_2 \right) \exp\left[-\hat{D}_1 q^2 t \right]$$

$$+ \frac{1}{\hat{D}_2 - \hat{D}_1} \left(P'_{T,\lambda} - P'_{S,\lambda} \hat{D}_1 \right) \exp\left[-\hat{D}_2 q^2 t \right]. \quad (2.42)$$

The fitting parameters are $P'_{S,\lambda}$, $P'_{T,\lambda}$, $\hat{D}_1$, $\hat{D}_2$, A/D_{sc}, $V_\lambda(\infty)$, and the factor of proportionality A'. However, they can be reduced to three: $P'_{S,\lambda}$, $P'_{T,\lambda}$, and A', after determination of $\hat{D}_1$, $\hat{D}_2$, A/D_{sc}, and $V_\lambda(\infty)$ in the analysis of the relaxation signal with Eq. (2.40). The optical contrast factor $\partial n_\lambda/\partial T$ should be evaluated by a refractometer in advance.

2.3.4 Determination of transport coefficients using the two-wavelength technique

With one probing laser, only the diffusion eigenvalues $\hat{D}_1$, $\hat{D}_2$ and the parameters $P'_{S,\lambda}$, $P'_{T,\lambda}$ can be obtained. In contrast, using two probing lasers of different wavelengths, $P'_{S,\lambda}$ and $P'_{T,\lambda}$ of each wavelength can be obtained, which enables to determine the Soret coefficient and thermodiffusion coefficient. From the definition of the $P'_{S,\lambda}$ and $P'_{T,\lambda}$ in Eqs. (2.31) and (2.32), the linear combinations can be described as Eqs. (2.43) and (2.44).

$$\begin{bmatrix} P'_{S,\lambda 1} \\ P'_{S,\lambda 2} \end{bmatrix} = \mathbf{N_c} \begin{bmatrix} S'_{T,1} \\ S'_{T,2} \end{bmatrix}, \tag{2.43}$$

$$\begin{bmatrix} P'_{T,\lambda 1} \\ P'_{T,\lambda 2} \end{bmatrix} = \mathbf{N_c} \begin{bmatrix} D'_{T,1} \\ D'_{T,2} \end{bmatrix}, \tag{2.44}$$

with

$$\mathbf{N_c} = \begin{bmatrix} \partial n_{\lambda 1}/\partial c_1 & \partial n_{\lambda 1}/\partial c_2 \\ \partial n_{\lambda 2}/\partial c_1 & \partial n_{\lambda 2}/\partial c_2 \end{bmatrix}. \tag{2.45}$$

Since the elements of the matrix $\mathbf{N_c}$ can be measured by a refractometer, the Soret coefficients $S'_{T,i}$ and the thermodiffusion coefficients $D'_{T,i}$ can be calculated by Eqs. (2.43) and (2.44), respectively. Note that the measurement becomes difficult when the condition number of the matrix $\mathbf{N_c}$ is large (ill-conditioned) [135]. The Soret coefficient and thermodiffusion coefficient of the third (dependent) component can be obtained by Eq. (1.21).

After obtaining the values of $\hat{D}_1$, $\hat{D}_2$, $S'_{T,i}$ and $D'_{T,i}$, the diffusion coefficients D_{ij} are theoretically calculated with Eqs. (1.19), (1.20), (2.28) and (2.29) .

2.4 Design of instrument for ternary systems

In this section, the SFRS instrument for ternary systems newly designed to detect the mass transport simultaneously by two-wavelength lasers with wavelengths of $\lambda = 403$ nm and $\lambda = 639$ nm will be presented.

2.4.1 Selection of probing wavelengths

In the previous study by the Nagasaka group [125], a red probing laser of with the wavelength of $\lambda = 632.8$ nm and a green heating laser of $\lambda = 514.5$ nm were employed. The new instrument developed in this study for ternary systems is based on that instrument. As the heating laser, CW solid-state laser (Verdi G5 SLM, Coherent) with the wavelength of 531.8 nm, the maximum power of 5 W, and the beam waists of 2.39 mm (horizontal) and 2.17 mm (horizontal) was introduced in

this study. The narrow line width (within 5 MHz) of this laser enables easy formation of an almost ideal interference pattern with high visibility.

A red laser of $\lambda = 639$ nm (OBIS637-140LX-HTK) was selected as one of the two probing lasers to inherit the experimental know-how of the instrument. After the following considerations, another probing laser of $\lambda = 403$ nm (OBIS405-100LX-HTK) was selected from limited choices of commercially available laser wavelengths in visible light region (about 400–800 nm). For example, continuous wave (CW) solid-state laser of OBIS LX/LS (Coherent) are available from UV to IR, with wavelengths at 375, 405, 413, 422, 445, 458, 473, 488, 505, 514, 520, 532, 552, 561, 594, 637, 640, 647, 660, 685, 730, 785, 808 and 980 nm.

As the first thing to consider, the sensitivity of the detector strongly depends on the wavelength. The diffracted beam is typically very weak, and the sensitivity significantly affects the measurement. Photomultiplier tubes are employed in SFRS experiments to detect the diffracted beam of the probing laser because of their high sensitivity and quick responsiveness. Typical photomultiplier tubes for visible light show peak sensitivity around $\lambda = 400$ nm.

Second, the absorption of the sample at the probing wavelength needed to be small, although the addition of the dye is necessary to convert the interference pattern of the heating laser to the temperature distribution. Absorption of the probing laser causes the temperature of the sample to rise at the laser spot, and reduces the intensity of the diffracted light. A sample including the dye (quinizarin) shows an absorption peak at around $\lambda = 470$ nm (Figure 2.2). Thus, the wavelength in this strongly absorbing range should not be used as the probing laser. Note that it is not easy to find other suitable dye besides quinizarin. For example, dye which shows strong red fluorescence affects the measurement.

In addition, most importantly, two probing wavelengths should be separated to utilize the optical dispersion. When the difference of the contrast factors $\partial n_\lambda / \partial c_i$ by the two wavelengths is very small, the matrix $\mathbf{N_c}$ can become ill-conditioned. In this case, small error of the experimentally obtained parameters can generate large error of the Soret coefficient and the thermodiffusion coefficient. Therefore, the elements of matrix $\mathbf{N_c}$ significantly affect the reliability of measurement by the two-wavelength technique. From the Cauchy's equation, which is an empirical relationship between the refractive index and wavelength in the visible wavelength region, the contrast factor is given by [136]:

$$\frac{\partial n_\lambda}{\partial c_i} = A_i + \frac{B_i}{\lambda^2} \, ,$$

(2.46)

where A_i and B_i are dispersion coefficients. As an example, the condition numbers of the ternary benchmark mixture of THN/IBB/nC12 for possible combinations of two wavelengths in visible light region were calculated as listed in Table 2.1. In this calculation, values of A_i and B_i from Ref. 136 (listed in Table 2.2) were used. When the $\lambda = 405$ nm is selected as the second wavelength to be used with the first wavelength of $\lambda = 639$ nm, the smallest condition number of 78 was obtained. This value is as small as the condition number of 62 calculated for the most separated combination in visible light region $\lambda = 403$ nm and $\lambda = 785$ nm.
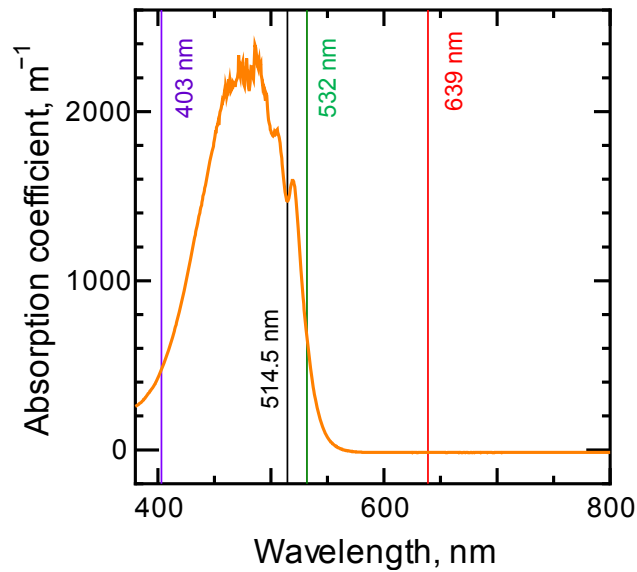
Figure 2.2: Absorption spectrum of the sample (binary benchmark mixture THN/nC12 with the dye of quinizarin).

Table 2.1: Condition numbers calculated for the ternary benchmark mixture of THN/IBB/nC12 with the mass fractions of 0.8/0.1/0.1.

Wavelength 1, nm	Wavelength 2, nm	Condition number (1-norm), –
639	403	78
639	594	601
639	660	1464
639	785	267

Table 2.2: Coefficients of dispersion equations for the ternary benchmark mixture of THN/IBB/nC12 with the mass fractions of 0.8/0.1/0.1 [136].

	A_i, –	B_i, nm^2
$\partial n_\lambda / \partial c_1$	0.1291	6.092×10^3
$\partial n_\lambda / \partial c_2$	0.0779	4.557×10^3

Accordingly, the wavelength of $\lambda = 403$ nm was adopted as the second wavelength to take advantage of the optical dispersion and avoid the absorption peak of quinizarin. This choice is reasonable in terms of the sensitivity of the photomultiplier tubes. Although quinizarin has little absorption at $\lambda = 403$ nm, this effect becomes negligible after introducing the "pulse probing" techinique (see Section 2.4.4 and 3.1.2). Note that the selected combination of $\lambda = 403$ nm and 639 nm is consequently almost identical to the two wavelengths of $\lambda = 405$ nm and 637 nm employed in the OBD technique [58], and $\lambda = 405$ nm and 633 nm in the TDFRS technique [121].

2.4.2 Optical system for simultaneous detection of two-wavelength signals

A. Incidence angle of lasers

The incident angle of the probing lasers $\theta_{B,\lambda}$ should satisfy the Bragg condition, which depends on the wavelength of lasers [99].

$$\theta_{B,\lambda} = \sin^{-1}\left(\frac{\lambda}{2\Lambda}\right). \tag{2.47}$$

The incident angle of the two heating laser beams θ_h, which symmetrically enter to the normal

direction of the sample cell surface, is adjusted to satisfy the designed interference fringe spacing Λ,

$$\theta_{\mathrm{h}} = \sin^{-1}\left(\frac{\lambda_{\mathrm{h}}}{2\Lambda}\right), \tag{2.48}$$

in which λ_{h} is the wavelength of the heating laser.

Figure 2.3 shows the incident optical path to the sample cell designed for the typical fringe spacing of $\Lambda = 5$ μm in SFRS experiments, in which the two probing lasers enter from opposite sides with respect to the normal vector. In addition, the use of a dichroic mirror, which reflects the heating laser and transmits the two probing lasers, enables alignment such that the three lasers can enter the sample cell simultaneously, although the difference in the incident angles of lasers is small.
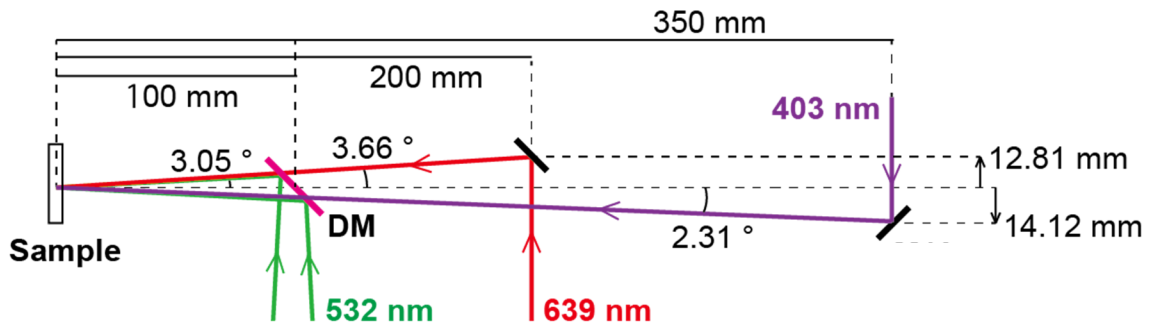
Figure 2.3: Incident beam path designed for simultaneous detection of two-wavelength signals.
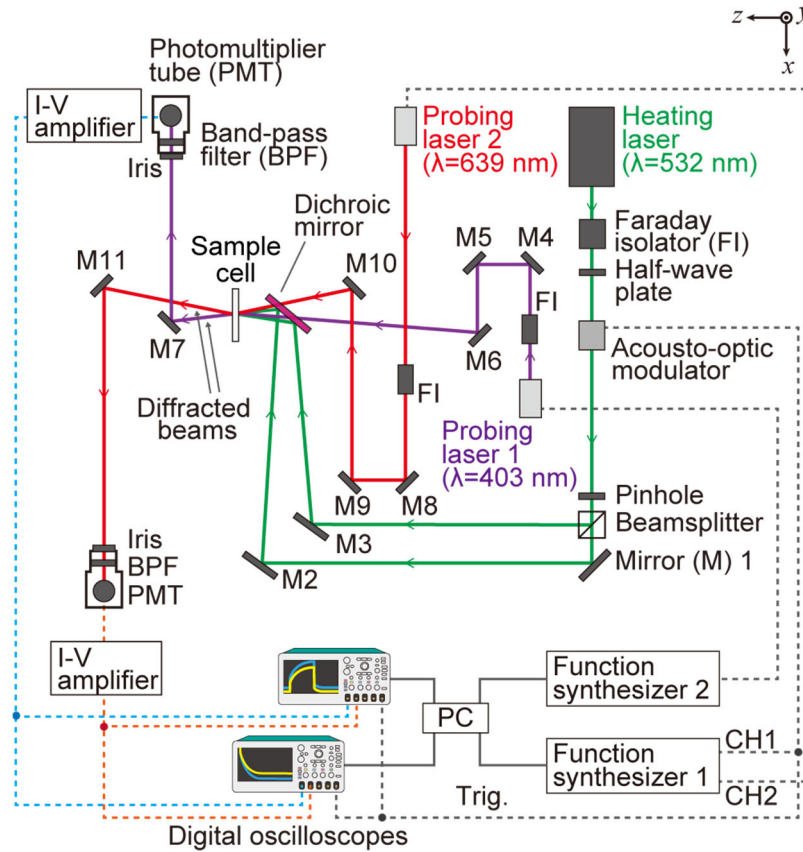
Figure. 2.4: Soret forced Rayleigh scattering instrument developed for ternary systems.

B. Optical system

Figure 2.4 is a schematic of the designed instrument of the Soret forced Rayleigh scattering technique for ternary systems.

In the heating laser system, a Faraday isolator (FI-530-5SV; Qioptiq) is used to protect the heating laser with the wavelength of $\lambda = 531.8$ nm (Verdi G5 SLM; Coherent). Since the isolator rotates the polarization, a half-wavelength plate (#85-037; Edmund Optics) is employed to adjust the polarization to the specification of the acousto-optic modulator (M1133-aQ80L-2; Isomet), which generates the diffracted beam while the modulation voltage is applied. The diffracted beam from the acousto-optic modulator is split into two beams by a non-polarizing beamsplitter, and they interfere in the sample. The two heating beams symmetrically enter to the normal direction of the sample surface. The interference pattern is observed by the laser beam profiler with a resolution of 11.4 nm (NanoScan; Ophir). The sample in the quartz cell of the 0.5-

mm optical path is mounted on the copper block cell holder [125], in which the water from the thermostat bath (NCB-3100; Tokyo Rikakikai) circulated.

The two probing lasers passing through the optical isolators (IO-5-405-LP/M and IO-3-633-LP/M; Thorlabs) enter the sample under the Bragg condition. A dichroic mirror (#47-950; Edmund Optics) is used to reflect the heating laser and transmit the two probing lasers. To detect the diffracted beams of the two-wavelength probing lasers independently, the diffracted beams are aligned so as to enter the different photomultiplier tubes (R9110 for both beams; Hamamatsu Photonics), which were installed in the housings with the bandpass filters (FF01-400/40-25 and FF01-637/7-25; Semrock).

Although in the TDFRS instrument, the diffracted beam was detected after passing through a single-mode optical fiber [103], any fibers are not used here. The single-mode optical fiber is employed in the TDFRS technique to suppress incoherent background light, which is advantageous for heterodyne detection schemes [103]. Königer [121] reported that the lack of a single-mode fiber for $\lambda = 405$ nm might cause problems in two-color TDFRS experiments. The SFRS instrument for the direct (homodyne) detection scheme developed in this study is free from this problem because it was designed without fibers.

2.4.3 Real-time observation and analysis

A real-time observation and analysis for two-wavelength signals can be performed by this instrument. The signals are observed in real time by digital oscilloscopes (DPO3014 and TDS3032B; Tektronix). Variable gain current−voltage amplifiers (DLPCA-200; Femto) amplify the output current from the photomultiplier tubes. By connecting the output signals from two photomultiplier tubes to the multichannel oscilloscopes, the two-wavelength signals can be displayed simultaneously. Signals in the formation and relaxation processes are observed independently via the two oscilloscopes. This enables flexible settings of the intensity and time ranges of the oscilloscope for the relaxation signals. The S/N ratio of the relaxation signals are increased compared to the single oscilloscope observation of both the formation and relaxation process, because of the vertical resolution of the oscilloscope. Data analysis and control of the instruments, including the digital oscilloscopes and the function synthesizers, are carried out by LabVIEW software on a PC. In the SFRS technique, signal acquisition is carried out at intervals

of 4 s, and typically 16–100 signals are averaged to improve the S/N ratio. Measured values can be checked on a PC after every signal averaging and analysis.

2.4.4 Control of probing time (pulsed probing)

The sample with dye (quinizarin) shows little absorption at $\lambda = 403$ nm (Figure 2.2). As Königer [121] pointed out, absorption of the CW probing laser could affect measurements. To reduce this effect, the irradiation time of the probing lasers can be controlled. Figure 2.5 shows an example of the timing chart for the output of function synthesizers, which control the heating and probing time. Output channel 1 of the function synthesizer 1 (WF1956; NF Corp.) is used to control the heating time. The irradiation time of the probing lasers are controlled by output channel 2 of function synthesizer 1, and the output of function synthesizer 2 (SG-4105; Iwatsu). The emission of the probing lasers begins before the heating, and ends after the observation of the mass diffusion. The effect of the pulsed probing will be described in the next chapter (Section 3.1.2).
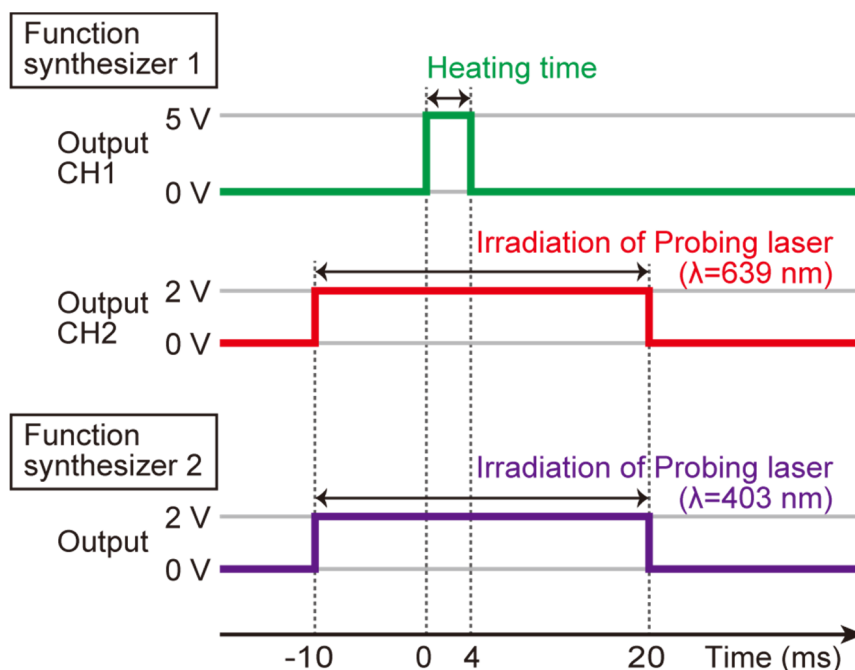
Figure. 2.5: Example of timing chart of function synthesizer output to control laser irradiation time.

3

Validation of instrument by measurement of Soret coefficient in benchmark mixtures

3.1 Binary benchmark mixtures

Before moving on to experiments on ternary systems, measurements on the binary benchmark systems [32] were carried out by the apparatus developed in this study, which was presented in the previous chapter. The validity of the simultaneous detection of the two-wavelength signals by this instrument was evaluated by comparing the experimental result with the benchmark values, which were proposed by Platten *et al.* [32].

3.1.1 Sample

The binary benchmark mixtures were composed of 1,2,3,4-tetrahydronaphthalene (THN, >98%; Acros Organics), isobutylbenzene (IBB, 99.5%; Acros Organics), and *n*-dodecane (*n*C12, 99%; Acros Organics), with an equal mass fraction $(c = 0.500)$. The chemical structures of components in benchmark mixtures are shown in Figure 3.1. The three components of the benchmark mixtures were chosen by Platten *et al.* [32] as the representative of hydrocarbons contained in petroleum reservoir (alkan, one-ring, and two-ring type). Because the Soret effect affects the spatial compositional distribution in an oil reservoir, the study of the Soret effect in this system has been motivated by the oil industry [32]. Note that crude oils contain thousands of different chemical compounds including alkanes, cycloalkanes, and aromatic hydrocarbons [137]. The chemical composition differs depending on producing regions, and aromatic hydrocarbons are usually less abundant than the saturated hydrocarbons [137]. Examples of the composition of crude oils are presented in Table 3.1.

1,2,3,4-tetrahydronaphthalene (THN)   isobutylbenzene (IBB)

n-dodecane (*n*C12)
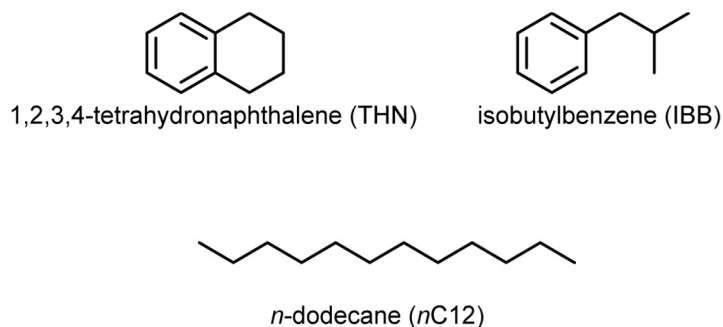
Figure 3.1: Components of benchmark systems.

Table 3.1: Composition of three crude oils [137].

Component	Prudhoe Bay	South Louisiana	Kuwait
Naphtha fraction (wt %)	23.2	18.6	22.7
Alkanes	12.5	8.8	16.2
Cycloalkanes	7.4	7.7	4.1
Aromatic hydrocarbons	3.2	2.1	2.4
Benzenes	0.3	0.2	0.1
Touluene	0.6	0.4	0.4
C8 aromatics	0.5	0.7	0.8
C9 aromatics	0.06	0.5	0.6
C10 aromatics	–	0.2	0.3
C11 aromatics	–	0.1	0.1
Indans	–	–	0.1
High-boiling fraction (wt %)	76.8	81.4	77.3
Saturates	14.4	56.3	34.0
n-Alkans	5.8	5.2	4.7
Isoalkans	–	14.0	13.2
1-ring cycloalkans	9.9	12.4	6.2
2-ring cycloalkanes	7.7	9.4	4.5
3-ring cycloalkans	5.5	6.8	3.3
4-ring cycloalkans	5.4	4.8	1.8
5-ring cycloalkans	–	3.2	0.4
6-ring cycloalkans	–	1.1	–

Table 3.1: (Continued)

Component	Prudhoe Bay	South Louisiana	Kuwait
Aromatic hydrocarbons (wt %)	25.0	16.5	21.9
Benzenes	7.0	3.9	4.8
Indans and tetralins	–	2.4	2.2
Dinaphthenobenzenes	–	2.9	2.0
Naphthalenes	9.9	1.3	0.7
Acenapthenes	–	1.4	0.9
Phenanthrenes	3.1	0.9	0.3
Acenaphthalenes	–	2.8	1.5
Pyrenes	1.5	–	–
Chrysenes	–	–	0.2
Benzothiophenes	1.7	0.5	5.4
Dibenzothiophenes	1.3	0.4	3.3
Indanothiophenes	–	–	0.6
Polar material (wt %)	2.9	8.4	17.9
Insolubles	1.2	0.2	3.5

A small amount ($c = 0.0004$) of inert dye (quinizarin) was added in samples for absorption of the heating laser. The influence of the addition of quinizarin on experiments by the holographic grating technique was examined by Köhler *et al.* [103] and Niwa *et al.* [125], and it was found to be negligible. All chemicals were used without further purification.

3.1.2 CW (continuous wave) and pulsed laser probing

Simultaneous detection of two-wavelength signals was performed on one of the binary benchmark systems: THN/nC12 with the mass fraction of $c = 0.500$ at a temperature of $T = 298.2$ K. In the experiment, the fringe spacing was $\Lambda = 4.93$ μm. Without controlling of the irradiation time of the probing lasers (CW probing), signals were obtained as shown in Figure 3.2. Detected signals were normalized by the intensity contributed by the formation of the temperature gratings. The difference of the normalized signals on the probing wavelengths in the Soret effect process were observed after the formation of temperature grating, which was due to the difference in the optical

3. Validation of instrument by measurement of Soret coefficient in benchmark mixtures

contrast factors $\partial n_\lambda / \partial c_i$ and $\partial n_\lambda / \partial T$ on the wavelength λ.

As mentioned in subsection 2.4.4, absorption of the probing laser could affect a measurement. The pulsed probing technique to reduce this problem was tested on the same sample used in the CW probing experiments (THN/nC12, $c = 0.500$, $T = 298.2$ K). The irradiation time of the probing lasers was controlled based on the timing chart shown in Figure 2.5: the irradiation started 10 ms before the heating, and ended 20 ms after the heating laser was switched off. The signals by the pulsed probing are shown in Figure 3.3. The Soret effect and the mass diffusion were observed, as in the case of the CW probing shown in Figure 3.2.

The effect of the pulsed probing was checked by the measurement of the mass diffusion coefficient. Here, only relaxation signals due to the mass diffusion were focused on, because the mass diffusion coefficient is obtained by the analysis of the relaxation signals before the analysis of the formation signals due to the Soret effect (see section 2.2). To evaluate the effect of the absorption of the probing laser, the dependency of the mass diffusion coefficient on the power of the probing laser was investigated. In the experiment, the power of the probing laser with $\lambda = 403$ nm was changed, while that of the other probing laser ($\lambda = 639$ nm), which is hardly absorbed in
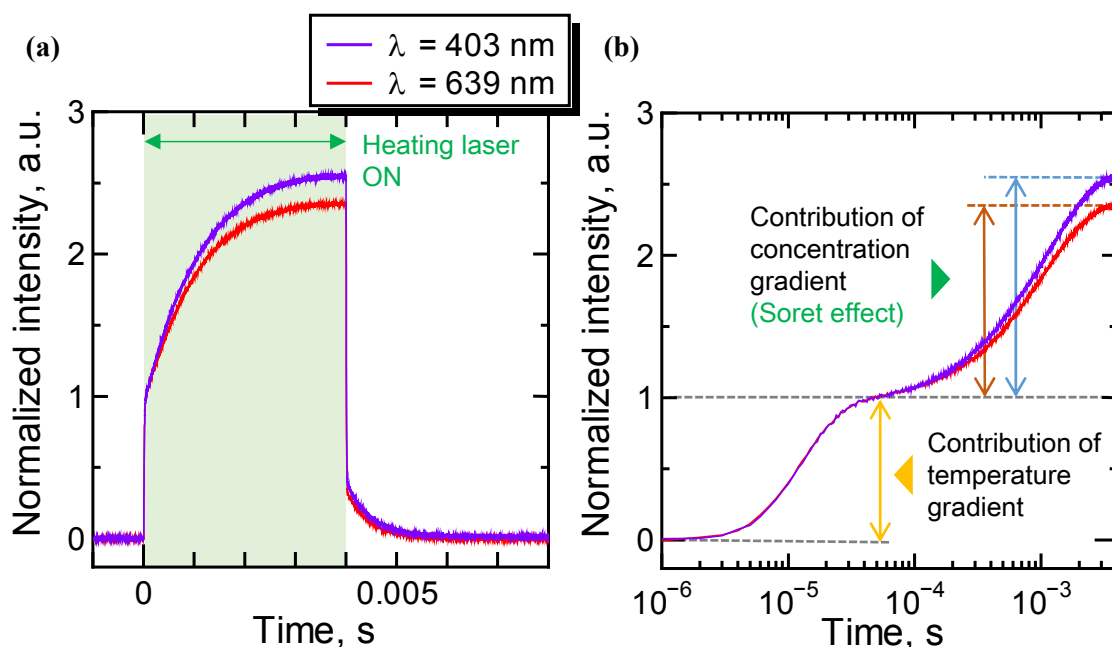
Figure. 3.2: Simultaneously detected two-wavelength signals by CW probing for binary mixture of THN/nC12 ($c = 0.500$, $T = 298.2$ K). (a) Signals in formation and relaxation process; (b) Signals in formation process versus logarithmic time to clarify two modes.
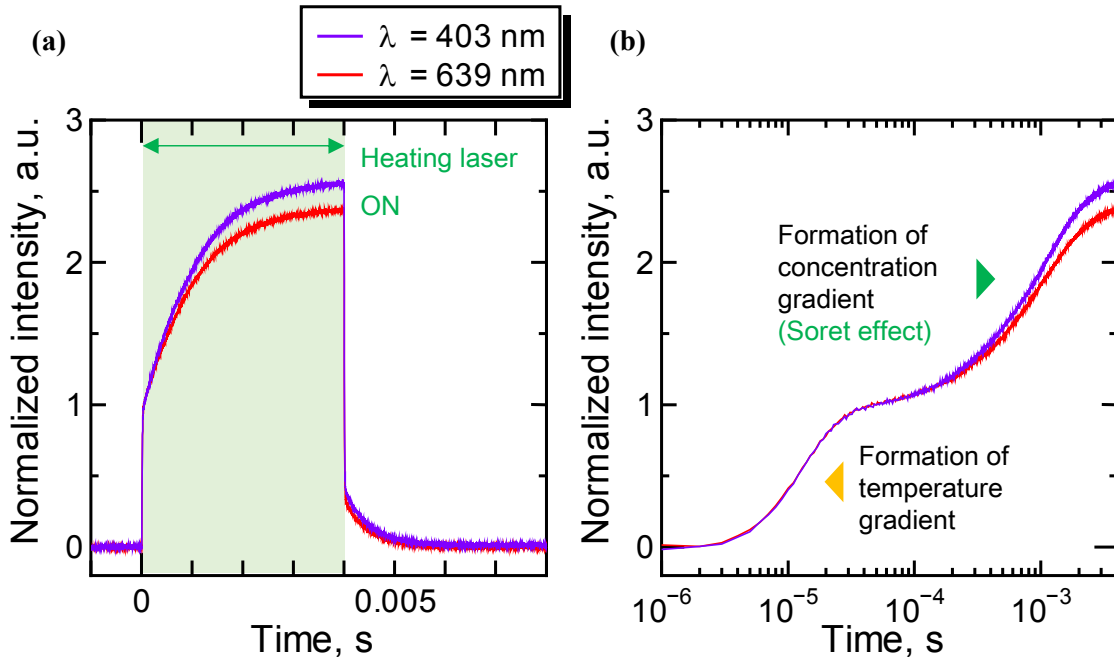
Figure. 3.3: Simultaneously detected two-wavelength signals by pulsed probing for binary mixture of THN/nC12 ($c = 0.500$, $T = 298.2$ K). (a) Signals in formation and relaxation process; (b) Signals in formation process versus logarithmic time to clarify two modes.

the sample, was fixed. The mass diffusion coefficients were obtained by the analysis of the mass diffusion signals based on Eq. (2.19).

　　　As shown in Figure 3.4, the diffusion coefficient obtained by CW probing showed a positive trend with the increase of the probing power of $\lambda = 403$ nm. Since the diffusion coefficient usually trends positive with a rise in temperature [1], this increase by CW probing is considered to be caused by the temperature rise at the laser spot, which is due to the absorption of the probing laser of $\lambda = 403$ nm. On the other hand, the diffusion coefficient measured by pulsed probing was in excellent agreement as the probing power was changed. In addition, there was good agreement between the diffusion coefficients by the two probing lasers. Therefore, it is possible to reduce the effect of the absorption of the probing laser by controlling the probing time. From Eq. (2.5), temperature rise by the absorption of the probing laser of $\lambda = 403$ nm was estimated to be within 0.02 K, when the probing power density was 1.3 W/cm^2 and the probing time was 30 ms.
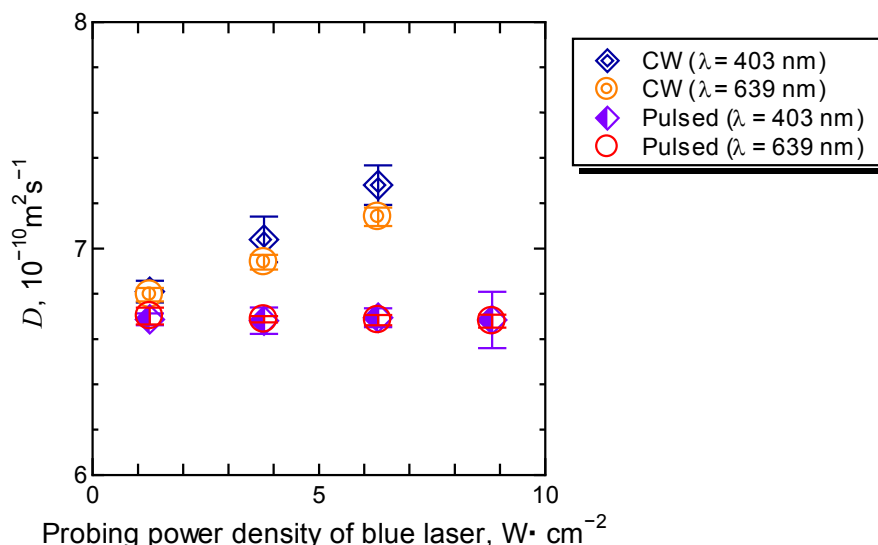
Figure 3.4: Diffusion coefficient D measured by CW and pulsed probing on binary mixtures of THN/nC12 ($c = 0.500$, $T = 298.2$ K) with changing power density of a probing laser ($\lambda = 403$ nm). Error bars are the standard deviation of measurement.

3.1.3 Soret and mass diffusion signals

Pulsed probing measurements were performed on the three binary benchmark mixtures, after confirming the effectiveness. Figure 3.5 compares the signals in the formation process of the three binary benchmark mixtures. Each signal acquisition was repeated 16 times and the signals were averaged to improve the S/N ratio. It was observed that the signals reflected the difference of the transport properties (D, S_T) and the optical properties ($\partial n_\lambda/\partial T$, $\partial n_\lambda/\partial c$) on samples. The Soret coefficient S_T is related to the magnitude of the intensity change in the formation process.

Before the signal analysis of the Soret signals in the formation process based on Eqs. (2.21) and (2.22), the mass diffusion part of the signals was analyzed by using Eq. (2.19) to obtain the mass diffusion coefficient. The examples of the mass diffusion signals are shown in Figure 3.6. The fitting curves of the Soret signals were goodly agreed with the experimental data. The deviation was within 2% (Figure A.2 in Appendix). In the analysis, the part of the signals after 0.1 ms from the start or end of the heating were analyzed to satisfy $t \gg \tau_a$ for the fitting models of Eqs. (2.19) and Eqs. (2.21), (2.22).

(a)

Sample:

THN/nC12

($c = 0.500$).

Fringe spacing:

$\Lambda = 4.96$ µm.

(b)

Sample:

THN/IBB

($c = 0.500$).

Fringe spacing:

$\Lambda = 4.96$ µm

(c)

Sample:

IBB/nC12

($c = 0.500$).

Fringe spacing:

$\Lambda = 4.93$ µm.
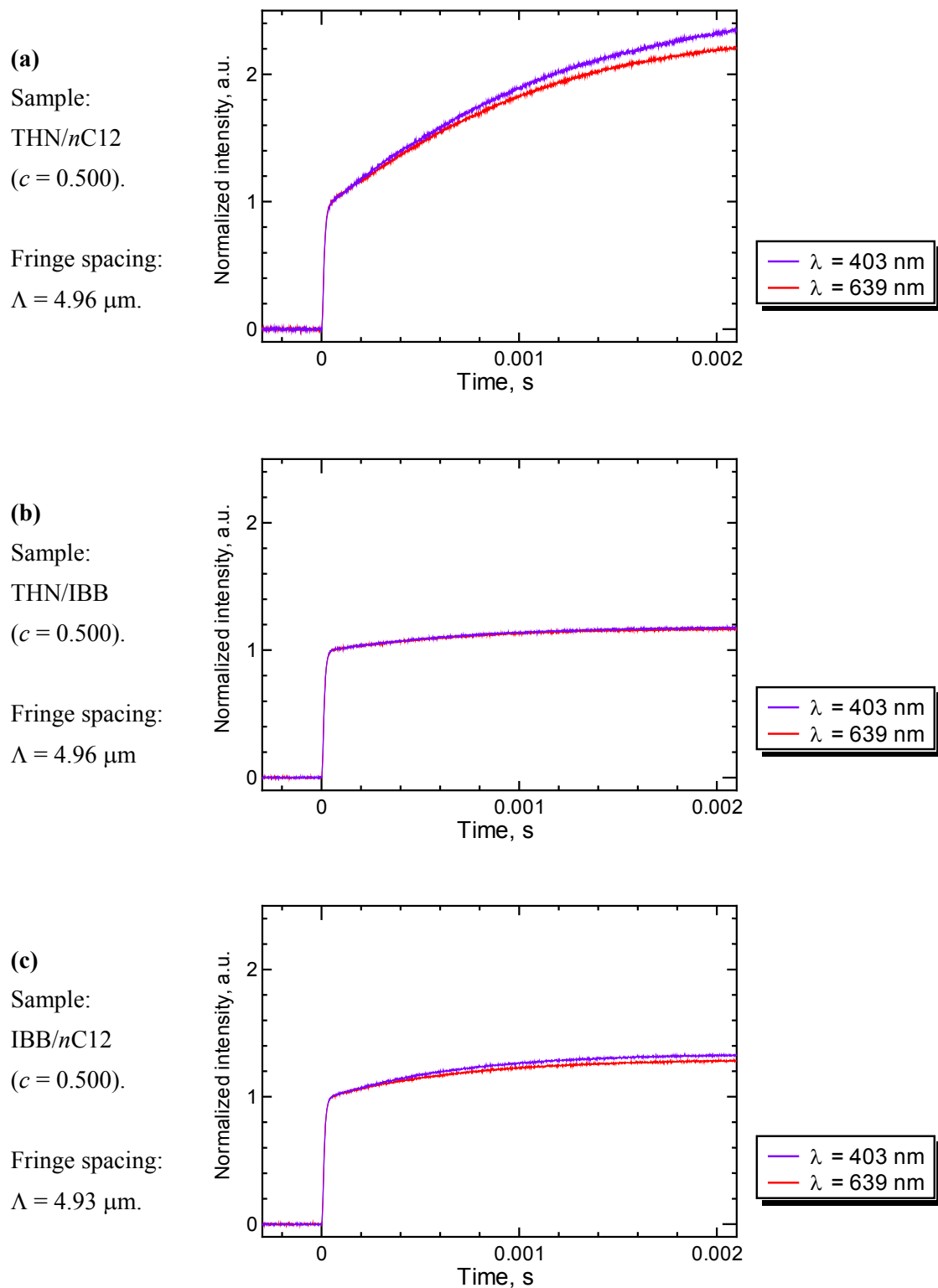
Figure 3.5: 16 times averaged Soret signals of the binary benchmark mixtures at $T = 298.2$ K.

(a)

Sample:

THN/nC12

(c = 0.500).

Fringe spacing:

Λ = 4.96 μm.

(b)

Sample:

THN/IBB

(c = 0.500).

Fringe spacing:

Λ = 4.96 μm

(c)

Sample:

IBB/nC12

(c = 0.500).

Fringe spacing:

Λ = 4.93 μm.
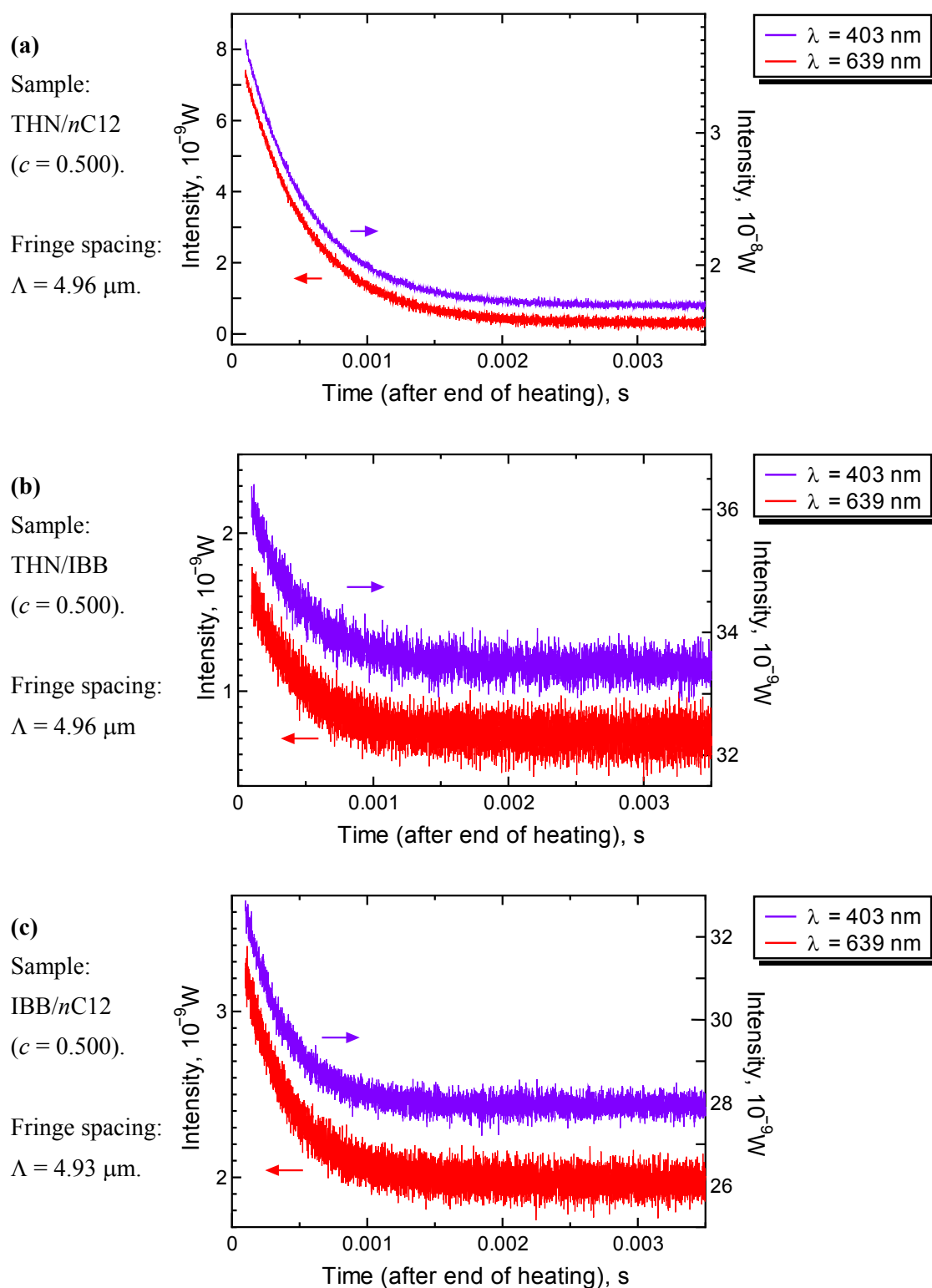
Figure 3.6: 16 times averaged mass diffusion signals of the binary benchmark mixtures at T = 298.2 K.

3.1.4 Results of signal analysis

Table 3.2 lists the measured values and the uncertainties of the mass diffusion coefficient, the Soret coefficient, and the thermodiffusion coefficient of the binary benchmark mixtures. The experimental results by the two-wavelength probing lasers in the present study were in excellent agreement: within 2.0% for the diffusion coefficient, 3.1% for the Soret coefficient, and 5.0% for the thermodiffusion coefficient.

A. Evaluation of Uncertainties

The standard uncertainties of the diffusion coefficient, the Soret coefficient, and the thermodiffusion coefficient were evaluated based on the Guide to the Expression of Uncertainty in Measurement (GUM) [130]. Since the diffusion coefficient D is represented by the fringe spacing Λ and the decay time constant of concentration τ_D in Eq. (2.10), the combined standard uncertainty of diffusion coefficient $u_c(D)$ is expressed by the law of propagation of uncertainty:

$$u_c(D) = \sqrt{\left(\frac{\partial f_D}{\partial \tau_D}\right)^2 u^2(\tau_D) + \left(\frac{\partial f_D}{\partial \Lambda}\right)^2 u^2(\Lambda)} \,, \tag{3.1}$$

where $f_D = (1/\tau_D) \cdot \{\Lambda/(2\pi)\}^2$ is the functional relationship between the measured D and the input quantities. The uncertainty of fringe spacing $u(\Lambda)$ was estimated to be 9.32 nm from the resolution of the beam profiler and the variance of the measurement of Λ at the same condition. The uncertainty of the decay time constant of concentration grating $u(\tau_D)$ was estimated from the variance of τ_D obtained by the analysis of the mass diffusion signals at the same interference fringe Λ. Table 3.3 lists the uncertainty budgets for the mass diffusion coefficient measured by the probing laser of $\lambda = 403$ nm (uncertainty budgets for $\lambda = 639$ nm is listed in Table A.1 in Appendix). The uncertainties $u(D)$ for THN/IBB and IBB/nC12 were larger than that for THN/nC12, which was due to the contribution of $u(\tau_D)$ affected by the S/N ratio of the signals. It should be noted that $u(D)$ can be reduced even further by increasing the number of repetitions for the signals averaging, which was only 16 times in the experiments.

In the curve-fitting analysis of the formation signals to obtain the Soret coefficient based on Eqs. (2.21) and (2.22), the fitting programs evaluate the product of S_T, $c_0(1-c_0)$, $\partial n_\lambda/\partial c$, and $(\partial n_\lambda/\partial T)^{-1}$, which is defined as Γ in Eq. (3.2).

3. Validation of instrument by measurement of Soret coefficient in benchmark mixtures

Table 3.2: Experimental result and standard uncertainties of diffusion coefficient D, Soret coefficient S_T, and thermodiffusion coefficient D_T of binary benchmark mixtures ($c = 0.500$) at $T = 298.2$ K.

Sample	λ, nm	D, 10^{-10} m^{2}s^{-1}	$u(D)$[a], 10^{-10} m^{2}s^{-1}	S_T, 10^{-3} K^{-1}	$u(S_T)$[a], 10^{-3} K^{-1}	D_T, 10^{-12} m^{2}s^{-1}K^{-1}	$u(D_T)$[a], 10^{-12} m^{2}s^{-1}K^{-1}
THN/ nC12	403	6.58	0.03 (0.4%)	9.11	0.06 (0.7%)	5.99	0.05 (0.8%)
	639	6.59	0.03 (0.5%)	9.21	0.06 (0.7%)	6.07	0.05 (0.8%)
THN/ IBB	403	8.41	0.11 (1.3%)	3.20	0.03 (0.8%)	2.70	0.04 (1.6%)
	639	8.26	0.09 (1.1%)	3.11	0.03 (0.9%)	2.57	0.04 (1.4%)
IBB/ nC12	403	10.1	0.12 (1.2%)	3.92	0.04 (0.9%)	3.95	0.06 (1.5%)
	639	9.89	0.06 (0.6%)	3.88	0.03 (0.9%)	3.84	0.04 (1.0%)

[a]$u(D)$, $u(S_T)$, and $u(D_T)$ are the standard uncertainties of the mass diffusion coefficient, the Soret coefficient, and the thermodiffusion coefficient in the measurement.

Table 3.3: Uncertainty budgets for the mass diffusion coefficient in measurement of the binary benchmark mixtures ($c = 0.500$) by the probing laser of $\lambda = 403$ nm at $T = 298.2$ K.

Sample	Uncertainty element x_i	Value of x_i	$u(x_i)$	Sensitivity coefficient $|c_D|$[a]	Contribution to uncertainty of D $|c_D| \times u(x_i)$, 10^{-10} m^{2}s^{-1}
THN/ nC12	τ_D	9.45×10^{-4} s	1.30×10^{-6} s	6.97×10^{-7}	0.009
	Λ	4.96×10^{-6} m	9.32×10^{-6} m	2.66×10^{-4}	0.025
					$u(D) = 0.03 \times 10^{-10}$ m^{2}s^{-1}
THN /IBB	τ_D	7.40×10^{-4} s	9.52×10^{-6} s	1.13×10^{-6}	0.108
	Λ	4.96×10^{-6} m	9.32×10^{-6} m	3.39×10^{-4}	0.032
					$u(D) = 0.11 \times 10^{-10}$ m^{2}s^{-1}
IBB/ nC12	τ_D	6.10×10^{-4} s	6.95×10^{-6} s	1.65×10^{-6}	0.115
	Λ	4.93×10^{-6} m	9.32×10^{-6} m	4.09×10^{-4}	0.038
					$u(D) = 0.12 \times 10^{-10}$ m^{2}s^{-1}

[a]The sensitivity coefficient c_D denotes $\partial f_D / \partial x_i$ in Eq. (3.1) with the uncertainty element x_i.

3. Validation of instrument by measurement of Soret coefficient in benchmark mixtures

$$\Gamma = S_T c_0 (1-c_0) \left(\frac{\partial n_\lambda}{\partial c} \right) \cdot \left(\frac{\partial n_\lambda}{\partial T} \right)^{-1} . \tag{3.2}$$

From Eq. (3.2), the Soret coefficient can be expressed as,

$$S_T = \frac{\Gamma (\partial n_\lambda / \partial T)}{c_0 (1-c_0)(\partial n_\lambda / \partial c)} . \tag{3.3}$$

Considering the uncertainties of Γ, $\partial n_\lambda / \partial c$, and $\partial n_\lambda / \partial T$, the combined standard uncertainty of the Soret coefficient $u_c(S_T)$ is expressed by Eq. (3.4).

$$u_c(S_T) = \sqrt{ \left\{ \frac{\partial f_S}{\partial (\partial n_\lambda / \partial c)} \right\}^2 u^2 \left(\frac{\partial n_\lambda}{\partial c} \right) + \left\{ \frac{\partial f_S}{\partial (\partial n_\lambda / \partial T)} \right\}^2 u^2 \left(\frac{\partial n_\lambda}{\partial T} \right) + \left(\frac{\partial f_S}{\partial \Gamma} \right)^2 u^2(\Gamma) }, \tag{3.4}$$

where f_s is the functional relationship between the measured S_T and the input quantities. The uncertainties of c_0 can be neglected. $u(\Gamma)$ was estimated from the variance of Γ in the experiment.

In this study, the values of $\partial n_\lambda / \partial T$ and $\partial n_\lambda / \partial c$ measured by Gebhardt et al. [138] ($\lambda = $ 405 nm, 633 nm) were used in the analysis of the formation signals. The wavelengths for the measurement of optical contrast factors in Ref. 138 are slightly different from the probing wavelengths of the instrument in this study, which might cause systematic errors. However, this can be ignored because the shift of optical contrast factors due to the deference of the wavelength in a few nanometers is estimated to be small [136] compared to the measurement uncertainties of the optical contrast factors. The uncertainties of the optical contrast factors are not presented in Ref. 138, but it was assumed that they were identical to the errors (4×10^{-4} for $\partial n_\lambda / \partial c$, and 2×10^{-6} for $\partial n_\lambda / \partial T$) described in the paper by Wittko and Köhler [33], which reported the optical contrast factors of the benchmark mixtures measured by the same technique.

Table 3.4 lists the uncertainty budgets for the Soret coefficient measured by the probing laser of $\lambda = 403$ nm (uncertainty budgets for $\lambda = 639$ nm is listed in Table A.2 in Appendix). The contributions of $\partial n_\lambda / \partial c$ and $\partial n_\lambda / \partial T$ to $u(S_T)$ were comparable to that of $u(\Gamma)$ which was evaluated by the experimental data of SFRS. Therefore, not only the performance of the SFRS apparatus but also the accuracy of the optical contrast factors are important to obtain the Soret coefficient with small uncertainties.

The uncertainty of the thermodiffusion coefficient $D_T = S_T \cdot D$ was calculated by the law of propagation of uncertainty.

$$u_c(D_T) = \sqrt{u^2(D) + u^2(S_T)} . \tag{3.5}$$

Table 3.4: Uncertainty budgets for the Soret coefficient in measurement of the binary benchmark mixtures (c = 0.500) by the probing laser of λ = 403 nm at T = 298.2 K.

Sample	Uncertainty element x_i	Value of x_i	$u(x_i)$	Sensitivity coefficient $|c_S|^{[a]}$	Contribution to uncertainty of S_T $|c_S| \times u(x_i)$, 10^{-3}K^{-1}
THN/	Γ	−0.659	2.50×10^{-3}	1.38×10^{-2}	0.035
nC12	$\partial n_\lambda/\partial c$	$0.1337^{[b]}$	$0.0004^{[c]}$	6.81×10^{-2}	0.027
	$\partial n_\lambda/\partial T$	-4.62×10^{-4}K$^{-1[b]}$	0.02×10^{-4}K$^{-1\,[c]}$	19.7	0.039
					$u(S_T) = 0.06 \times 10^{-3}$ K^{-1}
THN/	Γ	−0.0955	3.00×10^{-4}	3.35×10^{-2}	0.010
IBB	$\partial n_\lambda/\partial c$	$0.0601^{[b]}$	$0.0004^{[c]}$	5.33×10^{-2}	0.021
	$\partial n_\lambda/\partial T$	-5.04×10^{-4} K$^{-1\,[b]}$	0.02×10^{-4}K$^{-1\,[c]}$	6.35	0.013
					$u(S_T) = 0.03 \times 10^{-3}$ K^{-1}
IBB/	Γ	−0.157	9.31×10^{-4}	2.50×10^{-2}	0.023
nC12	$\partial n_\lambda/\partial c$	$0.0758^{[b]}$	$0.0004^{[c]}$	5.17×10^{-2}	0.021
	$\partial n_\lambda/\partial T$	-4.73×10^{-4} K$^{-1\,[b]}$	0.02×10^{-4}K$^{-1\,[c]}$	8.28	0.017
					$u(S_T) = 0.04 \times 10^{-3}$ K^{-1}

[a]The sensitivity coefficient c_S denotes $\partial f_S/\partial x_i$ in Eq. (3.4) with the uncertainty element x_i. [b]The optical contrast factors measured by Gebhardt *et al*. [138]. [c]The uncertainties of the optical contrast factors were assumed to be identical to the errors reported by Wittko and Köhler [33].

The experimental results indicated that the measurement of D, S_T, and D_T were performed with small uncertainties: the relative uncertainties were within 1.4%, 1.0%, and 1.6%, respectively.

B. Comparison to benchmark values

The experimental results of D, S_T, D_T are compared to the binary benchmark values [32] in Figures 3.7–3.9. There was good agreement between the benchmark values and the experimental results in the present study. The experimental results on the binary benchmark mixtures showed that the simultaneous two-wavelength observation of the Soret effect and mass diffusion were reasonably performed.
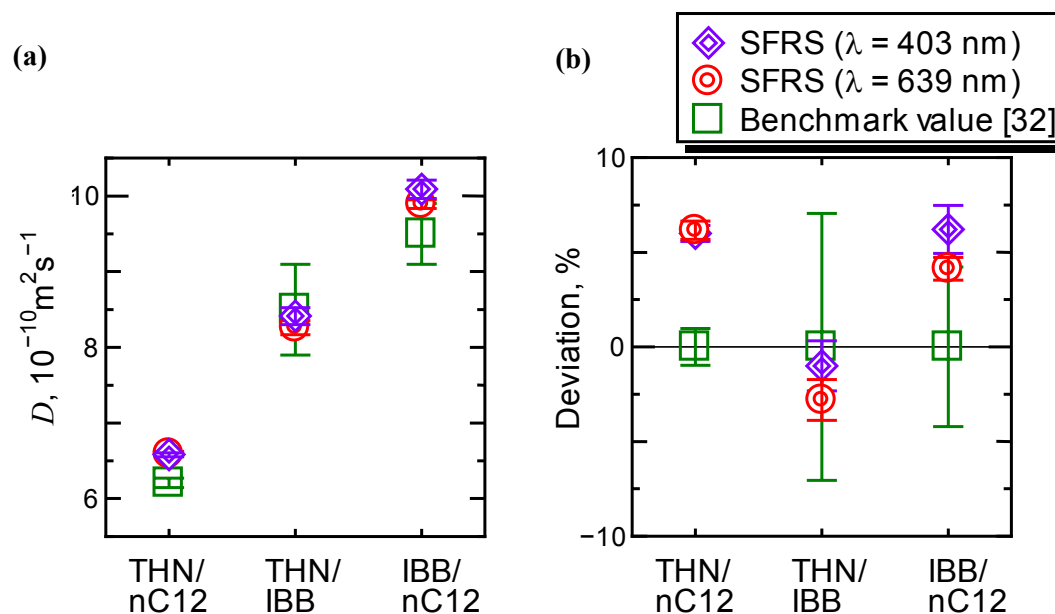
Figure 3.7: Mass diffusion coefficient D of binary benchmark mixtures ($c = 0.500$) at $T = 298.2$ K. (a) Absolute value. (b) Deviation between experimental result and benchmark value. Error bars for SFRS are standard uncertainties.
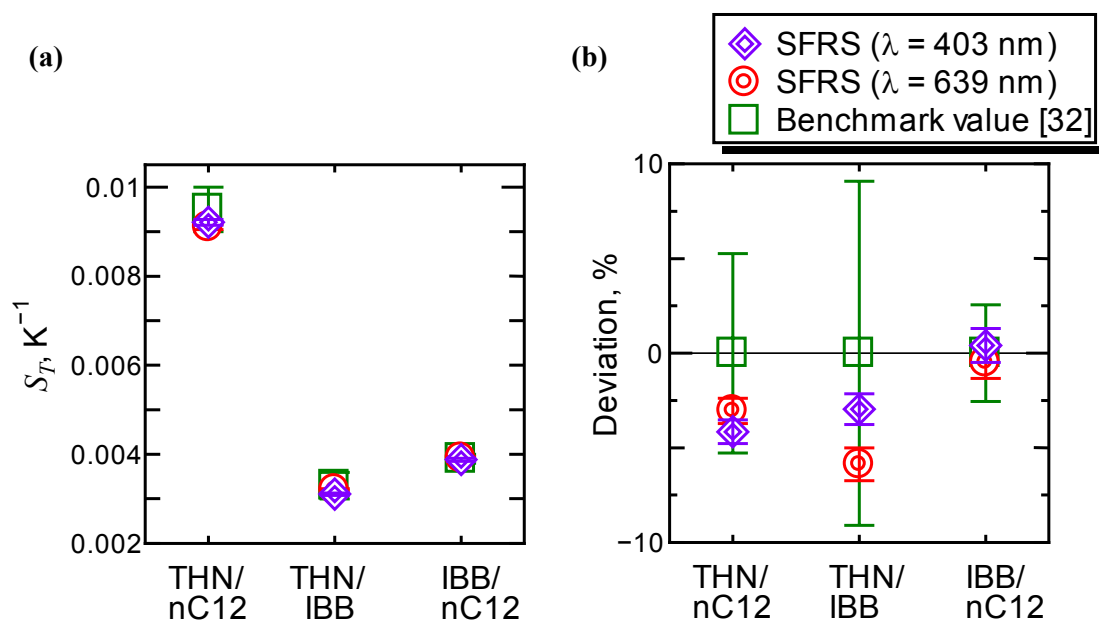
Figure 3.8: Soret coefficient S_T of binary benchmark mixtures ($c = 0.500$) at $T = 298.2$ K. (a) Absolute value. (b) Deviation between experimental result and benchmark value. Error bars for SFRS are standard uncertainties.
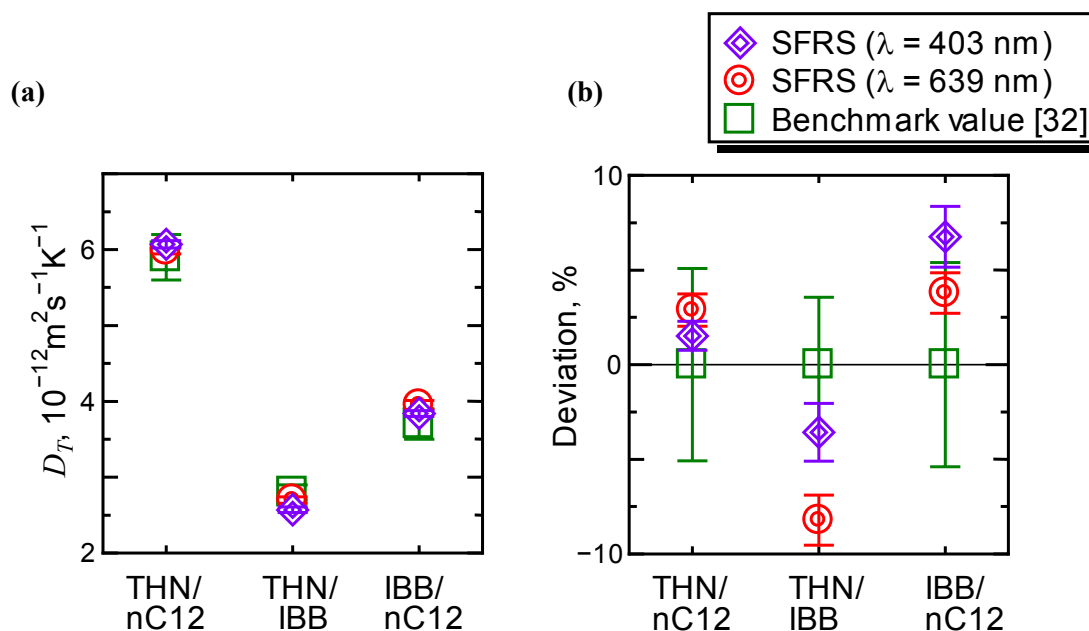
Figure 3.9: Thermodiffusion coefficient D_T of binary benchmark mixtures ($c = 0.500$) at $T = 298.2$ K. (a) Absolute value. (b) Deviation between experimental result and benchmark value. Error bars for SFRS are standard uncertainties.

3.2   Ternary benchmark systems

After confirming the validity of the simultaneous detection of two-wavelength signals by the developed instrument, experiments were carried out on the ternary benchmark mixture to evaluate the performance of the apparatus.

3.2.1 Sample

The ternary benchmark mixture was composed of 1,2,3,4-tetrahydronaphthalene (>98%; Acros Organics), isobutylbenzene (99.5%; Acros Organics), and n-dodecane (99%; Acros Organics), with mass fractions of $c = 0.80$, 0.10, and 0.10, respectively. The benchmark values were proposed by Bou-Ali *et al.* [62] for this ratio, which is a relatively well-conditioned composition for ODI technique [139] contributed to the benchmark campaign. Quinizarin with the mass fraction of $c = 0.0004$ was added in a sample for laser absorption. These chemicals were used without further purification.
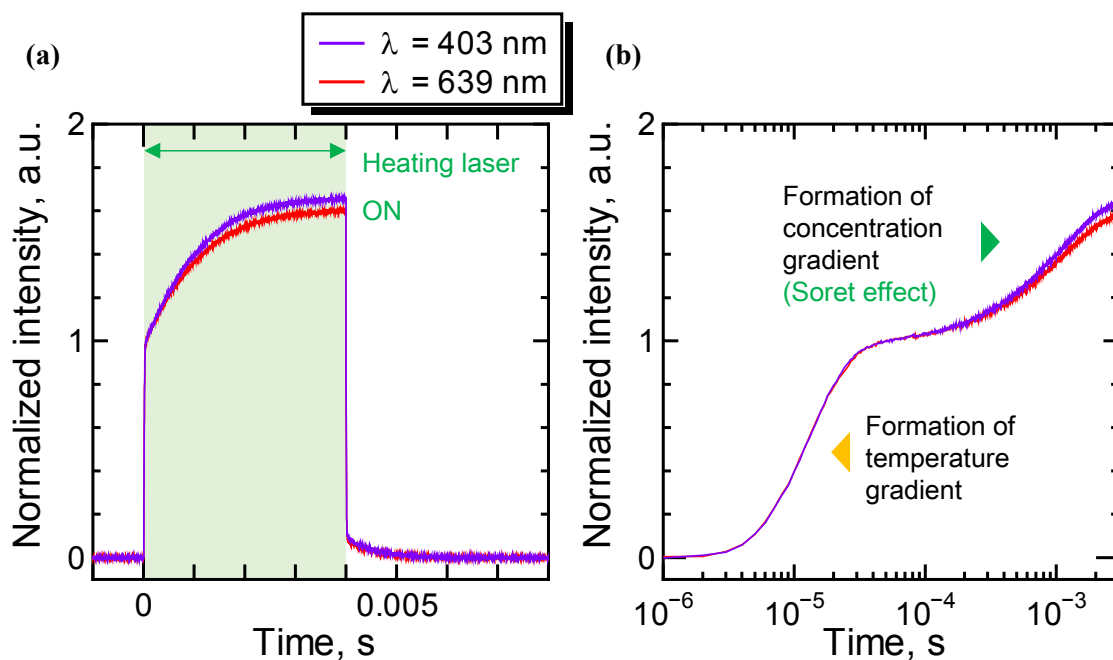
Figure 3.10: Simultaneously detected two-wavelength signals of ternary benchmark mixture THN/IBB/nC12 with mass fractions of 0.80/0.10/0.10 at $T = 298.2$ K. The signal intensity was normalized by the intensity of the temperature grating contribution. (a) Signals in formation and relaxation process; (b) Signals in formation process versus logarithmic time.

3.2.2 Detected signals

Figure 3.10 shows an example of simultaneously obtained two-wavelength signals of the ternary benchmark mixture, which were 16-times averaged. The differences in formation signals on the probing wavelength due to the difference of the optical contrast factors on the wavelength were observed, as in the case of binary benchmark mixtures. The Soret effect signals in the formation process have two modes caused by $\hat{D}_1$ and $\hat{D}_2$ for ternary systems (see Eq. (2.30)), but the detected signals showed the quasi-binary form with one mode, because the two eigenvalues are similar values ($\hat{D}_1 = (5.48 \pm 0.03) \times 10^{-10}$ [m²s⁻¹]) and ($\hat{D}_2 = 6.61 \pm 0.03) \times 10^{-10}$ [m²s⁻¹] [62]) for the ternary benchmark mixture.

3.2.3 Curve fitting

The fitting analysis of the mass diffusion signals in the relaxation process was tried to obtain the diffusion eigenvalues $\hat{D}_1$ and $\hat{D}_2$, but the same values of $\hat{D}_1$ and $\hat{D}_2$ were obtained by the curve-

fitting analysis based on Eq. (2.40). Figure 3.11 shows an example of the mass diffusion signals and the fitting curves. The relaxation signals also showed the quasi-binary form and it was difficult to distinguish the two decaying time constants related to the diffusion eigenvalues. As discussed by Gebhardt and Köhler [59], the individual diffusion eigenvalues cannot be reliably obtained for mixtures of small molecules with similar diffusion eigenvalues, such as the ternary benchmark system.

The obtained diffusion eigenvalues $\hat{D}_1$ (= $\hat{D}_2$) of $(5.91 \pm 0.06) \times 10^{-10}$ $[m^2 s^{-1}]$ for $\lambda = 403$ nm and $(5.81 \pm 0.06) \times 10^{-10}$ $[m^2 s^{-1}]$ for $\lambda = 639$ nm in this study were comparable to the average of the benchmark values of two diffusion eigenvalues. When the fitting analysis was carried out using values of $\hat{D}_1$ and $\hat{D}_2$ fixed to be the benchmark values, the fitting curve also agreed with the detected signals (Figure 3.12). Therefore, reasonable mass diffusion signals were detected in the experiments, although the diffusion eigenvalues were not separately obtained.
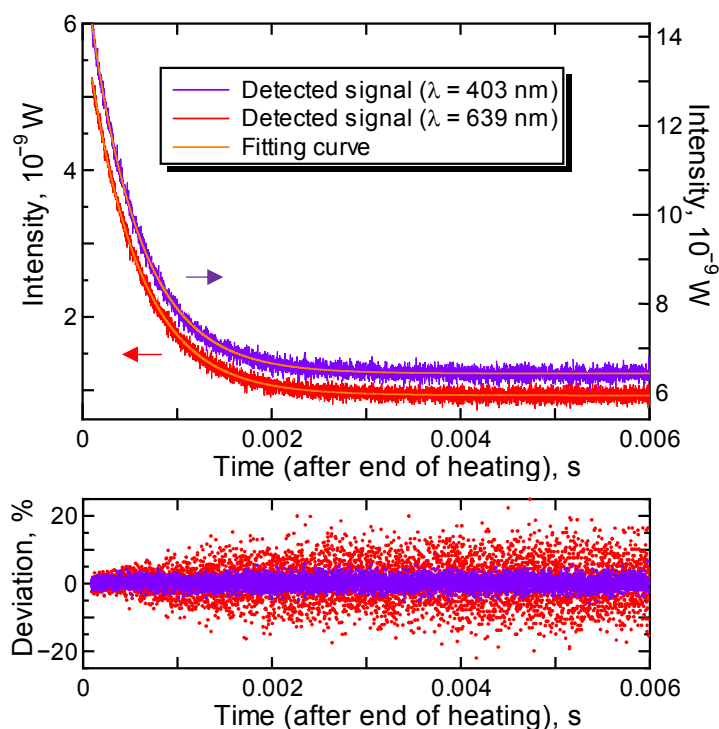
Figure 3.11: Mass diffusion signals and fitting curves of ternary benchmark mixture THN/IBB/nC12 with mass fractions of 0.80/0.10/0.10 at $T = 298.2$ K. Same values of eigenvalues $\hat{D}_1 = \hat{D}_2 = 5.88 \times 10^{-10}$ $[m^2 s^{-1}]$ for $\lambda = 403$ nm and $\hat{D}_1 = \hat{D}_2 = 5.83 \times 10^{-10}$ $[m^2 s^{-1}]$ for $\lambda = 639$ nm were obtained by fitting analysis of presented signals.
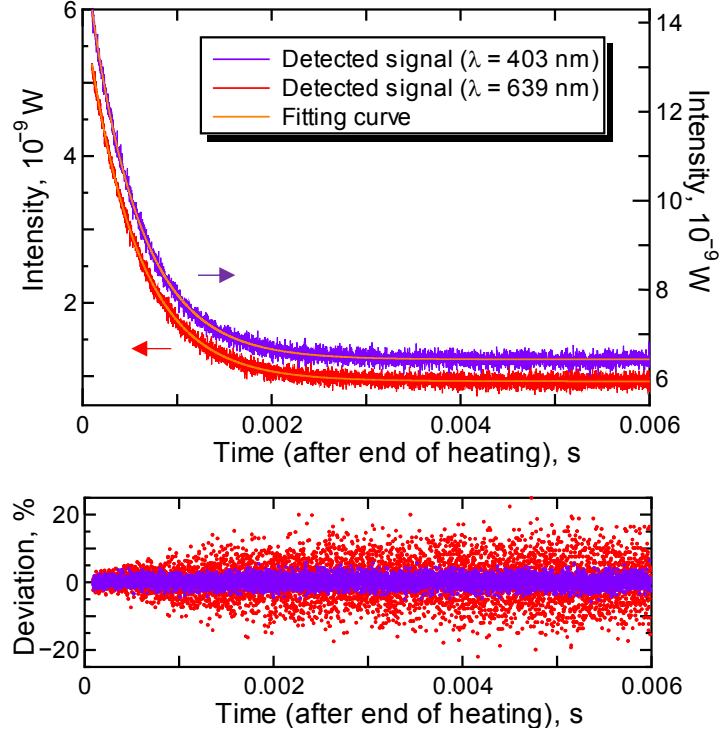
Figure 3.12: Mass diffusion signals and fitting curves of ternary benchmark mixture THN/IBB/nC12 with mass fractions of 0.80/0.10/0.10 at T = 298.2 K. Fitting curves were obtained by analysis using the benchmark values [62] of the diffusion eigenvalues, $\hat{D}_1 = 5.48 \times 10^{-10}$ [m^{2}s^{-1}] and $\hat{D}_2 = 6.61 \times 10^{-10}$ [m^{2}s^{-1}].

Since the eigenvalues were not separately evaluated from the mass diffusion signals, the benchmark values of $\hat{D}_1$ and $\hat{D}_2$ were used for the analysis of the Soret effect signals of the ternary benchmark mixture in this study, although $\hat{D}_1$ and $\hat{D}_2$ obtained by the signals in relaxation process are used in the analysis of the formation process in the developed methodology described in Section 2.3. It can be expected that the separation is reasonably carried out for the ternary systems in which $\hat{D}_1$ and $\hat{D}_2$ differed by an order of magnitude or more, for example, solutions composed of a polymer and two solvents (discussed in the next chapter). Such ternary mixtures can be measured by the SFRS instrument without requirement of the diffusion eigenvalues measured by other techniques, after the optical contrast factors are carefully obtained.

The fitting analysis of the Soret effect signals based on Eqs. (2.41) and (2.42) were carried out with the benchmark values of $\hat{D}_1$ and $\hat{D}_2$ [62], and the optical contrast factors of $\partial n_{405}/\partial T = -4.88 \times 10^{-4}$ [K^{-1}] and $\partial n_{633}/\partial T = -4.63 \times 10^{-4}$ [K^{-1}] measured by Gebhardt and Köhler

[65]. As shown in Figure 3.13, the fitting curves goodly agreed with the experimental data. The parameters $P'_{S,\lambda}$ and $P'_{T,\lambda}$ obtained from the formation signals of the ternary benchmark mixtures are listed in Table 3.5.
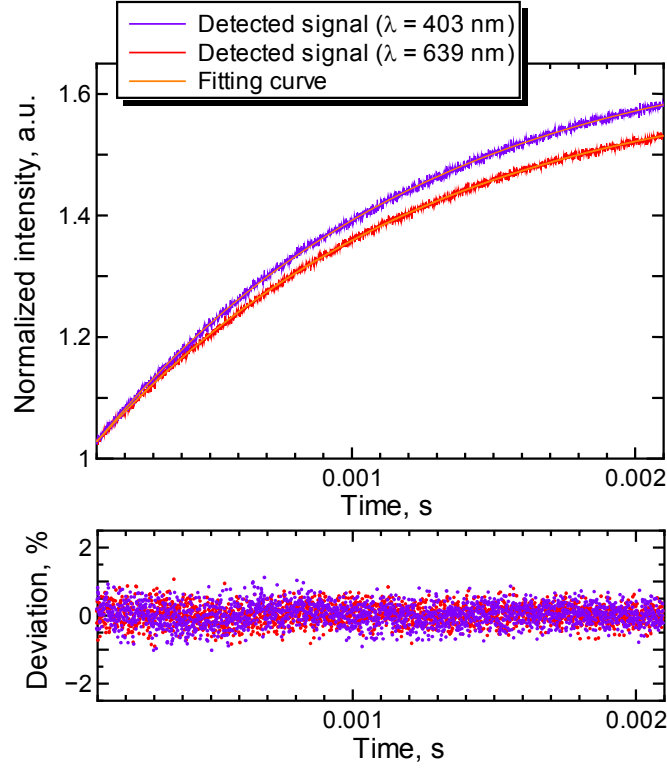
Figure 3.13: Soret effect signals and fitting curves of ternary benchmark mixture THN/IBB/nC12 with mass fractions of 0.80/0.10/0.10 at $T = 298.2$ K.

Table 3.5: Experimental result and standard uncertainties of parameters $P'_{S,\lambda} = (\partial n_\lambda/\partial c_1)S'_{T,1} + (\partial n_\lambda/\partial c_2)S'_{T,2}$ and $P'_{T,\lambda} = (\partial n_\lambda/\partial c_1)D'_{T,1} + (\partial n_\lambda/\partial c_2)D'_{T,2}$ of ternary benchmark mixture THN/IBB/nC12 with mass fractions of 0.80/0.10/0.10 at $T = 298.2$ K.

Probing wavelength λ, nm	$P'_{S,\lambda}$, 10^{-4} K^{-1}	$u(P'_{S,\lambda})$, 10^{-4} K^{-1}	$P'_{T,\lambda}$, 10^{-14} m^{2}s^{-1}K^{-1}	$u(P'_{T,\lambda})$, 10^{-14} m^{2}s^{-1}K^{-1}
403	1.58	0.009	9.59	0.07
		(0.5%)		(0.7%)
639	1.37	0.007	8.28	0.06
		(0.5%)		(0.7%)

The combined standard uncertainty of $P'_{S,\lambda}$ is expressed by Eq. (3.6):

$$
u_c(P'_{S,\lambda i}) = \left[\begin{array}{l} \left(\dfrac{\partial f_P}{\partial \hat{D}_1}\right)^2 u^2(\hat{D}_1) + \left(\dfrac{\partial f_P}{\partial \hat{D}_2}\right)^2 u^2(\hat{D}_2) + \left(\dfrac{\partial f_P}{\partial \Lambda}\right)^2 u^2(\Lambda) \\ + \left\{\dfrac{\partial f_P}{\partial(\partial n_{\lambda i}/\partial T)}\right\} u^2\left(\partial n_{\lambda i}/\partial T\right) + u_{\mathrm{SD}}{}^2(P'_{S,\lambda i}) \end{array} \right]^{1/2} , \qquad (3.6)
$$

where f_P is the functional relationship between $P'_{S,\lambda}$ and the uncertainty elements. $u_{\mathrm{SD}}(P'_{S,\lambda})$ is the uncertainty due to the scattering of $P'_{S,\lambda}$ in the experimental trials, which is calculated by the standard deviation (SD) of $P'_{S,\lambda}$ (A-type evaluation [130]). The standard uncertainty $u(P'_{T,\lambda})$ is described by almost the same equation ($P'_{T,\lambda}$ instead of $P'_{S,\lambda}$). The standard uncertainties of $P'_{S,\lambda}$ and $P'_{T,\lambda}$ were estimated by taking into account relative uncertainties of 0.5% for $u(\hat{D}_1)$ [62], 0.5% for $u(\hat{D}_2)$ [62], 0.2% for $u(\Lambda)$, 0.4% for $u(\partial n_\lambda/\partial T)$ [33], 0.5% for $u_{\mathrm{SD}}(P'_{S,\lambda})$, and 0.7% for $u_{\mathrm{SD}}(P'_{T,\lambda})$.

3.2.4 Soret coefficient and thermodiffusion coefficient

With the values of experimentally obtained $P'_{S,\lambda}$ and $P'_{T,\lambda}$, the Soret coefficient $S'_{T,i}$ and the thermodiffusion coefficient $D'_{T,i}$ were determined by Eqs. (2.43) and (2.44), respectively. The optical contrast factors $\partial n_\lambda/\partial c_i$ by Gebhardt and Köhler [65] were used in this calculation. From three possible choices of independent concentration variables, the combination of $c_1 = c_{n\mathrm{C}12}$ and $c_2 = c_{\mathrm{THN}}$ with the smallest condition number (2-norm) of 50 [65] was adopted.

Table 3.6 shows the experimental results of the Soret coefficient and thermodiffusion coefficient on the ternary benchmark mixture. Note that the thermodiffusion and Soret coefficients with a prime contain the concentration factor $c_1 \times c_2$ [58]. Therefore, when comparing the absolute values of S_T, D_T in binary systems (Table 3.2) to $S'_{T,i}$, $D'_{T,i}$ in ternary systems (Table 3.6), the binary Soret coefficient S_T, and thermodiffusion coefficient D_T should be converted using Eqs. (1.22) and (1.23).

Table 3.6: Experimental results and standard uncertainties of Soret coefficient $S'_{T,i}$ and thermodiffusion coefficient $D'_{T,i}$ of ternary benchmark mixture THN/IBB/nC12 with mass fractions of 0.80/0.10/0.10 at $T = 298.2$ K.

Component i	$S'_{T,i}$, 10^{-3} K^{-1}	$u(S'_{T,i})$, 10^{-3} K^{-1}	$D'_{T,i}$, 10^{-12} m^{2}s^{-1}K^{-1}	$u(D'_{T,i})$, 10^{-12} m^{2}s^{-1}K^{-1}
1 (nC12)	−0.83	0.16	−0.54	0.11
		(19%)		(20%)
2 (THN)	1.14	0.26	0.64	0.19
		(23%)		(30%)
3 (IBB)	−0.30	0.30	−0.095	0.22
		(100%)		(232%)

The combined standard uncertainty of the Soret coefficient $u_c(S'_{T,i})$ for independent components of $i = 1,2$ (nC12 and THN) is expressed by

$$u_c(S'_{T,i}) = \left[\begin{array}{l} \left(\dfrac{\partial f_{S,i}}{\partial P'_{S,\lambda 1}}\right)^2 u^2(P'_{S,\lambda 1}) + \left(\dfrac{\partial f_{S,i}}{\partial P'_{S,\lambda 2}}\right)^2 u^2(P'_{S,\lambda 2}) \\[3mm] + \left\{\dfrac{\partial f_{S,i}}{\partial(\partial n_{\lambda 1}/\partial c_1)}\right\}^2 u^2(\partial n_{\lambda 1}/\partial c_1) + \left\{\dfrac{\partial f_{S,i}}{\partial(\partial n_{\lambda 1}/\partial c_2)}\right\}^2 u^2(\partial n_{\lambda 1}/\partial c_2) \\[3mm] + \left\{\dfrac{\partial f_{S,i}}{\partial(\partial n_{\lambda 2}/\partial c_1)}\right\}^2 u^2(\partial n_{\lambda 2}/\partial c_1) + \left\{\dfrac{\partial f_{S,i}}{\partial(\partial n_{\lambda 2}/\partial c_2)}\right\}^2 u^2(\partial n_{\lambda 2}/\partial c_2) \end{array} \right]^{1/2}, \quad (3.7)$$

where f_S is the functional relationship between the measured $S'_{T,i}$ and the uncertainty elements. The standard uncertainty of the thermodiffusion coefficient is described by almost the same equation ($P'_{T,\lambda}$ replaces $P'_{S,\lambda}$). The combined standard uncertainties of the Soret coefficient $u_c(S'_{T,i})$ and the thermodiffusion coefficient $u_c(D'_{T,i})$ are not small (e.g., 23% for $u_c(S'_{T,\text{THN}})$ and 30% for $u_c(D'_{T,\text{THN}})$), although in the measurement of the binary benchmark mixtures, the uncertainties of the Soret coefficient are within 1% (Table 3.2). The contributions of the uncertainty elements to the uncertainty of the Soret and thermodiffusion coefficients of THN are presented in Table 3.7 (uncertainty budgets of $S'_{T,i}$ and $D'_{T,i}$ of nC12 and IBB are listed in Tables A.3 and A.4 in Appendix). The uncertainties of $P'_{S,\lambda}$ and $P'_{T,\lambda}$ and the optical contrast factors $\partial n_\lambda/\partial c_i$ were less than 1%, but rather large sensitivities produced uncertainties of $S'_{T,i}$ and $D'_{T,i}$ that were not small. Because the Soret coefficient and the thermodiffusion coefficient of the third components IBB

were obtained by Eq. (1.21), the uncertainties of them were evaluated using uncertainties for nC12 and THN (Table A.4). This is why the uncertainties $u(S'_{T,IBB})$ and $u(D'_{T,IBB})$ were relatively large. It should be noted that small errors in uncertainty elements, including the optical contrast factors, can cause large uncertainties of $S'_{T,i}$ and $D'_{T,i}$ in the measurement of ternary systems with the two-wavelength probing technique.

Table 3.7: Uncertainty budgets for the Soret coefficient and thermodiffusion coefficient of 1,2,3,4-tetrahydronaphthalene (THN) in measurement of the ternary benchmark mixture of nC12/THN/IBB with mass fraction $c_1 = c_{nC12} = 0.10$ and $c_2 = c_{THN} = 0.80$ at $T = 298.2$ K.

Uncertainty element x_i	Value of x_i	$u(x_i)$	Sensitivity coefficient to $S'_{T,THN}$ $c_{S,i}$[a]	Contribution to uncertainty of $S'_{T,THN}$ $\|c_{S,i}\| \times u(x_i)$, 10^{-3} K^{-1}	Sensitivity coefficient to $D'_{T,THN}$ $c_{T,i}$	Contribution to uncertainty of $D'_{T,THN}$ $\|c_{T,i}\| \times u(x_i)$, 10^{-12} m^{2}s^{-1}K^{-1}
$\partial n_{405}/\partial c_1$	-0.1059 [65]	0.0004 [33]	-0.142	0.06	-9.29×10^{-11}	0.04
$\partial n_{405}/\partial c_2$	0.0609 [65]	0.0004 [33]	0.199	0.08	1.09×10^{-10}	0.04
$\partial n_{633}/\partial c_1$	-0.0881 [65]	0.0004 [33]	0.170	0.07	1.12×10^{-10}	0.05
$\partial n_{633}/\partial c_2$	0.0555 [65]	0.0004 [33]	-0.239	0.10	-1.31×10^{-10}	0.05
$P'_{S,403}$	1.58×10^{-4} (K^{-1})	0.009×10^{-4} (K^{-1})	-172	0.15	–	–
$P'_{S,639}$	1.37×10^{-4} (K^{-1})	0.007×10^{-4} (K^{-1})	207	0.15	–	–
$P'_{T,403}$	9.59×10^{-14} (m^{2}s^{-1}K^{-1})	0.07×10^{-14} (m^{2}s^{-1}K^{-1})	–	–	-172	0.12
$P'_{T,639}$	8.28×10^{-14} (m^{2}s^{-1}K^{-1})	0.06×10^{-14} (m^{2}s^{-1}K^{-1})	–	–	207	0.12
			$u_c(S'_{T,THN})$	0.26	$u_c(D'_{T,THN})$	0.19

[a]The sensitivity coefficient $c_{S,i}$ denotes $\partial f_S/\partial x_i$ in Eq. (3.7) with the uncertainty element x_i.

3. Validation of instrument by measurement of Soret coefficient in benchmark mixtures

Figures 3.14 and 3.15 compares the ternary benchmark values and the experimental result. The values measured by the SFRS instrument in this study agreed with the benchmark values within 7.5% for the Soret coefficient, and 13% for the thermodiffusion coefficient. The results by the optical digital interferometry (ODI) [61], the optical beam deflection (OBD) [65], and the thermogravitational column (TGC) [66] are also plotted in Figures 3.14 and 3.15. Note that the error bars of the SFRS are the standard uncertainties evaluated based on GUM, while the experimental standard deviations were used for optical techniques of ODI [61] and OBD [65]. As for TGC [66], the uncertainties were determined by taking the errors of the experimental parameters such as the width of the gap in the column into account. Because the contribution of the uncertainties of optical contrast factors are not negligible in the two-wavelength scheme, the error bars for ODI and OBD are considered likely to increase when all dominant uncertainty elements are considered. The experimental results in the present study agreed with the benchmark values within the range of the uncertainties, and the validity of the SFRS instrument developed for ternary systems was confirmed.
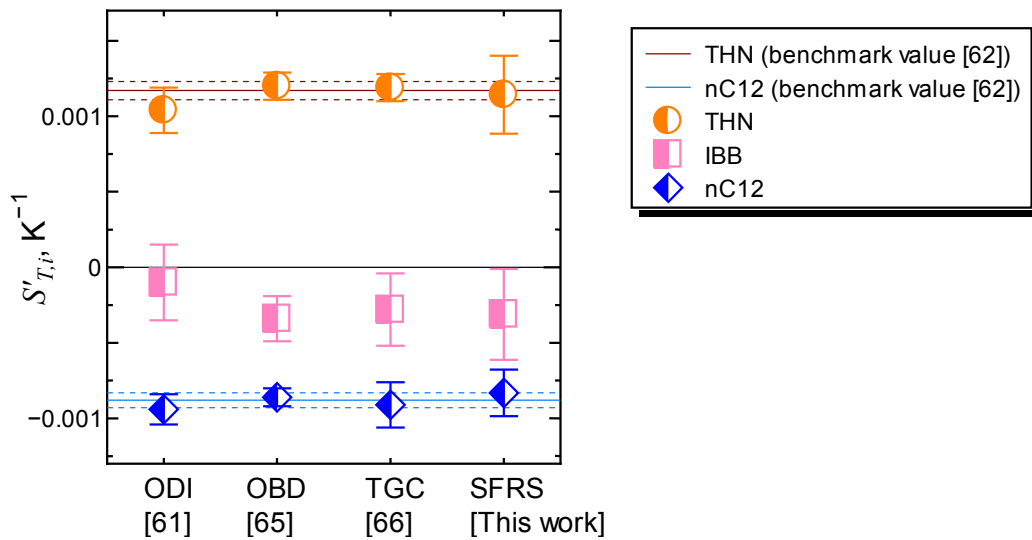
Figure 3.14: Soret coefficient $S'_{T,i}$ of ternary benchmark mixtures of THN/IBB/nC12 with mass fractions of 0.80/0.10/0.10 at $T = 298.2$ K. Experimental results of this work (SFRS) are plotted with benchmark values [62]. Experimental results by the optical digital interferometry (ODI) [61], the optical beam deflection (OBD) [65], and the thermogravitational column (TGC) [66] are also plotted. Error bars of SFRS are standard uncertainties.
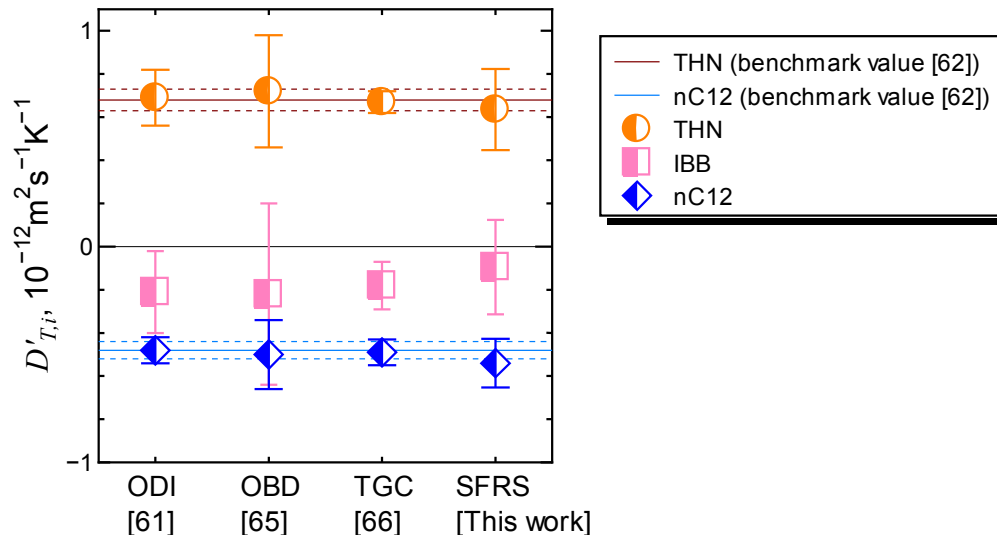
Figure 3.15: Thermodiffusion coefficient $D'_{T,i}$ of ternary benchmark mixtures of THN/IBB/nC12 with mass fractions of 0.80/0.10/0.10 at $T = 298.2$ K. Experimental results of this work (SFRS) are plotted with benchmark values [62]. Experimental results by the optical digital interferometry (ODI) [61], the optical beam deflection (OBD) [65], and the thermogravitational column (TGC) [66] are also plotted. Error bars of SFRS are standard uncertainties.

4

Measurement of Soret coefficient in ternary polymer solutions

4.1 Sample

As an application of the SFRS technique developed in this study, experiments were performed on the ternary polymer solutions of practical interest in engineering, which were composed of cellulose acetate butyrate (CAB), styrene monomer, and 2-butanone. CAB is widely used material for functional polymer films [125,128,129], and styrene monomer and 2-butanone are good solvents of CAB. The chemical structures of the components are shown in Figure 4.1. To prepare samples, commercially available CAB provided from Eastman Chemical (CAB-531-1, acetyl content of 2.8 wt%, butyryl content 50 wt%, and hydroxyl content 1.7 wt%) and small amount ($c =$ 0.0004) of quinizarin were dissolved by ultrasonication in solvents of styrene (Wako, 99.0%) and 2-butanone (Wako, 99.0%). All chemicals were used without further purification. The weight-average molecular weight M_w and the polydispersity M_w/M_n were measured by the gel permeation chromatography (GPC) and found to be $M_w = 49900$ and $M_w/M_n = 2.91$. In this study, several compositions of CAB/styrene/2-butanone with CAB mass fraction of $c_{CAB} = 0.10$ at a temperature $T = 298.2$ K were investigated (Figure 4.2).
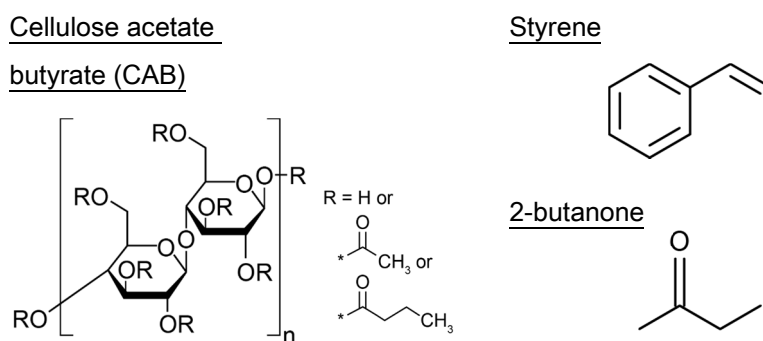
Figure 4.1: Components of ternary polymer solutions.
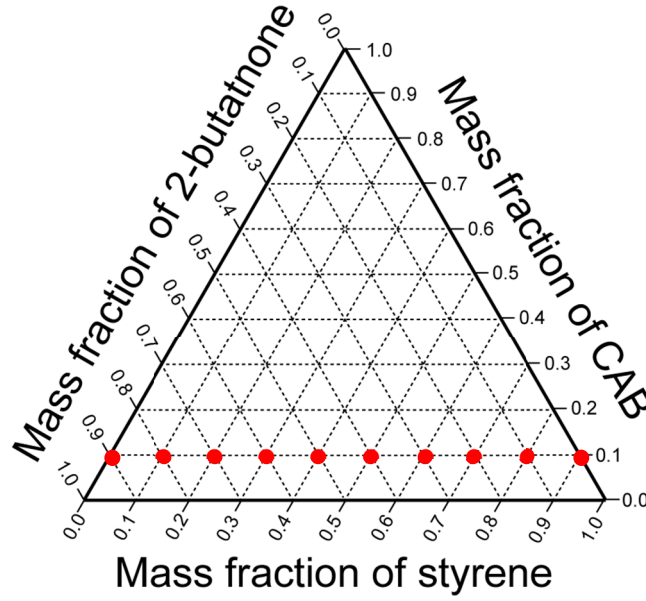
Figure 4.2: Compositions of ternary polymer solutions of CAB/styrene/2-butanone investigated in this work.

4.2 Optical contrast factors

As described in Chapter 2, optical contrast factors $\partial n_\lambda/\partial c_i$, $\partial n_\lambda/\partial T$ are needed to obtain the Soret coefficient.

4.2.1 Concentration derivative and condition numbers

In ternary mixtures, the refractive index with the small change of the mass fractions δc_i can be expressed by Eq. (4.1) [58]:

$$n(c_1 + \delta c_1, c_2 + \delta c_2) = n(c_1, c_2) + \left(\frac{\partial n}{\partial c_1} \right)_{p,T,c_2} \delta c_1 + \left(\frac{\partial n}{\partial c_2} \right)_{p,T,c_1} \delta c_2. \qquad (4.1)$$

The concentration derivatives $\partial n_\lambda/\partial c_i$ were determined by the measurement of the refractive index with one of the two independent concentration is fixed and the other is changed. For example, to determine $\partial n_\lambda/\partial c_1$, c_1 (and the dependent concentration c_3) was changed, while c_2 was fixed.

Refractive induces were measured at two wavelengths with a multi-wavelength Abbe refractometer (DR-M2, Atago). As the light source, $\lambda = 633$ nm from a halogen lamp unit of the refractometer with an interference filter (RE-3526-2, Atago) and $\lambda = 401$ nm from a laser diode

module (CPS405, Thorlabs) were employed. The results of the measurement of refractive index are listed in Table A.5 in Appendix. From the slope of the fitting curve in the graph of n_λ vs c_i shown in Figures A.3–A.5 in Appendix, $\partial n_\lambda/\partial c_i$ were determined as listed in Tables 4.1–4.3. Directions for $(\partial n_\lambda/\partial c_{styrene})_{c\_CAB,T,p}$, $(\partial n_\lambda/\partial c_{CAB})_{c\_2\text{-butanone},T,p}$, and $(\partial n_\lambda/\partial c_{CAB})_{c\_styrene,T,p}$ at the composition of $c_{CAB} = 0.1$, $c_{styrene} = 0.1$, and $c_{2\text{-butanone}} = 0.8$, as an example, are illustrated in Figure 4.3.
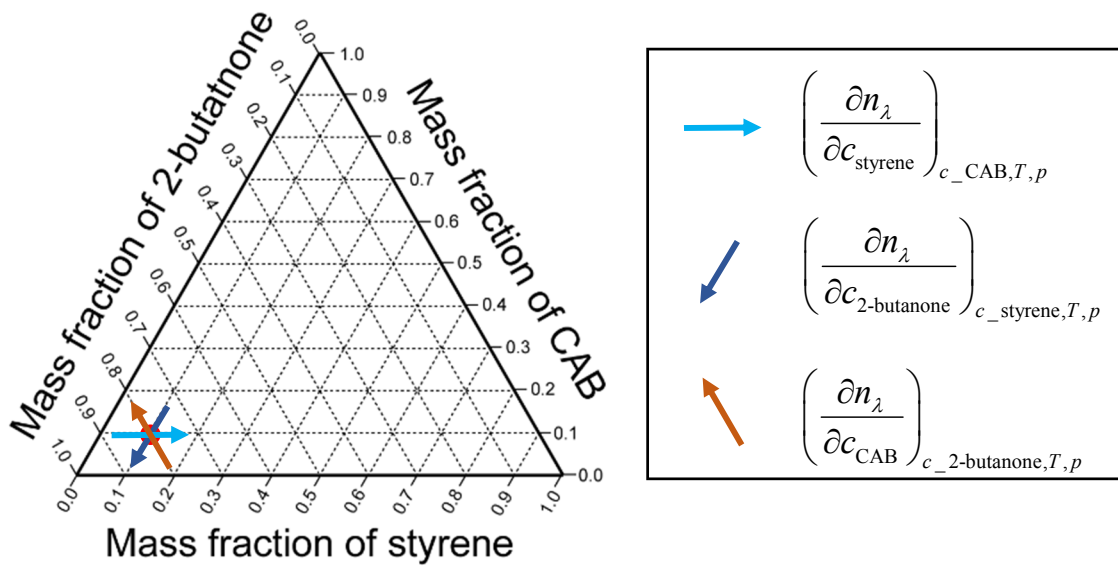
Figure 4.3: Directions for concentration derivatives $\partial n_\lambda/\partial c_i$ of CAB/styrene/2-butanone with the mass fractions of 0.1/0.1/0.8.

Table 4.1: Optical contrast factors $(\partial n_\lambda/\partial c_{\text{styrene}})_{c\_\text{CAB},T,p}$ of ternary polymer solutions of CAB/styrene/2-butanone at $T = 298.2$ K.

c_{CAB}	c_{styrene}	$c_{\text{2-butanone}}$	$\lambda = 401$ nm		$\lambda = 633$ nm	
			$\partial n_\lambda/\partial c_{\text{styrene}}$	$u(\partial n_\lambda/\partial c_{\text{styrene}})$[a]	$\partial n_\lambda/\partial c_{\text{styrene}}$	$u(\partial n_\lambda/\partial c_{\text{styrene}})$
0.10	0	0.90	0.1992	0.0022	0.1629	0.0016
0.10	0.10	0.80	0.2014	0.0021	0.1642	0.0015
0.10	0.20	0.70	0.2036	0.0022	0.1655	0.0016
0.10	0.30	0.60	0.2058	0.0024	0.1668	0.0017
0.10	0.40	0.50	0.2080	0.0027	0.1681	0.0019
0.10	0.50	0.40	0.2102	0.0030	0.1694	0.0021
0.10	0.60	0.30	0.2124	0.0033	0.1707	0.0023
0.10	0.70	0.20	0.2146	0.0037	0.1720	0.0026
0.10	0.80	0.10	0.2168	0.0040	0.1732	0.0029
0.10	0.90	0	0.2190	0.0044	0.1745	0.0031

[a]$u(\partial n_\lambda/\partial c_{\text{styrene}})$ is the standard uncertainties of the optical contrast factor.

Table 4.2: Optical contrast factors $(\partial n_\lambda/\partial c_{\text{CAB}})_{c\_\text{styrene},T,p}$ of ternary polymer solutions of CAB/styrene/2-butanone at $T = 298.2$ K.

c_{CAB}	c_{styrene}	$c_{\text{2-butanone}}$	$\lambda = 401$ nm		$\lambda = 633$ nm	
			$\partial n_\lambda/\partial c_{\text{CAB}}$	$u(\partial n_\lambda/\partial c_{\text{CAB}})$[a]	$\partial n_\lambda/\partial c_{\text{CAB}}$	$u(\partial n_\lambda/\partial c_{\text{CAB}})$
0.10	0	0.90	0.0829	0.0079	0.0819	0.0061
0.10	0.10	0.80	0.0949	0.0075	0.0945	0.0034
0.10	0.20	0.70	0.1044	0.0132	0.0991	0.0139
0.10	0.30	0.60	0.1179	0.0165	0.1083	0.0090
0.10	0.40	0.50	0.1208	0.0085	0.1100	0.0056
0.10	0.50	0.40	0.1269	0.0105	0.1201	0.0077
0.10	0.60	0.30	0.1333	0.0109	0.1214	0.0066
0.10	0.70	0.20	0.1410	0.0135	0.1285	0.0132
0.10	0.80	0.10	0.1362	0.0078	0.1222	0.0114
0.10	0.90	0	–	–	–	–

[a]$u(\partial n_\lambda/\partial c_{\text{CAB}})$ is the standard uncertainties of the optical contrast factor.

Table 4.3: Optical contrast factors $(\partial n_\lambda/\partial c_{CAB})_{c\_2\text{-butanone},T,p}$ of ternary polymer solutions of CAB/styrene/2-butanone at $T = 298.2$ K.

			$\lambda = 401$ nm		$\lambda = 633$ nm	
c_{CAB}	$c_{styrene}$	$c_{2\text{-butanone}}$	$\partial n_\lambda/\partial c_{CAB}$	$u(\partial n_\lambda/\partial c_{CAB})^a$	$\partial n_\lambda/\partial c_{CAB}$	$u(\partial n_\lambda/\partial c_{CAB})$
0.10	0	0.90	–	–	–	–
0.10	0.10	0.80	–0.1056	0.0032	–0.0721	0.0019
0.10	0.20	0.70	–0.1082	0.0069	–0.0740	0.0065
0.10	0.30	0.60	–0.0942	0.0071	–0.0643	0.0032
0.10	0.40	0.50	–0.0917	0.0062	–0.0556	0.0139
0.10	0.50	0.40	–0.0751	0.0017	–0.0478	0.0027
0.10	0.60	0.30	–0.0750	0.0000	–0.0426	0.0057
0.10	0.70	0.20	–0.0777	0.0213	–0.0503	0.0177
0.10	0.80	0.10	–0.0728	0.0118	–0.0454	0.0108
0.10	0.90	0	–0.0740	0.0203	–0.0478	0.0136

[a] $u(\partial n_\lambda/\partial c_{CAB})$ is the standard uncertainties of the optical contrast factor.

  The elements of the matrix $\mathbf{N_c}$ defined in Eq. (2.45) are the optical contrast factors $\partial n_\lambda/\partial c_i$ determined here. $\mathbf{N_c}$ is the coefficient matrix in the simultaneous linear equations of Eqs. (2.43) and (2.44) to determine the Soret coefficient and the thermodiffusion coefficient, respectively. The error amplification of the solution of a simultaneous linear equation $\mathbf{N_c}\mathbf{x} = \mathbf{b}$ can be estimated from the condition number of the matrix $\mathbf{N_c}$ [135]. In this case, the solution vector is $\mathbf{x} = {}^t(S'_{T,1}, S'_{T,2})$ or $\mathbf{x} = {}^t(D'_{T,1}, D'_{T,2})$ and the data vector is $\mathbf{b} = {}^t(P'_{S,\lambda1}, P'_{S,\lambda2})$ or $\mathbf{b} = {}^t(P'_{T,\lambda1}, P'_{T,\lambda2})$. The condition number of $\mathbf{N_c}$ is defined as Eq. (4.2) [65].

$$\text{cond}(\mathbf{N_c}) = \left\|\mathbf{N_c}^{-1}\right\| \cdot \left\|\mathbf{N_c}\right\|, \tag{4.2}$$

$\|\mathbf{N_c}\|$ is the spectral matrix norm of $\mathbf{N_c}$. A problem of $\mathbf{N_c}\mathbf{x} = \mathbf{b}$ with a high condition number of $\mathbf{N_c}$ is said to be ill-conditioned, in which small errors in the data vector can cause significant errors of the solution vector. According to the estimation of Gebhardt and Köhler [65], the condition number (2-norm) should not significantly exceed 10^2.

  Since there are three combinations of the independent mass fractions c_1 and c_2, the following three matrices can be constructed:

$$\mathbf{N_{c1}} = \begin{bmatrix} \partial n_{401}/\partial c_{CAB} & \partial n_{401}/\partial c_{styrene} \\ \partial n_{633}/\partial c_{CAB} & \partial n_{633}/\partial c_{styrene} \end{bmatrix}, \tag{4.3}$$

$$\mathbf{N_{c2}} = \begin{bmatrix} \partial n_{401}/\partial c_{CAB} & \partial n_{401}/\partial c_{2\text{-butanone}} \\ \partial n_{633}/\partial c_{CAB} & \partial n_{633}/\partial c_{2\text{-butanone}} \end{bmatrix}, \tag{4.4}$$

$$\mathbf{N_{c3}} = \begin{bmatrix} \partial n_{401}/\partial c_{styrene} & \partial n_{401}/\partial c_{2\text{-butanone}} \\ \partial n_{633}/\partial c_{styrene} & \partial n_{633}/\partial c_{2\text{-butanone}} \end{bmatrix}. \tag{4.5}$$

$\mathbf{N_{ci}}$ with lowest condition number should be used to obtain the Soret coefficient and the thermodiffusion coefficient with small uncertainties. The calculated values of the condition number of the matrix are listed in Table 4.4 and compared in Figure 4.4. It was found that the condition number is minimum when $c_1 = c_{styrene}$ and $c_2 = c_{2\text{-butanone}}$ are selected. In this case the condition numbers are lower than 21, and it can be said that the ternary systems of CAB/styrene/2-butanone investigated in this study are not ill-conditioned. Note that the condition number (2-norm) for ternary benchmark mixtures of THN/IBB/nC12 was 50 for $\lambda = 405$ nm and 635 nm [65].

Table 4.4: Condition numbers (1-norm) of $\mathbf{N_c}$ for ternary polymer solutions of CAB/styrene/2-butanone at $T = 298.2$ K.

c_{CAB}	$c_{styrene}$	$c_{2\text{-butanone}}$	$\mathbf{N_{c1}}$ $c_1 = c_{CAB}$, $c_2 = c_{styrene}$	$\mathbf{N_{c2}}$ $c_1 = c_{CAB}$, $c_2 = c_{2\text{-butanone}}$	$\mathbf{N_{c3}}$ $c_1 = c_{styrene}$, $c_2 = c_{2\text{-butanone}}$
0.10	0	0.90	31	40	12
0.10	0.10	0.80	39	41	14
0.10	0.20	0.70	46	45	18
0.10	0.30	0.60	48	29	15
0.10	0.40	0.50	34	41	17
0.10	0.50	0.40	44	29	16
0.10	0.60	0.30	41	44	20
0.10	0.70	0.20	47	41	20
0.10	0.80	0.10	31	40	12
0.10	0.90	0	39	41	14
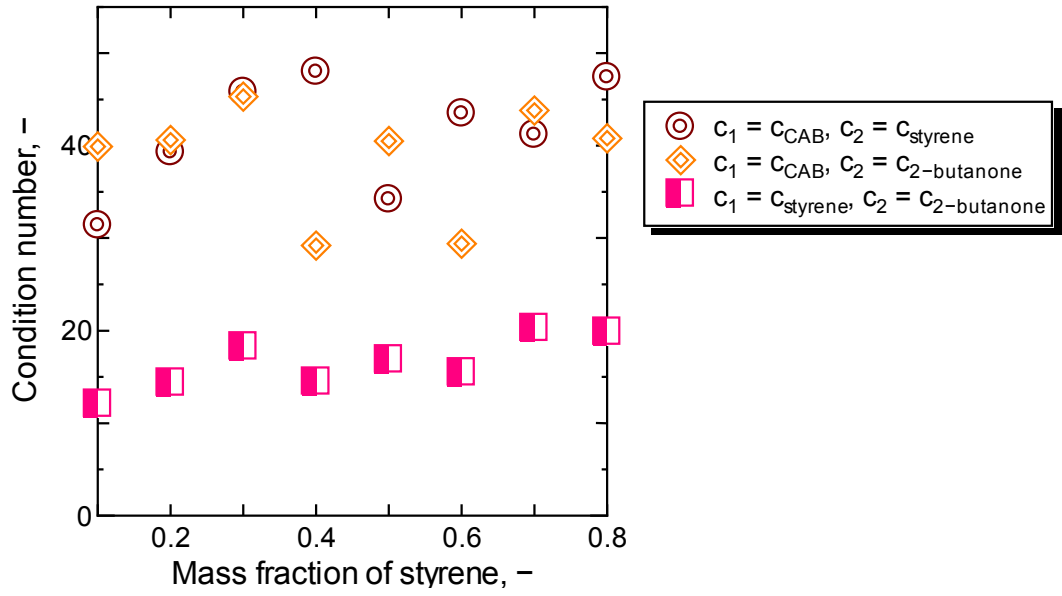
Figure 4.4: Condition numbers (1-norm) of $\mathbf{N_c}$ for ternary polymer solutions of CAB/styrene/2-butanone with $c_{CAB} = 0.10$ at $T = 298.2$ K.

Table 4.5: Optical contrast factors $\partial n_\lambda/\partial T$ of ternary polymer solutions of CAB/styrene/2-butanone at $T = 298.2$ K.

c_{CAB}	$c_{styrene}$	$c_{2\text{-butanone}}$	$\lambda = 401$ nm		$\lambda = 633$ nm	
			$\partial n_\lambda/\partial T$, 10^{-4}K^{-1}	$u(\partial n_\lambda/\partial T)^{a}$, 10^{-4}K^{-1}	$\partial n_\lambda/\partial T$, 10^{-4}K^{-1}	$u(\partial n_\lambda/\partial T)$, 10^{-4}K^{-1}
0.10	0	0.90	−5.36	0.10	−5.20	0.07
0.10	0.10	0.80	−5.49	0.12	−5.25	0.06
0.10	0.20	0.70	−5.50	0.07	−5.19	0.09
0.10	0.30	0.60	−5.94	0.12	−5.44	0.12
0.10	0.40	0.50	−5.88	0.06	−5.45	0.12
0.10	0.50	0.40	−6.18	0.14	−5.50	0.06
0.10	0.60	0.30	−5.80	0.10	−5.35	0.06
0.10	0.70	0.20	−5.99	0.10	−5.42	0.08
0.10	0.80	0.10	−6.06	0.10	−5.43	0.10
0.10	0.90	0	−6.29	0.07	−5.61	0.07

[a] $u(\partial n_\lambda/\partial T)$ is the standard uncertainties of the optical contrast factor.

4.2.2 Temperature derivative

To determine the temperature derivative $\partial n_\lambda / \partial T$ of the ternary polymer solutions of CAB/styrene/2-butanone, the temperature dependence of the refractive index was measured with the Abbe refractometer within the temperature range of (283.2 to 313.2) K. The results of the measurement of refractive index are listed in Tables A.6 and A.7 in Appendix. From linear regression to the relationship between n_λ and T, $\partial n_\lambda / \partial T$ were determined as listed in Table 4.5.

4.3　Result of measurements

Two-wavelength signals of the ternary polymer solutions of CAB/styrene/2-butanone were detected by the experimental apparatus developed in this study at $T = 298.2$ K. Figure 4.5 compares the normalized signals on the compositions. As the ratio of the mass fraction of styrene increased, the magnitude of intensity change in the Soret effect signals decreased and the slope turned to be negative.
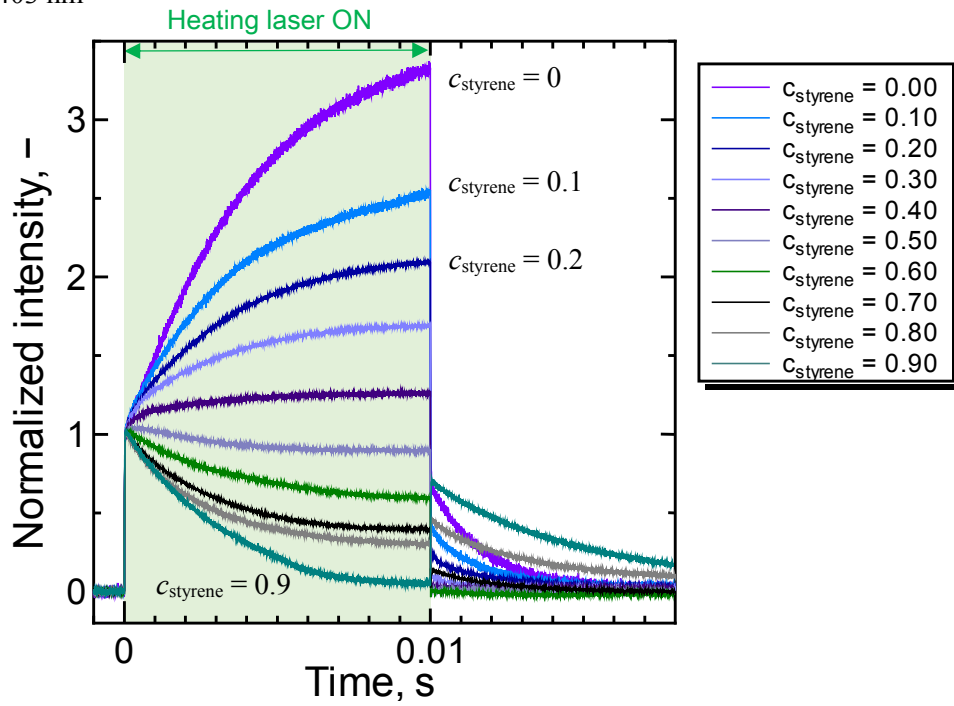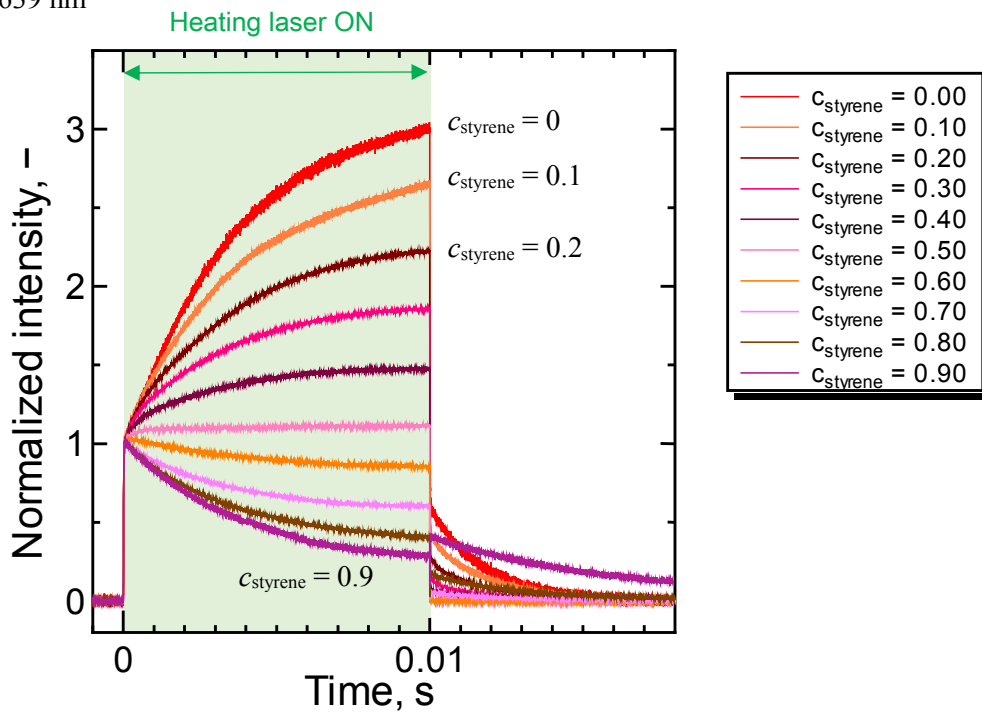
(a) $\lambda = 403$ nm

(b) $\lambda = 639$ nm

Figure 4.5: Detected signals of CAB/styrene/2-butanone at $T = 298.2$ K. The mass fraction of CAB was fixed to be $c_{CAB} = 0.10$ and the ratio of the solvents was changed. (a) $\lambda = 403$ nm; (b) $\lambda = 639$ nm.

4.3.1 Analysis of mass diffusion signals in relaxation process

Figure 4.6 shows examples of mass diffusion signals of the ternary polymer solutions of CAB/styrene/2-butane. Relaxation signals due to mass diffusion were observed except for samples with close mass fractions of two solvents (Figure 4.6(b)). Fitting analysis of the mass diffusion signals based on Eq. (2.40) was carried out to obtain the diffusion eigenvalues $\hat{D}_1$ and $\hat{D}_2$, whereas Eq. (2.19) was employed for the binary polymer solutions of CAB/styrene and CAB/2-butanone with c_{CAB}=0.10.
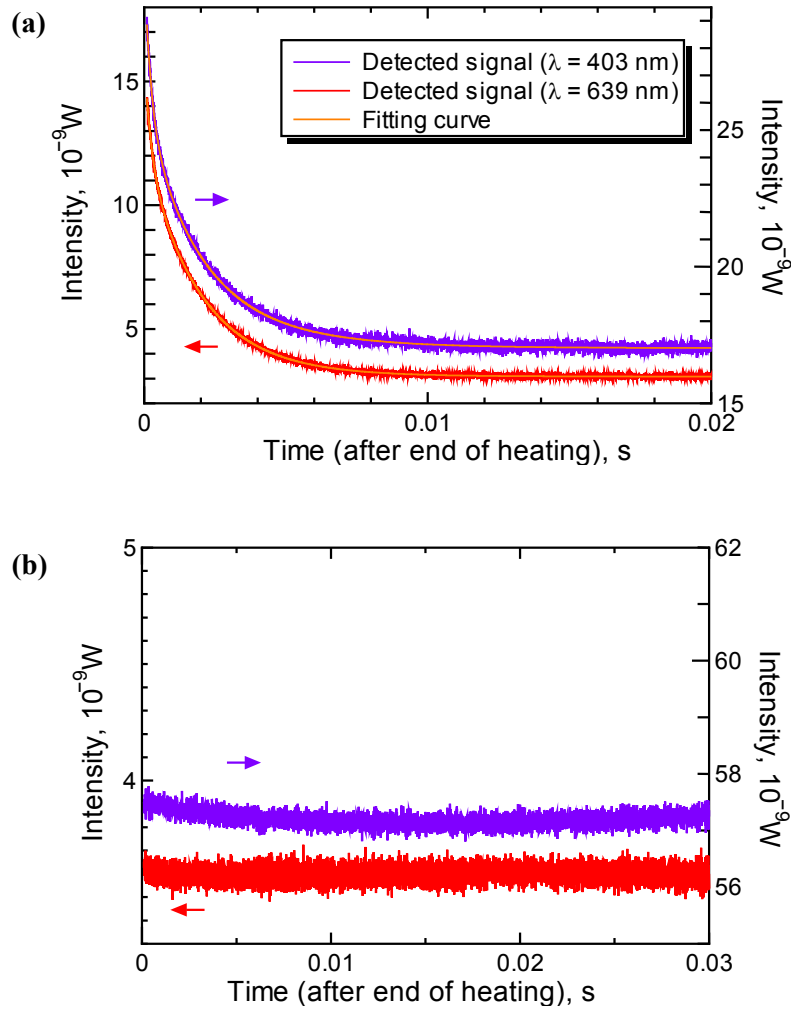
Figure 4.6: Example of mass diffusion signals of CAB/styrene/2-butanone at T = 298.2 K. (a) mass fractions of 0.10/0.30/0.60; (b) mass fractions of 0.1/0.50/0.40.

Table 4.6 lists the result of fitting analysis, in which the two eigenvalues were obtained in different order: 10^{-10} [m^{2}s^{-1}] for $\hat{D}_1$ and 10^{-9} [m^{2}s^{-1}] for $\hat{D}_2$. The slower relaxation mode characterized by $\hat{D}_1$ can be attributed to mass diffusion of polymer into solvent, because obtained values of $\hat{D}_1$ were comparable to the binary mass diffusion coefficient listed in Table 4.7 and $\hat{D}_1$ changed between the two mass diffusion coefficients, as shown in Figure 4.7. The faster mode characterized by another eigenvalue $\hat{D}_2$ can be attributed to mass diffusion of solvents. Note that the relaxation mode due to the heat diffusion was sufficiently faster than the two mass diffusion modes and it can be separated, as shown in Figure 4.8. Obtained value of $\hat{D}_2$ for $c_{styrene} = 0.6$ in Figure 4.7 may not seem to agree with the compositional tendency, which is probably due to the small intensity of the detected signals at this composition.

A fitting curve obtained by the analysis using the fitting model for binary systems Eq. (2.19) is also shown in Figure 4.8, which did not reproduce the faster mass diffusion mode characterized by $\hat{D}_2$. On the other hand, the fitting curve obtained using Eq. (2.40) agreed with the experimental data. Therefore, it was shown that the two mass diffusion modes due to $\hat{D}_1$ and $\hat{D}_2$, which are characteristic to ternary systems, was reasonably evaluated by the mass diffusion signals obtained by the experimental apparatus developed in this study.

Table 4.6: Diffusion eigenvalues $\hat{D}_i$ of CAB/styrene/2-butanone at $T = 298.2$ K.

			$\hat{D}_1$, 10^{-10}m^{2}s^{-1}		$\hat{D}_2$, 10^{-9}m^{2}s^{-1}	
c_{CAB}	$c_{styrene}$	$c_{2\text{-butanone}}$	$\lambda = 403$ nm	$\lambda = 639$ nm	$\lambda = 403$ nm	$\lambda = 639$ nm
0.10	0.10	0.80	1.72 ± 0.04[a]	1.74 ± 0.03	2.78 ± 0.21	2.75 ± 0.23
0.10	0.20	0.70	1.67 ± 0.03	1.67 ± 0.04	2.62 ± 0.09	2.47 ± 0.18
0.10	0.30	0.60	1.64 ± 0.06	1.61 ± 0.04	2.60 ± 0.08	2.43 ± 0.06
0.10	0.40	0.50	–	1.54[b]	–	2.25[b]
0.10	0.60	0.30	–	1.46 ±0.02	–	2.28 ± 0.15
0.10	0.70	0.20	1.22 ± 0.02	1.21 ± 0.02	1.37 ± 0.11	1.46 ± 0.23
0.10	0.80	0.10	0.980 ± 0.012	0.969 ± 0.012	1.51 ± 0.06	1.61 ± 0.07

[a]Standard deviation (SD) of measurement. [b]Fitting result of one signal and SD is not described.

Table 4.7: Mass diffusion coefficient D of CAB/2-butanone and CAB/styrene at $T = 298.2$ K.

c_{CAB}	$c_{styrene}$	$c_{2\text{-butanone}}$	D, 10^{-10}m^{2}s^{-1}	
			$\lambda = 403$ nm	$\lambda = 639$ nm
0.10	0	0.90	1.89 ± 0.05[a]	1.89 ± 0.02
0.10	0.90	0	0.562 ± 0.028	0.571 ± 0.013

[a]Standard deviation of measurement.
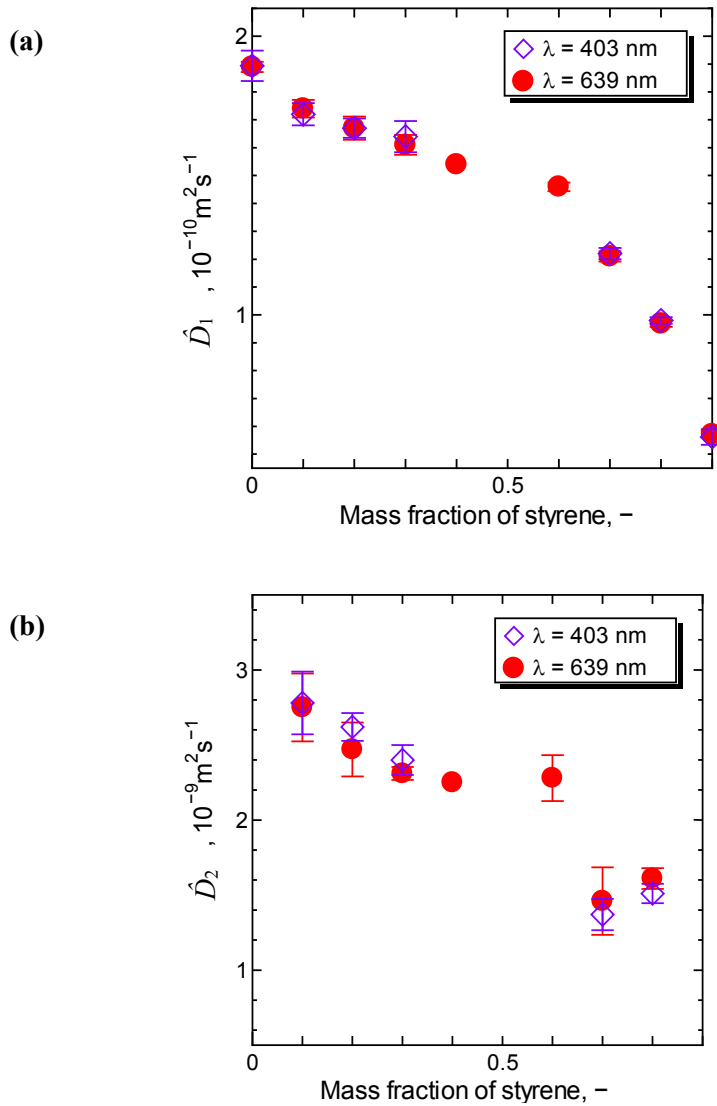
Figure 4.7: Diffusion eigenvalues $\hat{D}_i$ of CAB/styrene/2-butanone with $c_{CAB} = 0.10$ at $T = 298.2$ K. (a) $\hat{D}_1$ (mass diffusion coefficient D of CAB/Styrene and CAB/2-butanone are also plotted); (b) $\hat{D}_2$. Error bars are standard deviation of measurement.
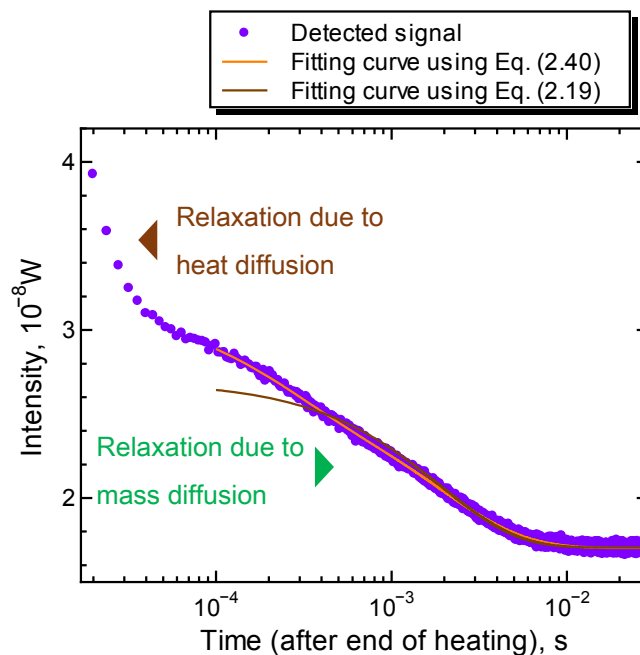
Figure 4.8: Relaxation signal after the end of heating for CAB/styrene/2-butanone with mass fractions of 0.10/0.30/0.60 at $T = 298.2$ K detected by the probing laser of $\lambda = 403$ nm. Relaxation mode due to heat diffusion can be separated from relaxation due to mass diffusion. Although fitting result using Eq. (2.19) for binary systems did not agree the mass diffusion signal, fitting result using Eq. (2.40) for ternary systems reproduced it.

4.3.2 Analysis of Soret effect signals in formation process

After the optical contrast factors and the diffusion eigenvalues were obtained, the Soret effect signals were analyzed based on Eqs. (2.41) and (2.42) for ternary polymer solutions. Since the diffusion eigenvalues were measured by the two probing lasers, average values of them were used in this analysis. The parameters $P'_{S,\lambda}$ and $P'_{T,\lambda}$ obtained from the Soret effect signals are listed in Table 4.8. The dependency of $P'_{S,\lambda}$ and $P'_{T,\lambda}$ on the composition is shown in Figures 4.9 and 4.10 respectively. As described in section 2.3.1, $P'_{S,\lambda}$ and $P'_{T,\lambda}$ are related to the asymptotic plateau, and the initial slope in the formation process of the concentration grating. The signs and trends of $P'_{S,\lambda}$ and $P'_{T,\lambda}$ agreed with the appearance of the Soret effect signals shown in Figure 4.5.

Table 4.8: $P'_{S,\lambda}$ and $P'_{T,\lambda}$ of CAB/styrene/2-butanone at $T = 298.2$ K.

c_{CAB}	$c_{styrene}$	$c_{2\text{-butanone}}$	$P'_{S,\lambda}$, 10^{-4}K^{-1}		$P'_{T,\lambda}$, 10^{-13}m^{2}s^{-1}K^{-1}	
			$\lambda = 403$ nm	$\lambda = 639$ nm	$\lambda = 403$ nm	$\lambda = 639$ nm
0.10	0.10	0.80	3.96 ± 0.07[a]	3.89 ± 0.07	1.32 ± 0.07	1.39 ± 0.07
0.10	0.20	0.70	2.86 ± 0.04	3.00 ± 0.02	1.35 ± 0.04	1.45 ± 0.04
0.10	0.30	0.60	2.03 ± 0.12	2.22 ± 0.20	1.45 ± 0.09	1.37 ± 0.03
0.10	0.40	0.50	0.76 ± 0.12	1.28 ± 0.14	0.839 ± 0.136	0.909 ± 0.107
0.10	0.60	0.30	-1.81 ± 0.06	-0.542 ± 0.019	-0.125 ± 0.030	0.123 ± 0.022
0.10	0.70	0.20	-2.90 ± 0.10	-1.66 ± 0.03	-0.574 ± 0.027	-0.302 ± 0.019
0.10	0.80	0.10	-4.70 ± 0.11	-2.85 ± 0.03	-0.778 ± 0.046	-0.477 ± 0.038

[a]Standard deviation of measurement.

Figure 4.9: $P'_{S,\lambda}$ of CAB/styrene/2-butanone with $c_{CAB} = 0.10$ at $T = 298.2$ K. Error bars are standard deviation of measurement.

Figure 4.10: $P'_{T,\lambda}$ of CAB/styrene/2-butanone with $c_{CAB} = 0.10$ at $T = 298.2$ K. Error bars are standard deviation of measurement.

4.3.3 Soret coefficient and thermodiffusion coefficient

With the values of experimentally obtained $P'_{S,\lambda}$ and $P'_{T,\lambda}$ and optical contrast factors, the Soret coefficient $S'_{T,i}$ and the thermodiffusion coefficient $D'_{T,i}$ of the ternary polymer solutions were determined by Eqs. (2.43) and (2.44), respectively. Tables 4.9 and 4.10 lists $S'_{T,i}$ and $D'_{T,i}$ obtained in this study, and the compositional dependency of $S'_{T,i}$ and $D'_{T,i}$ is shown in Figures 4.11 and 4.12, respectively.

It should be noted that obtained values of $S'_{T,i}$ and $D'_{T,i}$ for the ternary systems ($c_{styrene} = 0.10$–0.80 with $c_{CAB} = 0.10$) were comparable to that for the binary systems ($c_{styrene} = 0$ with $c_{CAB} = 0.10$ or $c_{styrene} = 0.90$ with $c_{CAB} = 0.10$), despite the working equations to determine $S'_{T,i}$ and $D'_{T,i}$ are quite different between binary and ternary systems. It was found that the Soret coefficient $S'_{T,i}$ of CAB is positive and $S'_{T,i}$ of styrene and 2-butanone is negative for the investigated conpositions, which means that CAB is transported to the colder region and the two solvents are transported to the warmer region under a temperature gradient.

Table 4.9: Soret coefficient $S'_{T,i}$ of CAB/styrene/2-butanone at $T = 298.2$ K.

			$S'_{T,i}$, $10^{-3}\mathrm{K}^{-1}$		
c_{CAB}	c_{styrene}	$c_{\mathrm{2\text{-}butanone}}$	CAB	styrene	2-butanone
0.10	0	0.90	5.20 ± 0.26[a]	–	-5.20 ± 0.26
0.10	0.10	0.80	3.88 ± 0.56	0.14 ± 0.28	-4.02 ± 0.28
0.10	0.20	0.70	4.82 ± 0.30	-1.02 ± 0.17	-3.80 ± 0.14
0.10	0.30	0.60	4.58 ± 1.09	-1.59 ± 0.59	-2.99 ± 0.51
0.10	0.40	0.50	4.35 ± 1.00	-2.12 ± 0.60	-2.24 ± 0.41
0.10	0.60	0.30	5.39 ± 0.23	-4.32 ± 0.17	-1.07 ± 0.06
0.10	0.70	0.20	5.11 ± 0.57	-4.61 ± 0.42	-0.51 ± 0.17
0.10	0.80	0.10	6.82 ± 0.97	-6.69 ± 0.68	-0.15 ± 0.29
0.10	0.90	0	11.8 ± 0.42	-11.8 ± 0.42	–

[a]Standard deviation of measurement.

Table 4.10: Thermodiffusion coefficient $D'_{T,i}$ of CAB/styrene/2-butanone at $T = 298.2$ K.

			$D'_{T,i}$, $10^{-12}\mathrm{m}^2\mathrm{s}^{-1}\mathrm{K}^{-1}$		
c_{CAB}	c_{styrene}	$c_{\mathrm{2\text{-}butanone}}$	CAB	styrene	2-butanone
0.10	0	0.90	0.97 ± 0.04[a]	–	-0.97 ± 0.04
0.10	0.10	0.80	1.87 ± 0.47	-0.23 ± 0.26	-1.64 ± 0.22
0.10	0.20	0.70	2.50 ± 0.29	-0.59 ± 0.15	-1.91 ± 0.14
0.10	0.30	0.60	1.56 ± 0.51	-0.18 ± 0.32	-1.37 ± 0.19
0.10	0.40	0.50	1.61 ± 0.93	-0.52 ± 0.57	-1.09 ± 0.36
0.10	0.60	0.30	1.35 ± 0.13	-0.92 ± 0.09	-0.43 ± 0.04
0.10	0.70	0.20	1.26 ± 0.12	-1.08 ± 0.08	-0.19 ± 0.04
0.10	0.80	0.10	1.13 ± 0.27	-1.11 ± 0.18	-0.02 ± 0.09
0.10	0.90	0	0.75 ± 0.03	-0.75 ± 0.03	–

[a]Standard deviation of measurement.
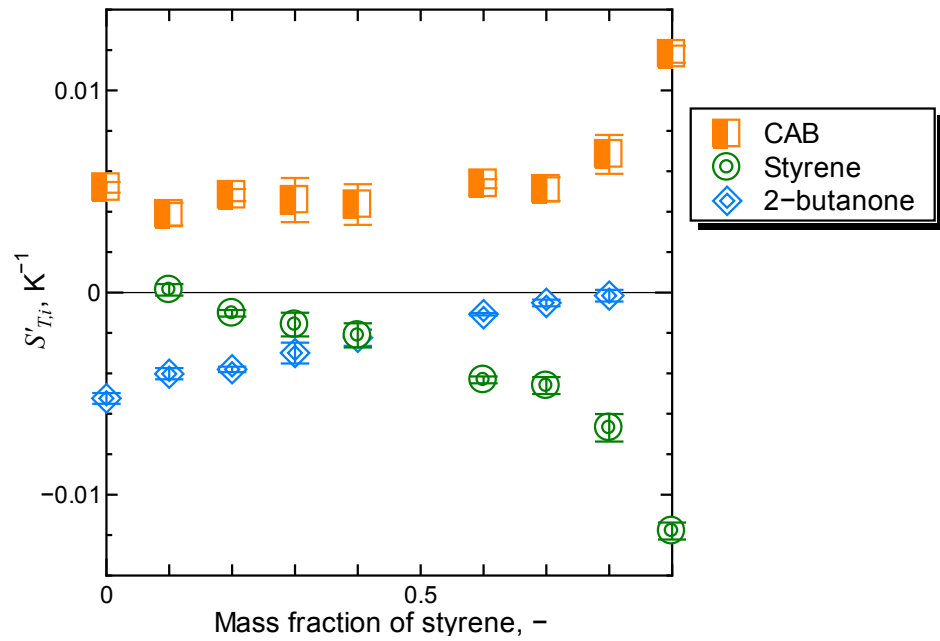
Figure 4.11: Soret coefficient $S'_{T,i}$ of CAB/styrene/2-butanone with $c_{CAB} = 0.10$ at $T = 298.2$ K. Error bars are standard deviation of measurement.

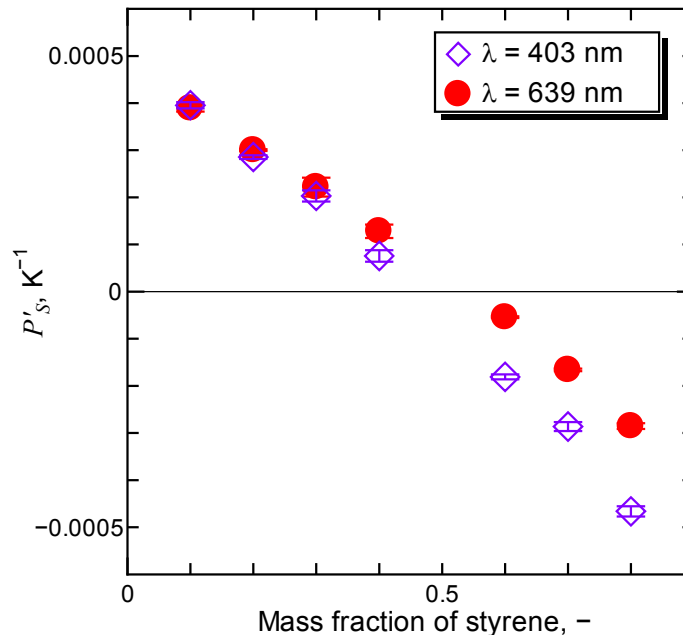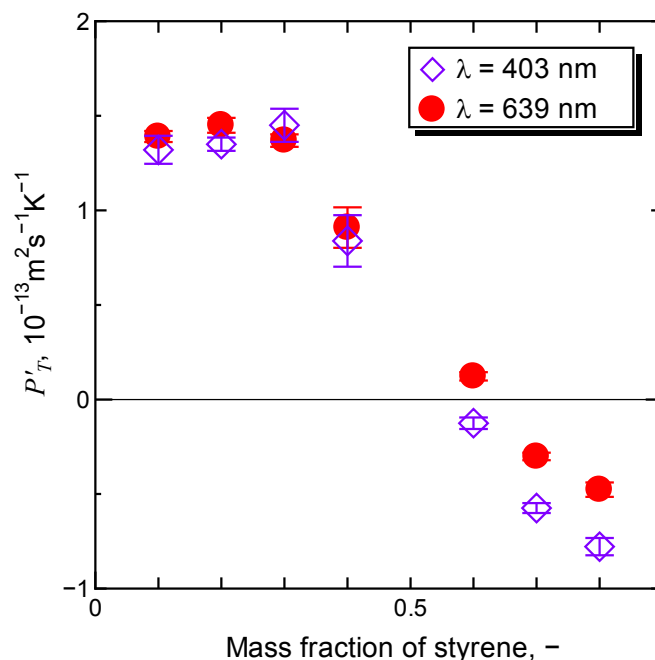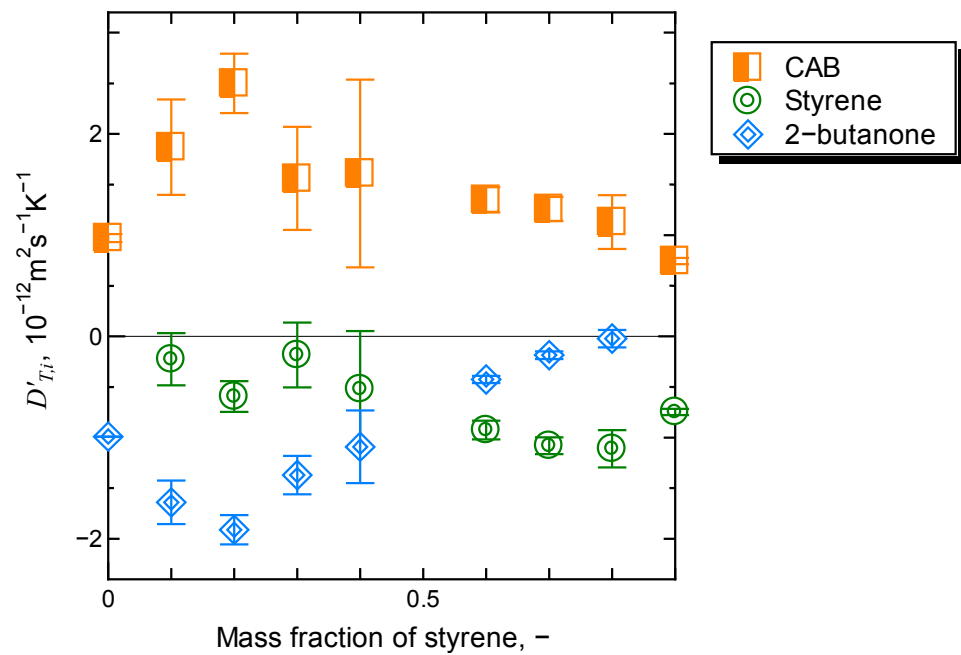**Figure 4.12:** Thermodiffusion coefficient $D'_{T,i}$ of CAB/styrene/2-butanone with $c_{CAB} = 0.10$ at $T = 298.2$ K. Error bars are standard deviation of measurement.

From this result, the behavior of detected signals shown in Figure 4.5 can be interpreted. From Eq. (2.23), the amplitude of the refractive index distribution is expressed as Eq. (4.6), when $c_1 = c_{styrene}$ and $c_2 = c_{2\text{-butanone}}$.

$$\Delta n_\lambda(t) = \left(\frac{\partial n_\lambda}{\partial c_{styrene}}\right)_{p,T,c_{2\text{-butanone}}} \Delta c_{styrene}(t) + \left(\frac{\partial n_\lambda}{\partial c_{2\text{-butanone}}}\right)_{p,T,c_{styrene}} \Delta c_{2\text{-butanone}}(t)$$
$$+ \left(\frac{\partial n_\lambda}{\partial T}\right) \Delta T(t) \tag{4.6}$$

Three terms on the right-hand side of Eq. (4.6) contribute to the signal intensity, which is proportional to the square of $\Delta n_\lambda(t)$. From the measurement of the refractive induces, the signs of the optical contrast factors were found: $\partial n_\lambda/\partial c_{styrene} > 0$, $\partial n_\lambda/\partial c_{2\text{-butanone}} < 0$, and $\partial n_\lambda/\partial T < 0$. On the other hand, signs of $\Delta c_{styrene}(t)$ and $\Delta c_{2\text{-butanone}}(t)$ are positive at the constructive interference regions of $\Delta T(t) > 0$, because $S'_{T,styrene}$ and $S'_{T,2\text{-butanone}}$ are negative. Therefore, the first, second and third term on the right-hand side of Eq. (4.6) are positive, negative, and negative, respectively. Note that the signs of two terms due to compositional changes are different. As shown in Figure 4.5, the intensity of the Soret effect signals increased when the ratio of $c_{2\text{-butanone}}$ was larger than that of $c_{styrene}$, because the contribution of the second term on the right-hand side of Eq. (4.6) was dominant. As the ratio of $c_{styrene}$ increased, the contribution the first term on the right-hand side of Eq. (4.6) increased, which lead to the decrease of the intensity of the Soret effect signals. When the mass fractions of 2-butanone and styrene were close, the intensity change in the Soret effect signals was small because two compositional contributions to the contrast of the refractive index grating cancel each other. This caused the intensity of the mass diffusion signals to be small and difficult to analyze (Figure 4.6(b)).

The result of the measurement showed that the Soret coefficient of CAB is positive, which means CAB is transported to colder region under a temperature gradient. On the other hand, the Soret coefficient was found to be negative and changed from almost zero to the values of binary mixture composed of CAB and the solvent, as $S'_{T,styrene}$ and $S'_{T,2\text{-butanone}}$ compensate each other. As it is known that the Soret coefficient of the heavier component is typically positive in a binary liquid mixtures [3], this trend for a ternary system was experimentally confirmed by the measurement in this study.

Unfortunately, a theoretical description which can be conveniently compared with the experimental data in this study was not found. An attempt was made to examine the relationship

of the Soret coefficient $S'_{T,i}$ and the solubility parameters. The Hildebrand solubility parameter δ_t is defined as the square root of the cohesive energy per unit volume [140]. By using Hansen parameters of δ_d, δ_p and δ_h, the Hildebrand parameter is expressed as [140]:

$$\delta_t^2 = \delta_d^2 + \delta_p^2 + \delta_h^2, \tag{4.7}$$

where δ_d is the energy from dispersion forces, δ_p is the energy from dipolar intermolecular force, and δ_h is the enegy from hydrogen bonds. When the difference of each solubility parameter between the components of fluid is small, the components are more likely to dissolve into each other. On the other hand, the tendency to separate is large, when the difference of solubility parameters is large. In this case, intuitively, it is likely that the components easily separate in a temperature gradient, which corresponds to a large Soret coefficient [3]. As an actual example, Kita *et al.* [141] confirmed the positive correlation between the Hildebrand parameter and the Soret coefficient in the experiments on binary solutions of Poly(N-isopropylacrylamide) and alcohols. Table 4.11 lists the solubility parameters of CAB, styrene, and 2-butanone. The Hildebrand parameter of two solvents, styrene and 2-butanone, are same, which might be related to the small dependency of the Soret coefficient in Figure 4.11 on the compositional ratio of styrene and 2-butanone. Further systematic experiments are required to discuss more about the tendency of the Soret coefficient.

Table 4.11: Solubility parameters of CAB, styrene, and 2-butanone.

	δ, $(MPa)^{1/2}$	δ_d, $(MPa)^{1/2}$	δ_p, $(MPa)^{1/2}$	δ_h, $(MPa)^{1/2}$
CAB 171[a] [142]	20.7	16.2	6.6	11.3
Styrene [140]	19.0	18.6	1.0	4.1
2-butanone [140]	19.0	16.0	9.0	5.1

[a]Acetyl content of 29.5 wt%, butyryl content 17.0 wt%, and hydroxyl content 1.5 wt%

In this chapter, the applicably and usefulness of the experimental apparatus developed in this study to the measurement of Soret coefficient in ternary polymer solutions was shown. Note that the Soret coefficient in ternary polymer solutions were obtained without the diffusion eigenvalues measured by other techniques, because two diffusion eigenvalues were separately obtained by the analysis of the mass diffusion signals. To the best of the author's knowledge, three Soret coefficients in ternary polymer solutions of practical interest in engineering have been presented for the first time. It is expected that this technique can contribute to understanding unrevealed mass transport phenomena in multicomponent systems.

5

Development of Infrared Soret forced Rayleigh scattering (IR-SFRS) apparatus

5.1   Concept of IR-SFRS using CO_2 laser

In the previous chapters, it was shown that measurement of Soret coefficient in binary and ternary organic mixtures can be performed by using the inert dye of quinizarin to convert the interference pattern of the heating laser with $\lambda = 532$ nm to the temperature grating. However, the situation is quite different in the measurement of aqueous systems, in which quinizarin is not be dissolved. Because absorption spectra due to dyes depend on pH, ionic strength, and other parameters, it is more difficult to find a suitable dye for aqueous systems [104].

Wiegand *et al.* [104] developed the thermal diffusion forced Rayleigh scattering setup for aqueous systems, employing a near infrared laser with the wavelength of $\lambda = 980$ nm. Due to the absorption of water, the use of a near-infrared laser as the heating laser enabled to create the temperature grating directly in a sample without dye. This technique, which is known as the infrared thermal diffusion forced Rayleigh scattering (IR-TDFRS), has been employed for the investigation of the Soret effect in various aqueous systems [111–120].

In addition, an experimental apparatus based on the holographic grating technique employing a CO_2 laser with the wavelength of $\lambda = 10.6$ μm as the heating laser was built in Nagasaka group [143]. This apparatus, called as the infrared Soret forced Rayleigh scattering (IR-SFRS), was developed with the aim to measure of the mass diffusion coefficient of aqueous methanol solutions in polymer electrolyte membranes (PEMs) for direct methanol fuel cells (DMFCs). However, it was difficult to obtain reasonable signals due to the scattered light generated at the polycrystalline diamond window in the sample cell [143].

Because IR-SFRS technique with a CO_2 laser basically works on the same principle as the SFRS technique using the green laser of $\lambda = 532$ nm described in the previous chapters, it has the potential to measure the Soret coefficient in aqueous systems. In addition, the use of a CO_2

laser could enable the measurement of Soret coefficient in heavy water, which cannot be performed by the IR-TDFRS setup with the heating laser of $\lambda = 980$ nm due to the absence of an absorption band [119]. Soret coefficient of protein in heavy water is important to examine solute-solvent interactions based on the concept of "hydration layer changes upon bio-macromolecular complex formation probed by thermodiffusion" proposed by Neither *et al.* [119].

This chapter will describe the development of IR-SFRS apparatus using a CO_2 laser with the aim to measure the Soret coefficient in binary systems, as the first step to examine more complexed systems.

5.2　Design of IR-SFRS apparatus

5.2.1 Sample cell

A. Selection of window materials

In an IR-SFRS experiment, a quartz cell cannot be used as a sample cell, because the IR beam of the CO_2 laser is absorbed by quartz. Therefore, development of a sample cell suitable for IR-SFRS experiments was needed. Two optical windows were required to interpose aqueous solution samples between them in a sample cell. The window for the incidence side must transmit both the heating laser and the probing laser.

In the previous study in Nagasaka group [143], a polycrystalline diamond window was employed for the incidence side, but found it difficult to obtain reasonable signals due to the scattered light of probing beam of $\lambda = 661$ nm generated at the window, as the scattered light coherent with the first order diffracted beam affected the signals.

A ZnSe window transmits both the IR heating laser and the red probing laser, but it reacts under an acidic environment. In this study, a single crystal diamond window was introduced as a window for the incidence side to reduce the effect of the scattered light. It was experimentally confirmed that the intensity of the scattered light with the single crystal diamond window was about 1/150 that of the polycrystalline diamond window, and was similar to a quartz glass window. In addition, a single crystal diamond window is stable under an acidic environment.

Although a glass window, which absorbs IR beams, is not suitable for the incidence side, it can be used as the exit side window. Figure 5.1 compares the appearance of the single crystal

diamond window, the polycrystalline diamond window, and the glass window.

B. Configuration of sample cell

Figure 5.2 shows the new sample cell designed by Daichi Tokuda (collaborator) to introduce the single crystal diamond window (145-500-0390, Element Six), which is 4.5 × 4.5 mm in size, and 0.5-mm thick. The sample is interposed between a glass window and a single crystal diamond window, which was held in a Cu plate with a square hole. Silicone gaskets are used for sealing. This sample cell has a screw cap structure that is easy to assemble. The exit side parts such as the glass window had two holes in addition to a center hole for the optical path, so that the cell could be filled with the sample liquid after assembly. The sample cell is set on a copper mount that contained thermostatically controlled circulating water.
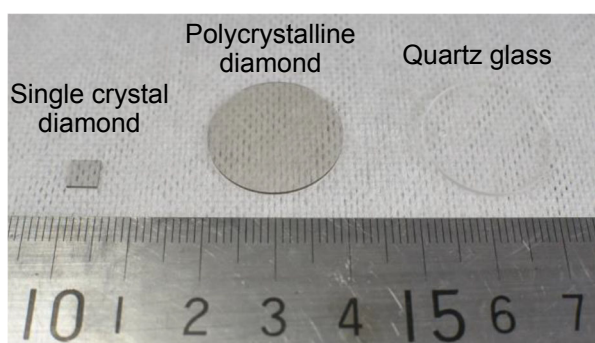
Figure. 5.1: Appearance of optical windows.
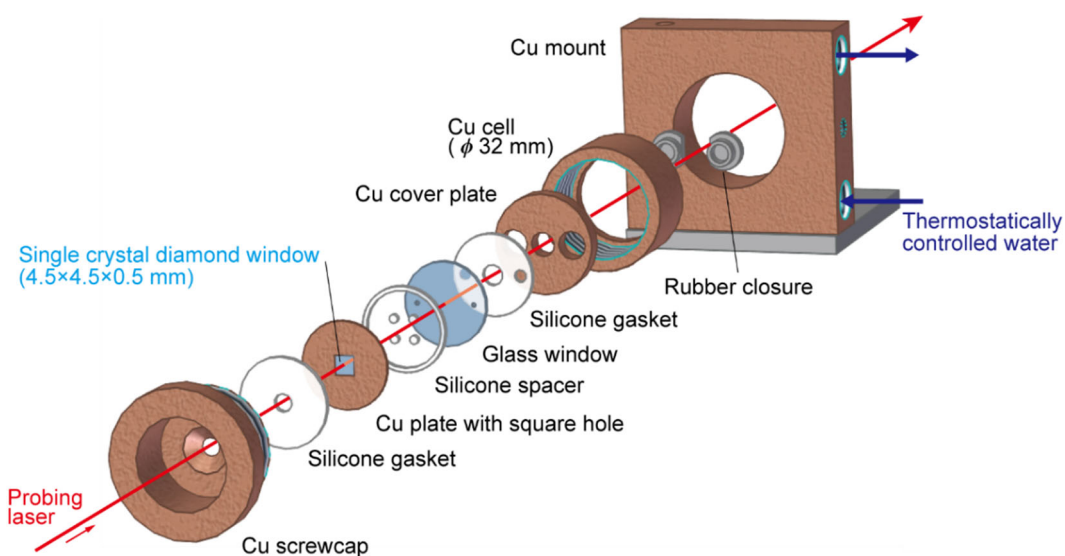
Figure. 5.2: Sample cell for IR-SFRS, in which a single crystal diamond window was employed as the incident side window (designed by collaborator Daichi Tokuda).
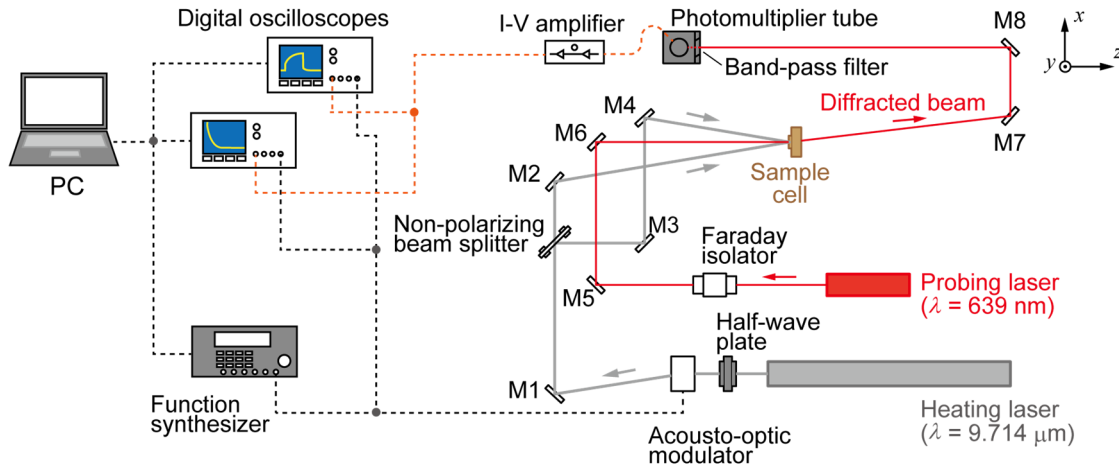
Figure. 5.3: Experimental apparatus of the infrared Soret forced Rayleigh scattering (IR-SFRS) technique.

5.2.2 Optical system

Figure 5.3 is a schematic of the experimental apparatus of the IR-SFRS technique designed and built for the homodyne (direct) detection scheme. As the heating laser, a variable-wavelength CO_2 laser (L20G, Access Laser Company) which emits beam of the wavelength of 9.183–9.733 μm and 10.125–10.811 μm was employed. This laser was introduced to adjust the emitting wavelength to use the absorption range due to the CO stretching of methanol, for the measurement of mass diffusion coefficient of aqueous methanol solutions in PEMs. In this study, the heating wavelength of $\lambda = 9.714$ μm was selected after the consideration of the emitting power and the stability.

A half-wavelength plate (#85-123; Edmund Optics) was employed to adjust the polarization to the acousto-optic modulator (1209-7-1064M, anti-reflective coating for 9.7 μm; Isomet), which generated the diffracted beam while the modulation voltage was applied to the driver (RFA241; Isomet). The diffracted beam from the acousto-optic modulator was split into two beams by a non-polarizing beamsplitter (PIB-5005Z; Lambda Research Optics). The two beams crossed in the sample.

The two heating laser beams entered symmetrically to the normal direction of the sample surface. The incident angle of the heating laser θ_h was adjusted to satisfy the designed interference fringe spacing (typically about 30 μm) based on Eq. (2.48).

A Faraday isolator (IO-3-633-LP/M; Thorlabs) was used to prevent backreflection into the probing laser (OBIS637-140LX-HTK) with the wavelength of $\lambda = 639$ nm. The probing laser

entered the sample vertically, because the Raman-Nath condition for diffraction [144] was adopted in the IR-SFRS experiment due to the short absorption length (micrometer order) of the infrared heating laser; meanwhile, the Bragg condition was adopted in the SFRS apparatus using visible light lasers as described in Chapter 2. The first order diffracted beam was aligned so as to enter the photomultiplier tube (R9110; Hamamatsu Photonics), which was installed in the housing with a bandpass filter (FF02-632/22-25; Semrock).

A variable gain current–voltage amplifier (DLPCA-200; Femto) amplified the output current from the photomultiplier tube. The output signal was then observed in real time using digital oscilloscopes (DPO3014 and TDS3032B; Tektronix). Data analysis and control of the instruments, including the digital oscilloscopes, were carried out using LabVIEW software on a PC.

5.3 Measurement of fringe spacing

The interference pattern of the IR heating laser cannot be observed by a beam profiler for visible wavelengths. To determine fringe spacing Λ, the diffraction angle of the $\pm$1st mode θ_1 was evaluated. The relationship between Λ and θ_1 can be described as:

$$\Lambda = \frac{\lambda_{\mathrm{p}}}{\sin \theta_1},$$ (5.1)

where λ_{p} is the wavelength of the probing laser ($\lambda_{\mathrm{p}} = 639$ nm).

After the mirrors M1–M4 of the heating laser system and M5 and M6 of the probing laser system were aligned as shown in Figure 5.3, a 1-mm thick acrylic plate was mounted at the sample position. The interference grating was then written on the acrylic plate by the heating laser so that stationary emitted diffracted beams were observed. The distance between the 1st order and −1st order diffracted beams at each position from the acrylic plate was measured. The diffraction angle of the $\pm$1st mode θ_1 is described as:

$$\theta_1 = \tan^{-1}\left(\frac{l/2}{L}\right),$$ (5.2)

where l is the distance between the $\pm$1st order diffracted beams, and L is the distance from the

5. Development of Infrared Soret forced Rayleigh scattering (IR-SFRS) apparatus

acrylic plate (Figure 5.4).

To determine the position of the diffracted beams, a probing needle (mechanical pencil lead with a diameter of 0.2 mm) mounted on a manual linear translation stage was used. The position of the needle was adjusted so that its shadow on the screen was at the center of the diffracted beams. Figure 5.5 shows a typical measurement result of $l/2$ vs. L. From Eq. (5.2), the diffraction angle θ_1 was determined by the slope of the fitting line in Figure 5.5. In this case, fringe spacing Λ was determined to be 29.5 μm from Eq. (5.1), with the standard uncertainty evaluated to be within 1.0%.
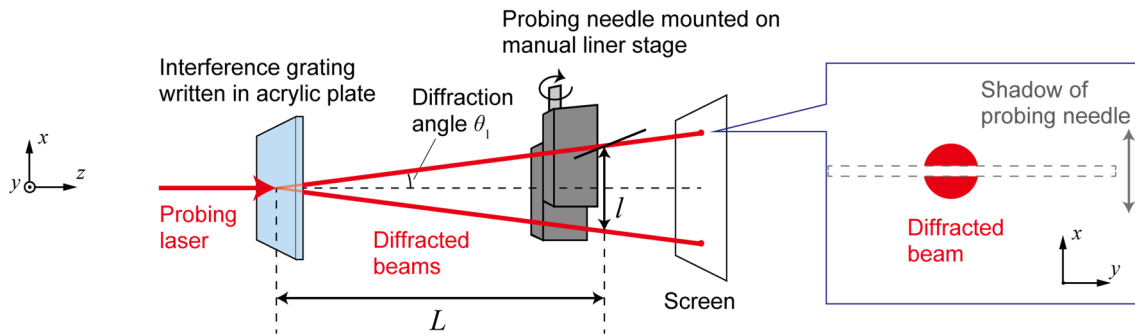
Figure. 5.4: Measurement method to determine the diffraction angle of ±1st mode θ_1. After writing an interference grating in an acrylic plate by the heating laser, the distance between the ±1st order diffracted beams l is measured.
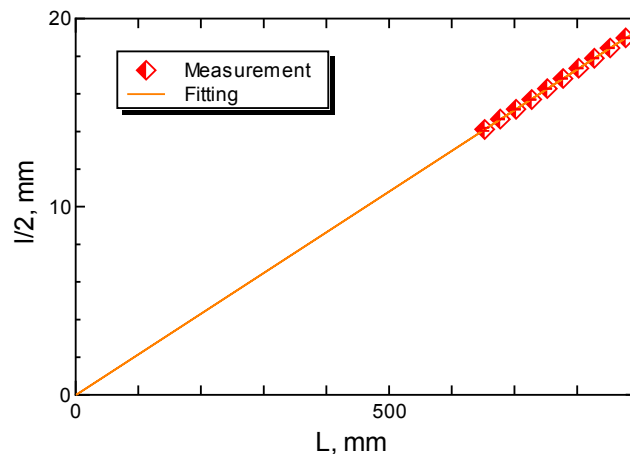
Figure. 5.5: A typical relationship of a half of the distance between the ±1st order diffracted beams $l/2$ and the distance between the acrylic plate and the probing needle L, which were measured to determine the fringe spacing Λ.

5.4 Measurement of aqueous ethanol solution to confirm the validity

Although there are no standard values or benchmark values of Soret coefficient in aqueous systems, some experimental data to be compared with are available for aqueous ethanol solutions [39,104]. Therefore, measurement of Soret coefficient of a binary aqueous ethanol solution was carried out to check the validity of the IR-SFRS apparatus developed in this study. The aqueous ethanol solution was composed of 10 wt% of ethanol (>99.5%, Wako) and 90 wt% of purified water (Wako).

Figure 5.6 shows the detected signal. The Soret effect was observed after the formation of the temperature gratings. Because the diffraction efficiency is proportional to the square of the amplitude of the refractive index distribution $\Delta n(t)$ in the case of Raman-Nath diffraction [144], as in the case with the Bragg diffraction, detected signals can be analyzed using the working equations described in Chapter 2. Mass diffusion signals were analyzed based on Eq. (2.19) and the Soret effect signals were analyzed based on Eqs. (2.21) and (2.22), with the optical contrast factors measured by Königer et al. [39]: $\partial n_{635}/\partial c = 0.0700$ and $\partial n_{635}/\partial T = -1.274 \times 10^{-4}$ [K^{-1}]. Fitting curves for both the mass diffusion signals and the Soret effect signals agreed with the detected signals with the deviation within 2%, as shown in Figures 5.7 and 5.8.
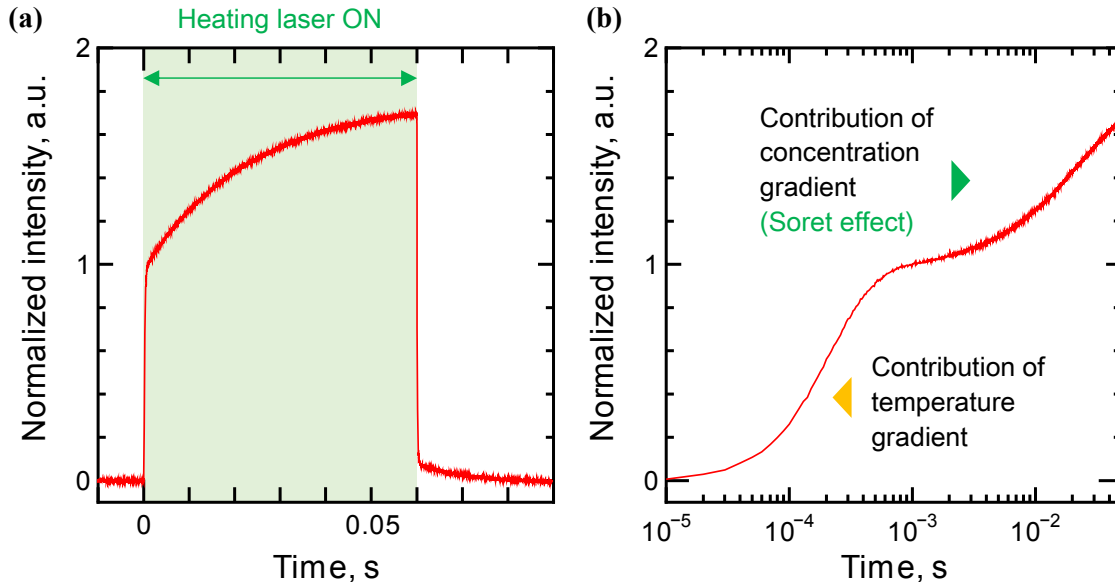
Figure. 5.6: Detected signal of aqueous ethanol solution $c_{ethanol} = 0.10$ at $T = 298.2$ K. (a) Signals in formation and relaxation process; (b) Signals in formation process versus logarithmic time to clarify two modes.
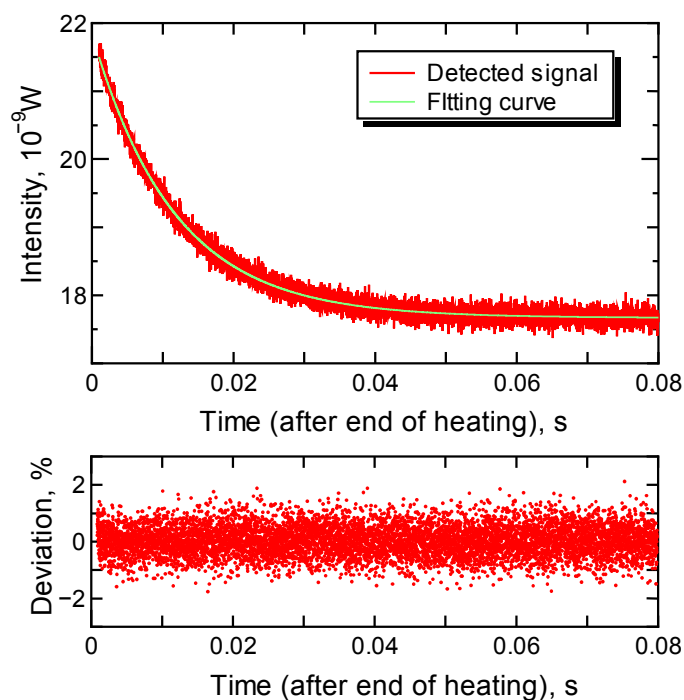
Figure. 5.7: 16 times averaged mass diffusion signal and fitting curve of aqueous ethanol solution with $c_{ethanol} = 0.10$ at $T = 298.2$ K.
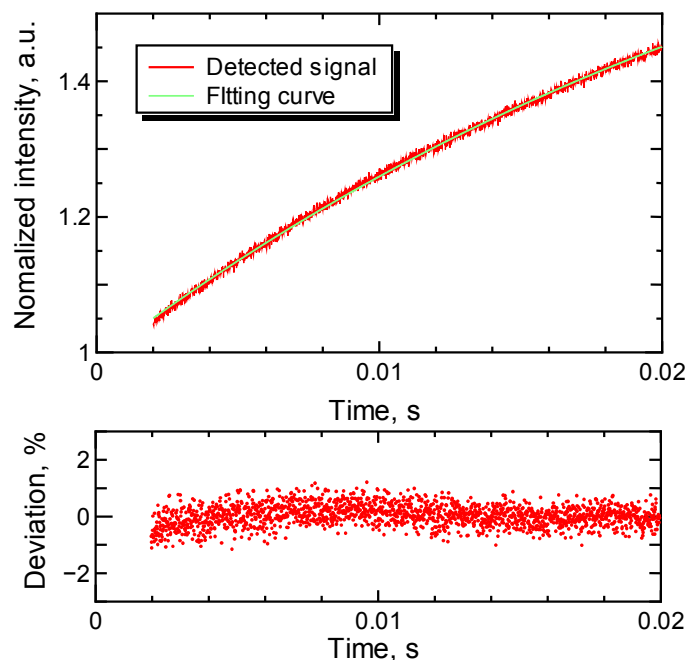
Figure. 5.8: 16 times averaged Soret effect signal and fitting curve of aqueous ethanol solution with $c_{ethanol} = 0.10$ at $T = 298.2$ K.

Table 5.1: Experimental result and standard uncertainties of mass diffusion coefficient D, Soret coefficient S_T, and thermodiffusion coefficient D_T of binary aqueous ethanol solution ($c_{\text{ethanol}} = 0.10$) at $T = 298.2$ K.

	D, 10^{-10} m^{2}s^{-1}	$u(D)$[a], 10^{-10} m^{2}s^{-1}	S_T, 10^{-3} K^{-1}	$u(S_T)$[a], 10^{-3} K^{-1}	D_T, 10^{-12} m^{2}s^{-1}K^{-1}	$u(D_T)$[a], 10^{-12} m^{2}s^{-1}K^{-1}
This work	9.68	0.25 (2.6%)	6.86	0.14 (2.0%)	6.61	0.22 (3.3%)
Königer *et al.* [39]	9.60	–	6.75	–	6.48	–
Wiegand *et al.* [104]	9.48	–	6.32	0.30 (4.7%)	5.99	–

[a]$u(D)$, $u(S_T)$, and $u(D_T)$ are the standard uncertainties of the mass diffusion coefficient, the Soret coefficient, and the thermodiffusion coefficient in the measurement.

In Table 5.1, the mass diffusion coefficient D, the Soret coefficient S_T, and the thermodiffusion coefficient D_T obtained in this study are compared to the experimental data available on literature. They agreed well within the range of the uncertainties. Therefore, the validity of the IR-SFRS apparatus using a single crystal diamond window in the newly designed sample cell was confirmed for the measurement of Soret coefficient in binary aqueous solutions.

5.5 Potential of IR-SFRS apparatus

Although experiments were performed only on a binary aqueous ethanol solution by the IR-SFRS apparatus developed in this study, this technique has a potential to measure various aqueous solutions not only for binary systems, but also for ternary systems. Two wavelength detection scheme can be integrated to the IR-SFRS apparatus by adding another probing laser. Because addition of dye is not required in experiments by the IR-SFRS technique, the probing wavelength is not limited by the absorption spectrum of the dye. Therefore, IR-SFRS apparatus employing more than two probing wavelengths can be designed, which could reduce the uncertainties of the measurements.

The IR-SFRS technique also has a potential to investigate the Soret effect in membranes,

by utilizing its unique principle that both inducement and detection of the Soret effect and mass diffusion can be performed optically. For example, the Soret effect of aqueous alcohol solutions in polymer electrolyte membranes (PEMs), which is known as the thermo-osmosis [145], could be investigated.

6

Conclusion

As discussed in the introduction, mass transport phenomena including the Soret effect, which is driven by the temperature gradient, play significant roles in many natural systems and engineering processes. Since there is as yet no comprehensive microscopic description of the Soret effect in multicomponent liquid mixtures, gaining knowledge by experimental approaches is important. Compared to binary systems, the Soret effect in multicomponent systems composed of more than two component is poorly understood due to the complexity.

This study dealt with the development of the optical holographic grating technique which is called as the Soret forced Rayleigh scattering (SFRS). To measure the Soret coefficient in binary and ternary systems by the SFRS technique employing homodyne detection scheme, working equations were derived. It involved the application of the two-wavelength detection technique which utilizes the dependence of the refractive index on the wavelength. An experimental apparatus which enabled the simultaneous detection by two probing lasers was designed and built. As the wavelengths of the detection lasers, $\lambda = 403$ nm and $\lambda = 639$ nm were selected, whereas the heating laser of $\lambda = 532$ nm was employed to induce the Soret effect in a sample. By controlling the irradiation time of the probing lasers, the effect of absorption of the probing laser to the sample with dye (quinizarin), which is added to convert the interference pattern of the heating laser of $\lambda = 532$ nm to the temperature grating, can be reduced.

The result of the measurement of the Soret coefficient and the mass diffusion coefficient in binary benchmark mixtures composed of 1,2,3,4-tetrahydronaphthalene (THN), isobutylbenzene (IBB), and n-dodecane (nC12) showed that the simultaneous two-wavelength observation of the Soret effect and the mass diffusion were adequately performed. To evaluate the performance in the measurement of ternary systems, experiments were carried out on the ternary benchmark mixtures of THN/IBB/nC12 with the mass fractions of 0.800/0.100/0.100 at a temperature of 298.2 K. The Soret coefficient and thermodiffusion coefficient agreed with the ternary benchmark values within the range of the standard uncertainties (23% for the Soret

coefficient of THN and 30% for the thermodiffusion coefficient of THN).

After the validation, this technique was applied to the measurement of ternary polymer solutions composed of cellulose acetate butyrate (CAB), styrene, and 2-butanone at a temperature of 298.2 K. Before the SFRS experiments, the optical contrast factors were determined by the measurement of the refractive induces using a multi-wavelength Abbe refractometer. It was found that the condition numbers (1-norm) for CAB/styrene/2-butanone were lower than 21 and this system is not ill-conditioned. By analyzing the relaxation signals due to the mass diffusion, two diffusion eigenvalues were separately obtained. It was found that the Soret coefficients of CAB were positive and that of solvents were negative at examined compositions in which the mass fractions of CAB is 0.1. To the best of the author's knowledge, three Soret coefficients in ternary polymer solutions of practical interest in engineering were presented for the first time.

Another experimental apparatus employing a CO_2 laser as the heating laser was developed with the aim to measure the Soret coefficient in aqueous systems. This technique, called as the infrared Soret forced Rayleigh scattering (IR-SFRS), enables measurements without addition of dye to samples. As the incident side window in a newly designed sample cell, a single crystal diamond window, which transmits both the heating laser with the wavelength of $\lambda = 9.714$ μm and the probing laser with the wavelength of $\lambda = 639$ nm, was selected. The validity of the instrument for binary systems was confirmed by the measurement of the Soret coefficient of a binary aqueous ethanol solution with the mass fraction of ethanol 0.1 at a temperature 298.2 K.

In this thesis, two new experimental apparatus based on the SFRS technique were presented. The two-wavelength detection technique was successfully integrated to the first one, which enabled the measurement of the Soret coefficient in ternary systems by the SFRS technique. The development of another one with an infrared laser was started for the measurement of aqueous systems and validated for binary systems, as a first step. This IR-SFRS apparatus can be extended to measurement of ternary systems, by applying the two-wavelength detection scheme. Although the experimental techniques of the Soret coefficient in ternary systems were limited to three (thermogravitational column, optical beam deflection, optical digital interferometry) and they have both their advantages and drawbacks, the development of SFRS technique described in this thesis added another option to measure the Soret coefficient in multicomponent systems. By utilizing its unique principle, it is expected that the SFRS technique will be used as a helpful tool to examine Soret effect in complexed systems which were not accessed by other techniques, for

example, concentrated ternary polymer solutions with high viscosity or samples close to the critical point. Obtaining experimental data in wide temperature and concentration range by the SFRS technique should promote applications of the knowledge on the Soret effect to optimization of engineering processes such as solution casting for polymer films. In addition, systematic experiments by the SFRS technique will provide data to be compared with theoretical models. It would be interesting to apply the SFRS technique to the measurement of ternary solutions including polystyrene, which has been relativity well studied for binary systems.

References

[1] E. L. Cussler, *Diffusion: Mass Transfer in Fluid Systems, Second Edition* (Cambridge University Press, Cambridge, 1997).

[2] W. Köhler, K. I. Morozov, The Soret Effect in Liquid Mixtures – A Review, *J. Non-Equilib. Thermodyn.*, **41**, 151–197, (2016).

[3] S. Wiegand, Thermal diffusion in liquid mixtures and polymer solutions, *J. Phys. Condens. Mat.*, **16**, R357–379, (2004).

[4] J. K. Platten, The Soret effect: A review of recent experimental results, *J. Appl. Mech.*, **73**, 5–15, (2006).

[5] S. R. de Groot, P. Mazur, *Non-Equilibrium Thermodynamics* (Dover, New York, 1984).

[6] C. Ludwig, Diffusion zwischen ungleich erwwärmten orten gleich zusammengestzter lösungen, *Sitz. Ber. Akad. Wiss.*, **20**, 539, (1856).

[7] A. Fick, Über diffusion, *Ann. Phys.*, **170**, 59–86, (1855).

[8] C. Soret, Sur l'état d'équilibre que prend au point de vue de sa concentration une dissolution saline primitivement homogéne dont deux parties sont portées a des températures différentes, *Arch. Sci. Phys. Nat. Genéve*, **2**, 48–61, (1879).

[9] C. Soret, Influence de la température sur la distribution des sels dans leurs solutions, *C.R. Acad. Sci. (Paris)*, **91**, 289–291, (1880).

[10] C. Soret, Sur l'état d'équilibre que prend au point de vue de sa concentration une dissolution saline primitivement homohéne dont deux parties sont portées a des temperatures différentes, *Ann. Chim. Phys.* **22**, 293–297, (1881).

[11] J. K. Platten, P. Costesèque, Charles Soret. A short biography, *Eur. Phys. J. E*, **15**, 235–239, (2004).

[12] K. Clusius, G. Dickel, Neues Verfahren zur Gasentmischung und Isotopentrennung, *Naturwissenschaften*, **26**, 546–552, (1938).

[13] K. Clusius, G. Dickel, Das Trennrohrverfahren bei Flüssigkeiten, *Naturwissenschaften*, **27**, 148–149, (1939).

[14] G Galliero, H. Bataller, J. P. Bazile, J. Diaz, F. Croccolo, H. Hoang, R. Vermorel, P. A. Artola, B. Rousseau, V. Vesovic, M. M. Bou-Ali, J. M. Ortiz de Zárate, S. Xu, K. Zhang, F. Montel,

99

A. Verga, O. Minster, Thermodiffusion in multicomponent *n*-alkane mixtures, *NPJ Microgravity*, **3,** 20, (2017).

[15] F. Montel, J. Bickert, A. Lagisquet, G. Galliéro, Initial state of petroleum reservoirs: A comprehensive approach, *J. Petrol. Sci. Eng.*, **58**, 391–402, (2007).

[16] M. Touzet, G. Galliéro, V. Lazzeri, M. Z. Saghir, F. Montel, J-C. Legros, Thermodiffusion: From microgravity experiments to the initial state of petroleum reservoirs, *C. R. Mecanique*, **339**, 318–323, (2011).

[17] F. M. Richter, E. B. Watson, R. A. Mendybaev, F-Z. Teng, P. E. Janney. Magnesium isotope fractionation in silicate melts by chemical and thermal diffusion, *Geochim. Cosmochim. Ac.*, **72**, 206–220, (2008).

[18] F. M. Richer, N. Dauphas, F-Z. Teng, Non-traditional fractionation of non-traditional isotopes: Evaporation, chemical diffusion and Soret diffusion, *Chem. Geol.*, **258**, 92–103, (2009).

[19] D. J. Lacks, G. Goel, C. J. Bopp IV, J. A. Van Orman, C. E. Lesher, C. C. Lundstrom, Isotope fractionation by thermal diffusion in silicate melts, *Phys. Rev. Lett.*, **108**, 065901, (2009).

[20] F. M. Richter, E. B. Watson, M. Chaussidon, R. Mendybaev, J. N. Christensen, L. Qiu, Isotope fractionation of Li and K in silicate liquids by Soret diffusion, *Geochim. Cosmochim. Ac.*, **138**, 136–145 (2014).

[21] G. Dominguez, G. Wilkins, M. H. Theimens, The Soret effect and isotopic fractionation inhigh-temperature silicate melts, *Nature*, **473**, 70–73, (2011).

[22] S. S. Es-haghi, M. Cakmak, Mass and heat diffusion in ternary polymer solutions: A classical irreversible thermodynamics approach, *Polymer*, **97**, 147–157, (2016).

[23] S. S. Es-haghi, M. Cakmak, in *Roll-to-Roll Manufacturing: Process Elements and Recent Advances*, edited by J. Greener, G. Pearson, M. Cakmak, (Wiley, Hoboken, US, 2018), pp. 65–110.

[24] P. Baaske, F. M. Weinert, S. Duhr, K. H. Lemke, M. J. Russell, D. P. Braun, *Proc. Natl. Acad. Sci.*, **104**, 9346–9351, (2007).

[25] I. Budin, R. J. Bruckner, J. W. Szostak, Formation of protocell-like vesicles in a thermal diffusion column, *J. Am. Chem. Soc.*, **131**, 9628–9629, (2009).

[26] C. B. Mast, D. Braun, Thermal trap for DNA replication, *Phys. Rev. Lett.*, **104**, 188102, (2010).

[27] C. B. Mast, S. Schink, U. Gerland, D. Braun, Escalation of polymerization in a thermal gradient, *Proc. Natl. Acad. Sci.*, **110**, 8030–8035, (2013).

[28] D. Niether, D. Afanasenkau, J. K. G. Dhont, S. Wiegand, Accumulation of formamide in hydrothermal pores to form prebiotic nucleobases, *Proc. Natl. Acad. Sci.*, **113**, 4272–4277, (2016).

[29] S. Chapman, T. G. Cowling, *The mathematical theory of non-uniform gases : an account of the kinetic theory of viscosity, thermal conduction, and diffusion in gases* (Cambridge University Press, Cambridge, 1939).

[30] J. O. Hirschfelder, C. F. Curtiss, R. B. Bird, *Molecular Theory of Gases and Liquids* (Wiley, New York, 1954).

[31] G. Maitland, M. Rigby, E. Smith, W. Wakeham, *Intermolecular Forces: Their Origin and Determination* (Oxfrod University Press, Oxford, 1981).

[32] J. K. Platten, M. M. Bou-Ali, P. Costesèque, J. F. Dutrieux, W. Köhler, C. Leppla, S. Wiegand, G. Wittko. Benchmark values for the Soret, thermal diffusion and diffusion coefficients of three binary organic liquid mixtures, *Philos. Mag.*, **83**, 1965–1971, (2003).

[33] G. Wittko, W. Köhler, Precise determination of the Soret, thermal diffusion and mass diffusion coefficients of binary mixtures of dodecane, isobutylbenzene and 1,2,3,4-tetrahydronaphthalene by a holographic grating technique, *Philos. Mag.*, **83**, 1973–1987, (2003).

[34] C. Leppla, S. Wiegrand, Investigation of the Soret effect in binary liquid mixtures by thermal-diffusion-forced Rayleigh scattering (contribution to the benchmark test) , *Philos. Mag.*, **83**, 1989–1999, (2003).

[35] J. K. Platten, M. M. Bou-Ali, J. F. Dutrieux, Precise determination of the Soret, thermodiffusion and isothermal diffusion coefficients of binary mixtures of dodecane, isobutylbenzene and 1,2,3,4-tetrahydronaphthalene (contribution of the University of Mons to the benchmark test) , *Philos. Mag.*, **83**, 2001–2010, (2003).

[36] M. M. Bou-Ali, J. J. Valencia, Determination of the thermodiffusion coefficient in three binary organic liquid mixtures by the thermogravitational method (contribution of the Universidad del País Vasco, Bilbao, to the benchmark test) , *Philos. Mag.*, **83**, 2011–2015, (2003).

[37] P. Costesèque, J-C. Loubet, Measuring the Soret coefficient of binary hydrocarbon mixtures

in packed thermogravitational columns (contribution to Toulouse University to the benchmark test), *Philos. Mag.*, **83**, 2017–2022, (2003).

[38] A. Mialdun, V. Shevtsova, Measurement of the Soret and diffusion coefficients for benchmark binary mixtures by means of digital interferometry, *J. Chem. Phys.*, **134**, 044524, (2011).

[39] A. Königer, B. Meier, W. Köhler, Measurement of the Soret, diffusion, and thermal diffusion coefficients of three binary organic benchmark mixtures and of ethanol/water mixtures using a beam deflection technique, *Philos. Mag.*, **89**, 907–923, (2009).

[40] P. Naumann, A. Martin, H. Kriegs, M. Larrañaga, M. M. Bou-Ali, S. Wiegand, Development of a thermogravitational microcolumn with an interferometric contactless detection system, *J. Phys. Chem. B*, **116**, 13889–13897, (2012).

[41] E. Lapeira, A. Mialdun, V. Yasnou, P. Aristimuño, V. Shevtsova, M. M. Bou-Ali, Digital Interferometry Applied to Thermogravitational Technique, *Microgravity Sci. Technol.*, **30**, 635–641, (2018).

[42] F. Croccolo, H. Bataller, and F. Scheffold, A light scattering study of non equilibrium fluctuations in liquid mixtures to measure the Soret and mass diffusion coefficient, *J. Chem. Phys.*, **137**, 234202, (2012).

[43] P. Kolodner, H. Williams, C. Moe, Optical measurement of the Soret coefficient of ethanol/water solutions, *J. Chem. Phys.*, **88**, 6512–6524, (1988).

[44] J. C. Giddings, K. D. Caldwell, M. N. Myers, Thermal diffusion of polystyrene in eight solvents by an improved thermal field-flow fractionation methodology, *Macromolecules*, **9**, 106–112, (1976).

[45] M. E. Schimpf, J. C. Giddings, Characterization of thermal diffusion in polymer solutions by thermal field-flow fractionation: Dependence of polymer and solvent parameters, *J. Polym. Sci., Part B: Polym. Phys.*, **27**, 1317–1332, (1989).

[46] M. E. Schimpf, J. C. Giddings, Characterization of thermal diffusion in polymer solutions by thermal field-flow fractionation: effects of molecular weight and branching, *Macromolecules*, **20**, 1561–1563, (1987).

[47] C. Debuschewitz, W. Köhler, Molecular origin of thermal diffusion in benzene+cyclohexane mixtures, *Phys. Rev. Lett.*, **87**, 055901, (2001).

[48] G. Wittko, W. Köhler, Universal isotope effect in thermal diffusion of mixtures containing

cyclohexane and cyclohexane-d12, *J. Chem. Phys.*, **123**, 014506, (2005).

[49] G. Wittko, W. Köhler, Influence of isotopic substitution on the diffusion and thermal diffusion coefficient of binary liquids, *Eur. Phys. J. E*, **21**, 283–291, (2006).

[50] G. Wittko, W. Köhler, On the temperature dependence of thermodiffusion of liquid mixtures, *Europhys. Lett.*, **78**, 46007, (2007).

[51] S. Hartmann, W. Köhler, K. I. Morozov, The isotope Soret effect in liquids: a quantum effect at room temperatures, *Soft Matter*, **8**, 1355–1360, (2012).

[52] S. Hartmann, G. Wittko, W. Köhler, K. I. Morozov, K. Albers, G. Sadowski, Thermophobicity of liquids: heats of transport in mixtures as pure component properties, *Phys. Rev. Lett.*, **109**, 065901, (2012).

[53] S. Hartmann, G. Wittko, F. Schock, W. Groß, F. Lindner, W. Köhler, K. I. Morozov, Thermophobicity of liquids: heats of transport in mixtures as pure component properties - the case of arbitrary concentration, *J. Chem. Phys.*, **141**, 134503, (2014).

[54] E. L. Cussler, *Multicomponent Diffusion 1st Edition*, (Elsevier, Amsterdam - Oxford - New York, 1976).

[55] A. Leahy-Dios, M. M. Bou-Ali, J. K. Platten, A. Firoozabadi, Measurements of molecular and thermal diffusion coefficients in ternary mixtures. *J. Chem. Phys.*, **122**, 234502, (2005).

[56] M. M. Bou-Ali, J. K. Platten, Metrology of the thermodiffusion coefficients in a ternary system, *J. Non-Equilib. Thermodyn.*, **30**, 385–399, (2005).

[57] P. Blanco, M. M. Bou-Ali, J. K. Platten, D. A. de Mezquia, J. A. Madariaga, C. Santamaría, Thermodiffusion coefficients of binary and ternary hydrocarbon mixtures, *J. Chem. Phys.*, **132**, 114506, (2010).

[58] A. Königer, H. Wunderlich, W. Köhler, Measurement of diffusion and thermal diffusion in ternary fluid mixtures using a two-color optical beam deflection technique, *J. Chem. Phys.*, **132**, 174506, (2010).

[59] M. Gebhardt, W. Köhler, What can be learned from optical two-color diffusion and thermodiffusion experiments on ternary fluid mixtures?, *J. Chem. Phys.*, **142**, 084506, (2015).

[60] K. B. Haugen, A. Firoozabadi, On measurement of molecular and thermal diffusion coefficients in multicomponent mixtures, *J. Phys. Chem. B*, **110**, 17678–17682, (2006).

[61] A. Mialdun, J. C. Legros, V. Yasnou, V. Sechenyh, V. Shevtsova, Contribution to the benchmark for ternary mixtures: Measurement of the Soret, diffusion and thermodiffusion

coefficients in the ternary mixture THN/IBB/*n*C12 with 0.8/0.1/0.1 mass fractions in ground and orbital laboratories, *Eur. Phys. J. E*, **38**, 27, (2015).

[62] M. M. Bou-Ali, A. Ahadi, D. Alonso de Mezquia, Q. Galand, M. Gebhardt, O. Khlybov, W. Köhler, M. Larrañaga, J. C. Legros, T. Lyubimova, A. Mialdun, I. Ryzhkov, M. Z. Saghir, V. Shevtsova, S. Van Vaerenbergh, Benchmark values for the Soret, thermodiffusion and molecular diffusion coefficients of the ternary mixture tetralin+isobutylbenzene+*n*-dodecane with 0.8-0.1-0.1 mass fraction, *Eur. Phys. J. E*, **38**, 30, (2015).

[63] A. Mialdun, C. Minetti, Y, Gaponenko, V. Shevtsova, F. Dubois, Analysis of the thermal performance of SODI instrument for DCMIX configuration, *Microgravity Sci. Technol.*, **25**, 83–94, (2013).

[64] T. Triller, H. Bataller, M. M. Bou-Ali, M. Braibanti, F. Croccolo, J. M. Ezquerro, Q. Galand, Jna. Gavaldà, E. Lapeira, A. Laverón-Simavilla, T. Lyubimova, A. Mialdun, J. M. Ortiz de Zárate, J. Rodríguez, X. Ruiz, I. I. Ryzhkov, V. Shevtsova, S. Van Vaerenbergh, W. Köhler, Thermodiffusion in Ternary Mixtures of Water/Ethanol/Triethylene Glycol: First Report on the DCMIX3-Experiments Performed on the International Space Station, *Microgravity Sci. Technol.*, **30**, 295–308, (2018).

[65] M. Gebhardt, W. Köhler, Contribution to the benchmark for ternary mixtures: Measurement of the Soret and thermodiffusion coefficients of tetralin+isobutylbenzene+*n*-dodecane at a composition of (0.8/0.1/0.1) mass fractions by two-color optical beam deflection, *Eur. Phys. J. E*, **38**, 24, (2015).

[66] M. Larrañaga, M. M. Bou-Ali, D. Alonso de Mezquía, D. A. S. Rees, J. A. Madariaga, C. Santamaría, J. K. Platten, Contribution to the benchmark for ternary mixtures: Determination of Soret coefficients by the thermogravitational and the sliding symmetric tubes techniques, *Eur. Phys. J. E*, **38**, 28, (2015).

[67] Q. Galand, S. Van Vaerenbergh, Contribution to the benchmark for ternary mixtures: Measurement of diffusion and Soret coefficients of ternary system tetrahydronaphtalene–isobutylbenzene–*n*-dodecane with mass fractions 80-10-10 at 25 °C, *Eur. Phys. J. E*, **38**, 26, (2015).

[68] O. A. Khlybov, I. I. Ryzhkov, T. P. Lyubimova, Contribution to the benchmark for ternary mixtures: Measurement of diffusion and Soret coefficients in 1,2,3,4-tetrahydronaphthalene, isobutylbenzene, and dodecane onboard the ISS, *Eur. Phys. J. E*, **38**, 29, (2015).

[69] A. Ahadi, M .Z. Saghir, Contribution to the benchmark for ternary mixtures: Transient analysis in microgravity conditions, *Eur. Phys. J. E*, **38**, 25, (2015).

[70] M. Larrañaga, M. M. Bou-Ali, I. Lozarraga, J. A. Madariaga, C. Santamaría, Soret coefficients of the ternary mixture 1,2,3,4-tetrahydronaphthalene + isobutylbenzene + *n*-dodecane, *J. Chem. Phys.*, **143**, 024202, (2015).

[71] M. Gebhardt, W. Köhler, Soret, thermodiffusion, and mean diffusion coefficients of the ternary mixture *n*-dodecane+isobutylbenzene+1,2,3,4-tetrahydronaphthalene, *J. Chem. Phys.*, **143**, 164511, (2015).

[72] L. Onsager, Reciprocal relations in irreversible processes. I, *Phys. Rev.*, **37**, 405–426, (1931).

[73] L. Onsager, Reciprocal relations in irreversible processes. II, *Phys. Rev.*, **38**, 2265–2279, (1931).

[74] S. Chapman, F. W. Dootson, A note on thermal diffusion, *Philos. Mag.*, **33**, 248–253, (1917).

[75] M. E. Schimpf, in *Thermal Nonequilibrium Phenomena in Fluid Mixtures*, edited by W. Köhler, S. Wiegand (Springer, Berlin, 2002), pp. 285–312.

[76] J. Schirdewahn, A. Klemm, L. Waldmann, Thermodiffusion in D_2-HT und anderen Wasserstoffgemischen, *Z. Naturforsch. A*, **16**, 133–144, (1961).

[77] S. Iacopini, R. Piazza, Thermophoresis in protein solutions, *Europhys. Lett.*, **63**, 247–253, (2003).

[78] I. Prigogine, L. de Brouckère, R. Amand, Recherches sur la thermodiffusion en phase liquid, *Physica*, **16**, 851–860, (1950).

[79] F. Brochard, P. G. de Gennes, Soret effect of flexible macromolecules, *C. R. Acad. Sci. Paris, Ser. 2*, **293**, 1025–1027, (1981).

[80] P. Costesèque, D. Fargue, P. Jamet, in *Thermal Nonequilibrium Phenomena in Fluid Mixtures*, edited by W. Köhler, S. Wiegand (Springer, Berlin, 2002), pp. 389–427.

[81] W. H. Furry, R. C. Jones, L. Onsager, On the theory of isotope separation by thermal diffusion, *Phys. Rev.*, **55**, 1083–1095, (1939).

[82] M. M. Bou-Ali, O. Ecenarro, J. A. Madariaga, C. M. Santamaria, J. J. Valencia, Measurement of negative Soret coefficients in a vertical fluid layer with an adverse density gradient, *Phys. Rev. E*, **62**, 1420, (2000).

[83] C. C. Tanner, The Soret effect. Part I., *Trans. Faraday Soc.*, **23**, 75–95, (1927).

[84] C. C. Tanner, The Soret effect. Part II., *Trans. Faraday Soc.*, **49**, 611–619, (1953).

[85] K. B. Haugen, A. Firoozabadi, On the unsteady-state species separation of a binary liquid mixture in a rectangular thermogravitational column, *J. Chem. Phys.*, **124**, 054502, (2006).

[86] A. Becker, W. Köhler, B. Müller, A Scanning Michelson Interferometer for the Measurement of the Concentration and Temperature Derivative of the Refractive Index of Liquids, *Ber. Bunsenges*, *Phys. Chem.*, **99**, 600–608, (1995).

[87] A. Mialdun, V. Shevtsova, Development of optical digital interferometry technique for measurement of thermodiffusion coefficients, *Int. J. Heat Mass Transfer*, **51**, 3164–3178, (2008).

[88] F. A. Messaud, R. D. Sanderson, J. R. Runyon, T. Otte, H. Pasch, S. K. R. Williams, An overview on field-flow fractionation techniques and their applications in the separation and characterization of polymers, *Prog. Polym. Sci.*, **34**, 351–368, (2009).

[89] C. Giddings, A new separation concept based on a coupling of concentration and flow nonuniformities, *Sep. Sci.*, **1**, 123–125, (1966).

[90] P. N. Segrè, R. W. Gammon, and J. V. Sengers, Light-scattering measurements of nonequilibrium fluctuations in a liquid mixture, *Phys. Rev. E*, **47**, 1026–1034, (1993).

[91] H. Bataller, C. Giraudet, F. Croccolo, J. M. Ortiz de Zárate, Analysis of Non-Equilibrium Fluctuations In A Ternary Liquid Mixture, *Microgravity Sci. Technol.*, **28**, 611–619, (2016).

[92] J. M. Ortiz de Zárate, C. Giraudet, H. Bataller, F. Croccolo, Non-equilibrium fluctuations induced by the Soret effect in a ternary mixture, *Eur. Phys. J. E*, **37**, 34, (2014).

[93] H. Bataller, T. Triller, B. Pur, W. Köhler, J. M. Ortiz de Zárate, F. Croccolo, Dynamic analysis of the light scattered by the non-equilibrium fluctuations of a ternary mixture of polystyrene-toluene-*n*-hexane, *Eur. Phys. J. E*, **40**, 35, (2017).

[94] P. Polyakov, S. Wiegand, Investigation of the Soret effect in aqueous and non-aqueous mixtures by the thermal lens technique, *Phys. Chem. Chem. Phys.*, **11**, 864–871, (2009).

[95] A. P. Fröba, S. Will, Y. Nagasaka, J. Winkelmann, S. Wiegand, W. Köhler, in *Experimental Thermodynamics Volume IX: Advances in Transport Properties of Fluids*, edited by M. J. Assael, A. R. H. Goodwin, V. Vesovic, W. A. Wakeham, (Royal Society of Chemistry, Chembridge, 2014), pp. 19–74.

[96] C. A. Carter, J. M. Harris, Comparison of models describing the thermal lens effect, *Appl. Opt.*, **23**, 476–481, (1984).

[97] A. Voit, Ph.D. thersis, University Bayreuth, (2003).

[98] R. Rusconi, L. Isa, R. Piazza, Thermal-lensing measurement of particle thermophoresis in aqueous dispersions, *J. Opt. Soc. Am. B*, **21**, 605–616, (2004).

[99] H. J. Eichler, P. Günter, D. W. Pohl, *Laser-Induced Dynamic Gratings*, (Springer, Berlin, 1986).

[100] K. Thyagarajan, P. Lallemand, Determination of the thermal diffusion ratio in a binary mixture by forced Rayleigh scattering, *Opt. Commun.* **26**, 54–57, (1978).

[101] W. Köhler, Thermodiffusion in polymer solutions as observed by forced Rayleigh scattering, *J. Chem. Phys.*, **98**, 660–668, (1993).

[102] W. Köhler, P. Rossmanith, Aspects of thermal diffusion forced Rayleigh scattering: heterodyne detection, active phase tracking and experimental constraints, *J. Phys. Chem.*, **99**, 5838–5847, (1995).

[103] S.Wiegand, W.Köhler, in *Thermal Nonequilibrium Phenomena in Fluid Mixtures*, edited by W. Köhler, S. Wiegand (Springer, Berlin, 2002), pp. 189–210.

[104] S. Wiegand, H. Ning, H. Kriegs, Thermal diffusion forced Rayleigh scattering setup optimized for aqueous mixtures, *J. Phys. Chem. B*, **111**, 14169–14174, (2007).

[105] M. Gebhardt, Ph.D. Thesis, Universität Bayreuth, (2015).

[106] J. Rauch, W. Köhler, Diffusion and thermal diffusion of semidilute to concentrated solutions of polystyrene in toluene in the vicinity of the glass transition, *Phys. Rev. Lett.*, **88**, 185901, (2002).

[107] J. Rauch, W. Köhler, Collective and thermal diffusion in dilute, semidilute, and concentrated solutions of polystyrene in toluene, *J. Chem. Phys.*, **119**, 11977, (2003).

[108] W. Enge, W. Köhler, Thermal diffusion in a critical polymer blend, *Phys. Chem. Chem. Phys.*, **6**, 2373–2378, (2004).

[109] W. Enge, W. Köhler, Correlation between the Soret coefficient and the static structure factor in a polymer blend, *Eur. Phys. J. E*, **15**, 265–270, (2004).

[110] W. Köhler, A. Krekhov, W. Zimmermann, Thermal diffusion in polymer blends: Criticality and pattern formation, *Adv. Polym. Sci.*, **227**, 145–198, (2010).

[111] H. Ning, R. Kita, H. Kriegs, J. Luettmer-Strathmann, S. Wiegand, Thermal diffusion behavior of nonionic surfactants in water, *J. Phys. Chem. B*, **110**, 10746–10756, (2006).

[112] Y. Kishikawa, H. Shinohara, K. Maeda, Y. Nakamura, S. Wiegand, R. Kita, *Phys. Chem. Chem. Phys.*, **14**, 10147–10153, (2012).

[113] K. Maeda, N. Shinyashiki, S. Yagihara, S. Wiegand, R. Kita, Temperature dependence of thermal diffusion for aqueous solutions of monosaccharides, oligosaccharides, and polysaccharides, *Eur. Phys. J. E*, **37**, 94, (2014).

[114] Z. Wang, D. Afanasenkau, M. Dong, D. Huang, S. Wiegand, Molar mass and temperature dependence of the thermodiffusion of polyethylene oxide in water/ethanol mixtures, *J. Chem. Phys.*, **141**, 064904, (2014).

[115] K. Maeda, N. Shinyashiki, S. Yagihara, S. Wiegand, R. Kita, Ludwig-Soret effect of aqueous solutions of ethylene glycol oligomers, crown ethers, and glycerol: temperature, molecular weight, and hydrogen bond effect, *J. Chem. Phys.*, **143**, 124504, (2015).

[116] O. Syshchyk, D. Afanasenkau, Z. Wang, H. Kriegs, J. Buitenhuis, S. Wiegand, Influence of temperature and charge effects on thermophoresis of polystyrene beads, *Eur. Phys. J. E*, **39**, (2016).

[117] D. Niether, T. Kawaguchi, J. Hovancová, K. Eguchi, J. K. G. Dhont, R. Kita, S. Wiegand, Role of Hydrogen Bonding of Cyclodextrin−Drug Complexes Probed by Thermodiffusion, *Langmuir*, **33**, 8483–8492, (2017).

[118] D. Niether, S. Di Lecce, F. Bresme, S. Wiegand, Unravelling the hydrophobicity of urea in water using thermodiffusion: implications for protein denaturation, *Phys. Chem. Chem. Phys.*, **20**, 1012–1020, (2018).

[119] D. Niether, M. Sarter, B. König, M. Zamponi, J. Fitter, A. Stadler, S. Wiegand, Thermodiffusion as a probe of protein hydration for streptavidin and the streptavidin-biotin complex, *AIP Conf. Proc.*, **1929**, 020001, (2018).

[120] A. Sehnem, D. Niether, S. Wiegand, A. M. F. Neto, Thermodiffusion of Monovalent Organic Salts in Water, *J. Phys. Chem. B*, **122**, 4093–4100, (2018).

[121] A. Königer, Ph.D. thesis, Universität Bayreuth, (2012).

[122] K. Hayashida, Y. Nagasaka, Measurement of Mutual Diffusion Coefficient by the Soret Forced Rayleigh Scattering Method: 1st Report, Examination of the Method and Measurement of Polymer Solutions, *Trans. Jpn. Soc. Mech. Eng. B*, **63**, 276–281, (1997). (in Japanese)

[123] Y. Yamamoto, Y. Nagasaka, Development of the Soret Forced Rayleigh Scattering Method for Measurement of Mass Diffusion Coefficient 1st Report, Development of the Measurement System and Measurement of the Fullerene in Solution, *Trans. Jpn. Soc. Mech.*

Eng. B, **72**, 709–714, (2006). (in Japanese)

[124] Y. Yamamoto, Y. Nagasaka, Measurement of Mass Diffusion Coefficient by the Soret Forced Rayleigh Scattering Method 2nd Report, Theoretical Analysis of Systematic Effectof Experimental Parameters, *Trans. Jpn. Soc. Mech. Eng. B*, **72**, 715–722, (2006). (in Japanese)

[125] M. Niwa, Y. Ohta, Y. Nagasaka, Mass Diffusion Coefficients of Cellulose Acetate Butyrate in Methyl Ethyl Ketone Solutions at Temperatures between (293 and 323) K and Mass Fractions from 0.05 to 0.60 Using the Soret Forced Rayleigh Scattering Method, *J. Chem. Eng. Data*, **54**, 2708–2714, (2009).

[126] Y. Nagasaka, T. Hatakeyama, M. Okuda, A. Nagashima, Measurement of the thermal diffusivity of liquids by the forced Rayleigh scattering method: Theory and experiment, *Rev. Sci. Instrum.*, **59**, 1156−1168, (1988).

[127] Y. Matsushita, T. Sato, T. Kanaya, K. Ito, H. Watanabe, K. Tanaka, T. Shimomura, T. Inoue, *Structures and physical properties of polymers* (Kodansha, Tokyo, 2013). (in Japanese)

[128] K. J. Edgar, C. M. Buchanan, J. S. Debenham, P. A. Rundquist, B. D. Seiler, M. C. Shelton, D. Tindall, Advances in cellulose ester performance and application, *Prog. Polym. Sci.*, **26**, 1605–1688, (2001).

[129] K. Oki, Y. Nagasaka, Dynamic Observation of the Behavior of the Surface of Liquid Films of Polymer–Organic Solvent System by Ripplon Surface Laser-Light Scattering Method, *Kagaku Kogaku Ronbun.*, **34**, 587–593, (2008). (in Japanese)

[130] ISO/IEC Guide 98-3:2008, *Uncertainty of Measurement—Part 3: Guide to the Expression of Uncertainty in Measurement (GUM:1995)* (International Organization for Standardization, Geneva, 2008).

[131] Y. Yamamoto, Ph.D. Thesis, Keio University, (2006).

[132] H. Fujita, L. J. Gosting, A new procedure for calculating the four diffusion coefficients of three-component systems from Gouy diffusiometer data, *J. Phys. Chem.*, **64**, 1256–1263, (1960).

[133] D. G. Miller, A Method for Obtaining Multicomponent Diffusion Coefficients Directly from Rayleigh and Gouy Fringe Position Data, *J. Phys. Chem.*, **92**, 4222–4226, (1988).

[134] V. Sechenyh, J. C. Legros, A. Mialdun, J. M. Ortiz de Zárate, V. Shevtsova, Fickian Diffusion in Ternary Mixtures Composed by 1,2,3,4-Tetrahydronaphthalene,

Isobutylbenzene, and *n*-Dodecane, *J. Phys. Chem. B*, **120**, 535–548, (2016).

[135] V. Shevtsova, V. Sechenyh, A. Nepomnyashchy, J. C. Legros, Analysis of the application of optical two-wavelength techniques to measurement of the Soret coefficients in ternary mixtures, *Philos. Mag.*, **91**, 3498–3518, (2011).

[136] A. Mialdun, Shevtsova, Analysis of multi-wavelength measurements of diffusive properties via dispersion dependence of optical properties, *Appl. Opt.*, **56**, 572–581, (2017).

[137] National Research Council, *Oil in the Sea: Inputs, Fates, and Effects* (National Academy Press, Washington, D.C., 1985).

[138] M. Gebhardt, W. Köhler, A. Mialdun, V. Yasnou, V. Shevtsova, Diffusion, thermal diffusion, and Soret coefficients and optical contrast factors of the binary mixtures of dodecane, isobutylbenzene, and 1,2,3,4-tetrahydronaphthalene, *J. Chem. Phys.*, **138**, 114503 (2013).

[139] V. V. Sechenyh, J. C. Legros, V. Shevtsova, Optical properties of binary and ternary liquid mixtures containing tetralin,isobutylbenzene and dodecane, *J. Chem. Thermodyn.*, **62**, 64−68, (2013).

[140] Allan F. M. Barton, *CRC Handbook of Solubility Parameters and Other Cohesion Parameters: Second Edition*, (CRC Press, Boca Raton, 1991).

[141] R. Kita, P. Polyakov, S. Wiegand, Ludwig-Soret Effect of Poly(N-isopropylacrylamide): Temperature Dependence Study in Monohydric Alcohols, *Macromolecules*, **40**, 1638−1642, (2007).

[142] M. H. V. Mulder, F. Kruitz, C. A. Smolders, Separation of isomeric xylenes by pervaporation through cellulose ester membranes, *J. Memb. Sci*., **11**, 349−363, (1982).

[143] T. Sakai, J. Hotta, Y. Nagasaka, Development of measurement technique for mass diffusion coefficient of methanol aqueous solutions in polymer electrolyte membrane for fuel cell by Soret forced Rayleigh scattering, *Netsu Bussei*, **26**, 196–202, (2012) (in Japanese).

[144] W. R. Klein, B. D. Cook, Unified approach to ultrasonic light diffraction, *IEEE Trans. Sonic Ultrason*., **14**, 123–134, (1967).

[145] A. Kusoglu, A. Z. Weber, New Insights into Perfluorinated Sulfonic-Acid Ionomers, *Chem. Rev.*, **117**, 987−1104, (2017).

Appendix

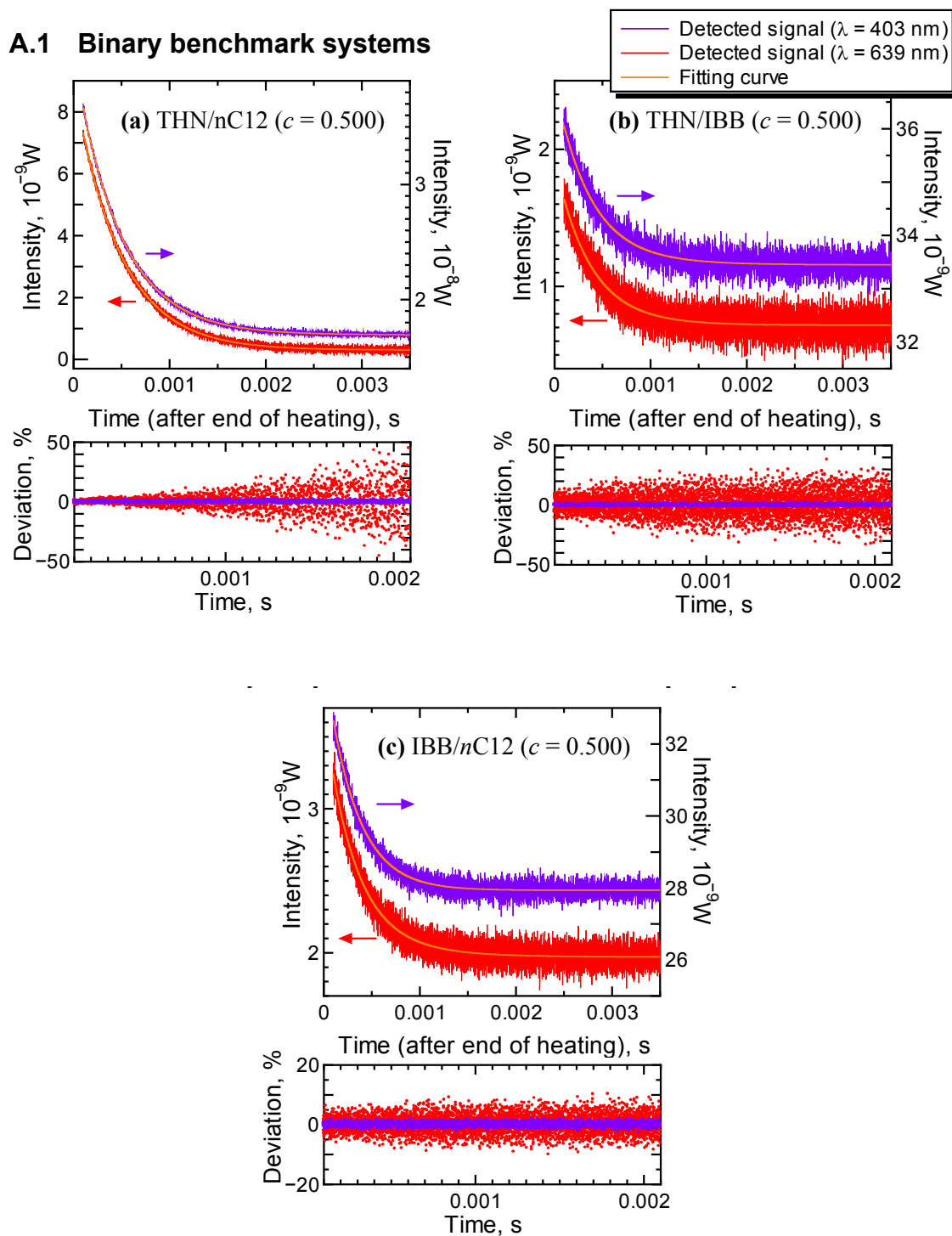## A.1 Binary benchmark systems

Figure A.1: Mass diffusion signals and fitting curves of the binary benchmark mixtures at $T = 298.2$ K.
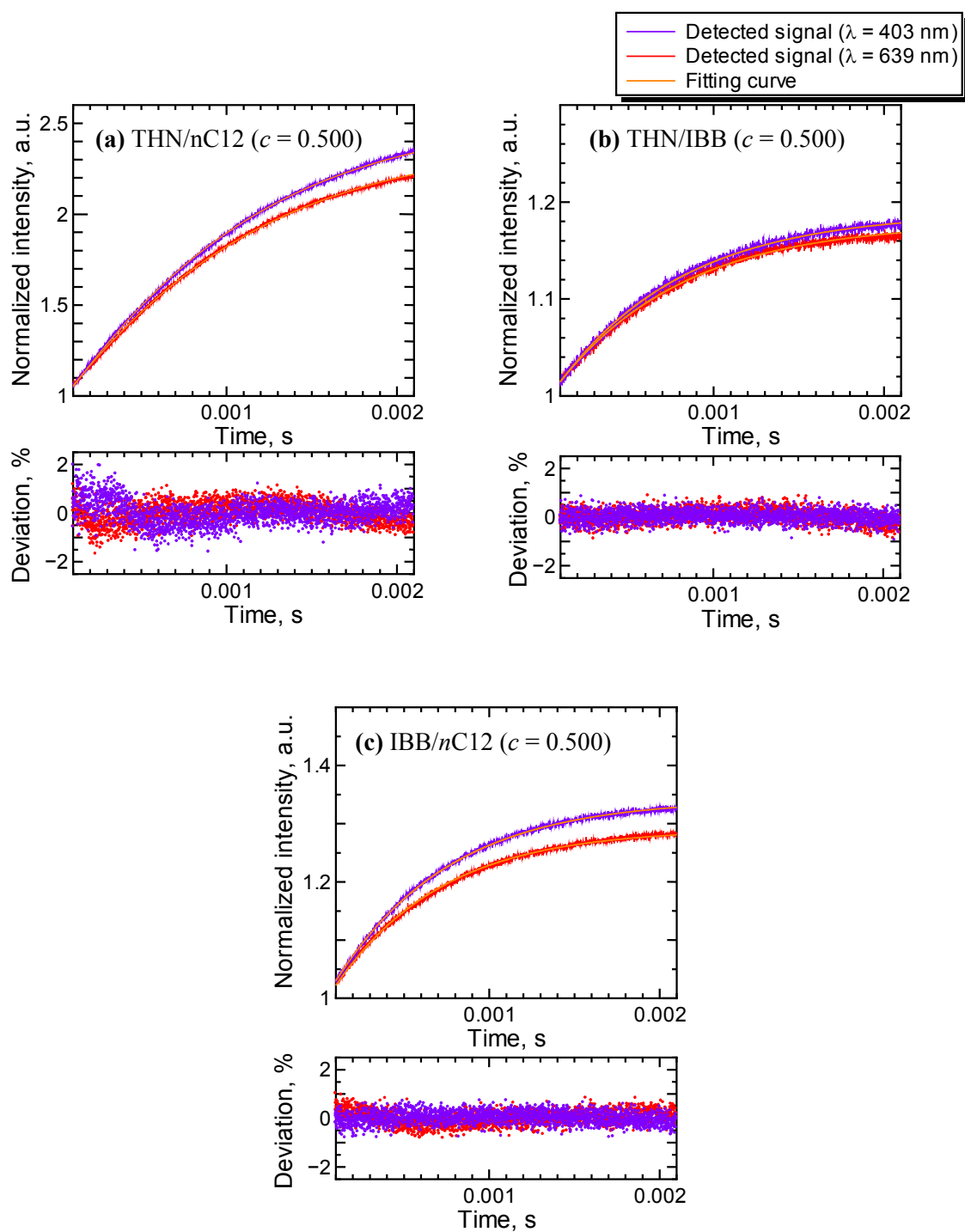
Figure A.2: Soret effect signals and fitting curves of the binary benchmark mixtures at $T = 298.2$ K.

Table A.1: Uncertainty budgets for the mass diffusion coefficient in measurement of the binary benchmark mixtures ($c = 0.500$) by the probing laser of $\lambda = 639$ nm at $T = 298.2$ K.

Sample	Uncertainty element x_i	Value of x_i	$u(x_i)$	Sensitivity coefficient $\lvert c_D \rvert$	Contribution to uncertainty of D $\lvert c_D \rvert \times u(x_i)$, 10^{-10} m^{2}s^{-1}
THN/ nC12	τ_D	9.43×10^{-4} s	2.45×10^{-6} s	6.99×10^{-7}	0.017
	Λ	4.96×10^{-6} m	9.32×10^{-6} m	2.66×10^{-4}	0.025
					$u(D) = 0.03 \times 10^{-10}$ m^{2}s^{-1}
THN /IBB	τ_D	7.54×10^{-4} s	7.88×10^{-6} s	1.10×10^{-6}	0.086
	Λ	4.96×10^{-6} m	9.32×10^{-6} m	3.33×10^{-4}	0.031
					$u(D) = 0.09 \times 10^{-10}$ m^{2}s^{-1}
IBB/ nC12	τ_D	6.22×10^{-4} s	2.66×10^{-6} s	1.59×10^{-6}	0.042
	Λ	4.93×10^{-6} m	9.32×10^{-6} m	4.01×10^{-4}	0.037
					$u(D) = 0.06 \times 10^{-10}$ m^{2}s^{-1}

Table A.2: Uncertainty budgets for the Soret coefficient in measurement of the binary benchmark mixtures ($c = 0.500$) by the probing laser of $\lambda = 639$ nm at $T = 298.2$ K

Sample	Uncertainty element x_i	Value of x_i	$u(x_i)$	Sensitivity coefficient $\lvert c_S \rvert$	Contribution to uncertainty of S_T $\lvert c_S \rvert \times u(x_i)$, 10^{-3}K^{-1}
THN/ nC12	Γ	-0.599	2.38×10^{-3}	1.54×10^{-2}	0.037
	$\partial n_\lambda/\partial c$	0.1155	0.0004	7.98×10^{-2}	0.032
	$\partial n_\lambda/\partial T$	-4.44×10^{-4} K^{-1}	0.02×10^{-4} K^{-1}	20.7	0.041
					$u(S_T) = 0.06 \times 10^{-3}$ K^{-1}
THN/ IBB	Γ	-0.0889	3.35×10^{-4}	3.50×10^{-2}	0.012
	$\partial n_\lambda/\partial c$	0.0547	0.0004	5.68×10^{-2}	0.023
	$\partial n_\lambda/\partial T$	-4.78×10^{-4} K^{-1}	0.02×10^{-4} K^{-1}	6.50	0.013
					$u(S_T) = 0.03 \times 10^{-3}$ K^{-1}
IBB/nC 12	Γ	-0.133	4.85×10^{-4}	2.92×10^{-2}	0.014
	$\partial n_\lambda/\partial c$	0.0625	0.0004	6.21×10^{-2}	0.025
	$\partial n_\lambda/\partial T$	-4.56×10^{-4} K^{-1}	0.02×10^{-4} K^{-1}	8.51	0.017
					$u(S_T) = 0.03 \times 10^{-3}$ K^{-1}

A2. Measurement of ternary benchmark systems

Table A.3: Uncertainty budgets for the Soret coefficient and thermodiffusion coefficient of n-dodecane (nC12) in measurement of the ternary benchmark mixture of nC12/THN/IBB with mass fraction $c_1 = c_{n\text{C}12} = 0.100$ and $c_2 = c_{\text{THN}} = 0.800$ at $T = 298.2$ K.

Uncertainty element x_i	Value of x_i	$u(x_i)$	Sensitivity coefficient to $S'_{T,n\text{C}12}$ $c_{S,i}$[a]	Contribution to uncertainty of $S'_{T,n\text{C}12}$ $\|c_{S,i}\| \times u(x_i)$, 10^{-3} K^{-1}	Sensitivity coefficient to $D'_{T,n\text{C}12}$ $c_{T,i}$	Contribution to uncertainty of $D'_{T,n\text{C}12}$ $\|c_{T,i}\| \times u(x_i)$, 10^{-12} m^{2}s^{-1}K^{-1}
$\partial n_{405}/\partial c_1$	-0.1059 [65]	0.0004 [33]	-0.089	0.04	-5.85×10^{-11}	0.02
$\partial n_{405}/\partial c_2$	0.0609 [65]	0.0004 [33]	0.125	0.05	6.88×10^{-11}	0.03
$\partial n_{633}/\partial c_1$	-0.0881 [65]	0.0004 [33]	0.098	0.04	6.42×10^{-11}	0.03
$\partial n_{633}/\partial c_2$	0.0555 [65]	0.0004 [33]	-0.137	0.05	-7.55×10^{-11}	0.03
$P'_{S,\lambda}$	1.58×10^{-4} (K^{-1})	0.009×10^{-4} (K^{-1})	-108	0.09	–	–
$P'_{S,\lambda}$	1.37×10^{-4} (K^{-1})	0.007×10^{-4} (K^{-1})	119	0.08	–	–
$P'_{T,\lambda}$	9.59×10^{-14} (m^{2}s^{-1}K^{-1})	0.07×10^{-14} (m^{2}s^{-1}K^{-1})	–	–	-108	0.07
$P'_{T,\lambda}$	8.28×10^{-14} (m^{2}s^{-1}K^{-1})	0.06×10^{-14} (m^{2}s^{-1}K^{-1})	–	–	119	0.07
			$u_c(S'_{T,n\text{C}12})$	0.16	$u_c(D'_{T,n\text{C}12})$	0.11

[a]The sensitivity coefficient $c_{S,i}$ denotes $\partial f_S/\partial x_i$ in Eq. (3.7) with the uncertainty element x_i.

Table A.4: Uncertainty budgets for the Soret coefficient and thermodiffusion coefficient of isobutylbenzene (IBB) in measurement of the ternary benchmark mixture of nC12/THN/IBB with mass fraction $c_1 = c_{n\text{C}12} = 0.100$ and $c_2 = c_{\text{THN}} = 0.800$ at $T = 298.2$ K.

Uncertainty element x_i	Value of x_i	$u(x_i)$	Sensitivity coefficient to $S'_{T,\text{IBB}}$ $c_{S,i}$[a]	Contribution to uncertainty of $S'_{T,\text{IBB}}$ $\lvert c_{S,i} \rvert \times u(x_i)$, 10^{-3} K^{-1}	Sensitivity coefficient to $D'_{T,\text{IBB}}$ $c_{T,i}$	Contribution to uncertainty of $D'_{T,\text{IBB}}$ $\lvert c_{T,i} \rvert \times u(x_i)$, 10^{-12} m^{2}s^{-1}K^{-1}
$S'_{T,n\text{C}12}$	-0.83×10^{-3} (K^{-1})	0.16×10^{-3} (K^{-1})	1	0.16	–	–
$S'_{T,\text{THN}}$	1.14×10^{-3} (K^{-1})	0.26×10^{-3} (K^{-1})	1	0.26	–	–
$D'_{T,n\text{C}12}$	-0.54×10^{-12} (m^{2}s^{-1}K^{-1})	0.11×10^{-12} (m^{2}s^{-1}K^{-1})	–	–	1	0.11
$D'_{T,\text{THN}}$	0.64×10^{-12} (m^{2}s^{-1}K^{-1})	0.19×10^{-12} (m^{2}s^{-1}K^{-1})	–	–	1	0.19
			$u_c(S'_{T,\text{IBB}})$	0.30	$u_c(D'_{T,\text{IBB}})$	0.22

[a]The sensitivity coefficient $c_{S,i}$ denotes $\partial f_S/\partial x_i$ in Eq. (3.7) with the uncertainty element x_i.

A3. Measurement of refractive indecus of ternary polymer solutions

Table A.5: Refractive induces of CAB/styrene/2-butanone measured at $T = 298.2$ K.

c_{CAB}	$c_{styrene}$	$c_{2\text{-butanone}}$	$\lambda =$ 401 nm	$\lambda =$ 633 nm	c_{CAB}	$c_{styrene}$	$c_{2\text{-butanone}}$	$\lambda =$ 401 nm	$\lambda =$ 633 nm
0	0.000	1.000	1.3895	1.3753	0.100	0	0.900	1.3962	1.3826
0	0.100	0.900	1.4078	1.3899	0.100	0.100	0.800	1.4160	1.3987
0	0.200	0.800	1.4270	1.4062	0.100	0.200	0.700	1.4361	1.4150
0	0.300	0.700	1.4457	1.4212	0.100	0.300	0.600	1.4571	1.4317
0	0.400	0.600	1.4663	1.4383	0.100	0.399	0.501	1.4772	1.4486
0	0.500	0.500	1.4866	1.4538	0.100	0.500	0.400	1.4987	1.4654
0	0.600	0.400	1.5061	1.4704	0.100	0.600	0.300	1.5188	1.4823
0	0.700	0.300	1.5265	1.4863	0.100	0.700	0.200	1.5413	1.5000
0	0.800	0.200	1.5487	1.5049	0.100	0.800	0.100	1.5631	1.5174
0	0.900	0.100	1.5694	1.5213	0.100	0.900	0	1.5837	1.5337
0	1.000	0	1.5908	1.5386	0.150	0.000	0.850	1.4011	1.3868
0.050	0.000	0.950	1.3917	1.3783	0.150	0.100	0.750	1.4210	1.4036
0.050	0.100	0.850	1.4115	1.3944	0.150	0.200	0.650	1.4411	1.4197
0.050	0.200	0.750	1.4305	1.4099	0.150	0.300	0.550	1.4625	1.4370
0.050	0.300	0.650	1.4509	1.4264	0.150	0.400	0.450	1.4831	1.4537
0.050	0.400	0.550	1.4719	1.4432	0.150	0.500	0.350	1.5048	1.4711
0.050	0.500	0.450	1.4922	1.4595	0.150	0.600	0.250	1.5259	1.4882
0.050	0.600	0.350	1.5133	1.4766	0.150	0.700	0.150	1.5479	1.5055
0.050	0.700	0.250	1.5349	1.4940	0.150	0.800	0.050	1.5693	1.5230
0.050	0.800	0.150	1.5560	1.5106	0.150	0.850	0	1.5794	1.5311
0.050	0.950	0.00	1.5877	1.5364	0.20	0.00	0.80	1.4059	1.3918

Table A.5: continued.

c_{CAB}	$c_{styrene}$	$c_{2\text{-butanone}}$	$\lambda =$ 401 nm	$\lambda =$ 633 nm	c_{CAB}	$c_{styrene}$	$c_{2\text{-butanone}}$	$\lambda =$ 401 nm	$\lambda =$ 633 nm
0.200	0.100	0.70	1.4273	1.4092	0.25	0.50	0.25	1.5200	1.4850
0.200	0.200	0.60	1.4473	1.4254	0.25	0.60	0.15	1.5409	1.5019
0.200	0.300	0.50	1.4681	1.4423	0.25	0.70	0.05	1.5623	1.5192
0.200	0.400	0.40	1.4911	1.4607	0.25	0.75	0.00	1.5727	1.5270
0.200	0.5000	0.30	1.5115	1.4776	0.30	0.00	0.70	1.4180	1.4037
0.200	0.600	0.20	1.5327	1.4944	0.30	0.10	0.60	1.4386	1.4201
0.200	0.7000	0.10	1.5545	1.5120	0.30	0.20	0.50	1.4609	1.4382
0.200	0.800	0.00	1.5761	1.5292	0.30	0.30	0.40	1.4838	1.4571
0.250	0.000	0.75	1.4111	1.3967	0.30	0.40	0.30	1.5048	1.4738
0.250	0.100	0.65	1.4320	1.4142	0.30	0.50	0.20	1.5257	1.4906
0.250	0.200	0.55	1.4555	1.4335	0.30	0.60	0.10	1.5465	1.5076
0.250	0.300	0.45	1.4780	1.4503	0.30	0.70	0.00	1.5661	1.5230
0.250	0.400	0.35	1.4977	1.4670	–	–	–	–	–
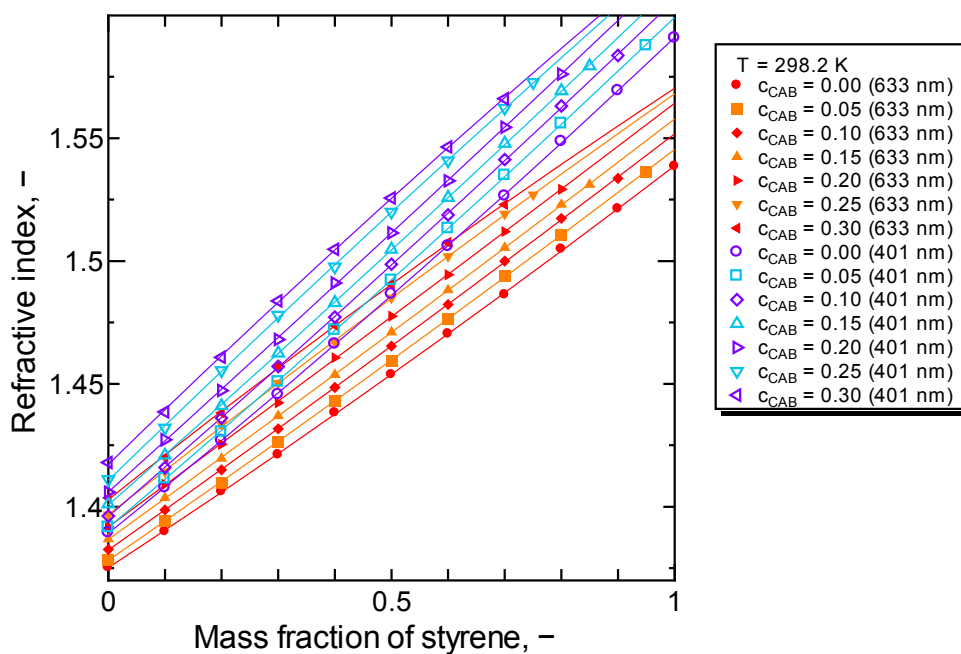
Figure A.3: Refractive index vs $c_{styrene}$ for CAB/styrene/2-butanone at $T = 298.2$ K (c_{CAB} is fixed).
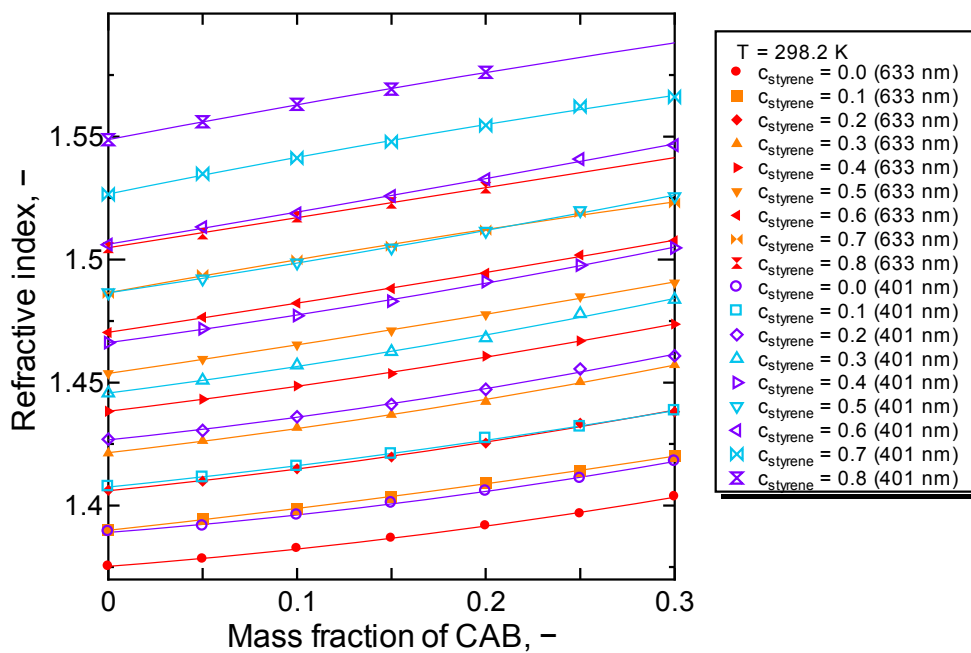
Figure A.4: Refractive index vs c_{CAB} for CAB/styrene/2-butanone at $T = 298.2$ K ($c_{styrene}$ is fixed).
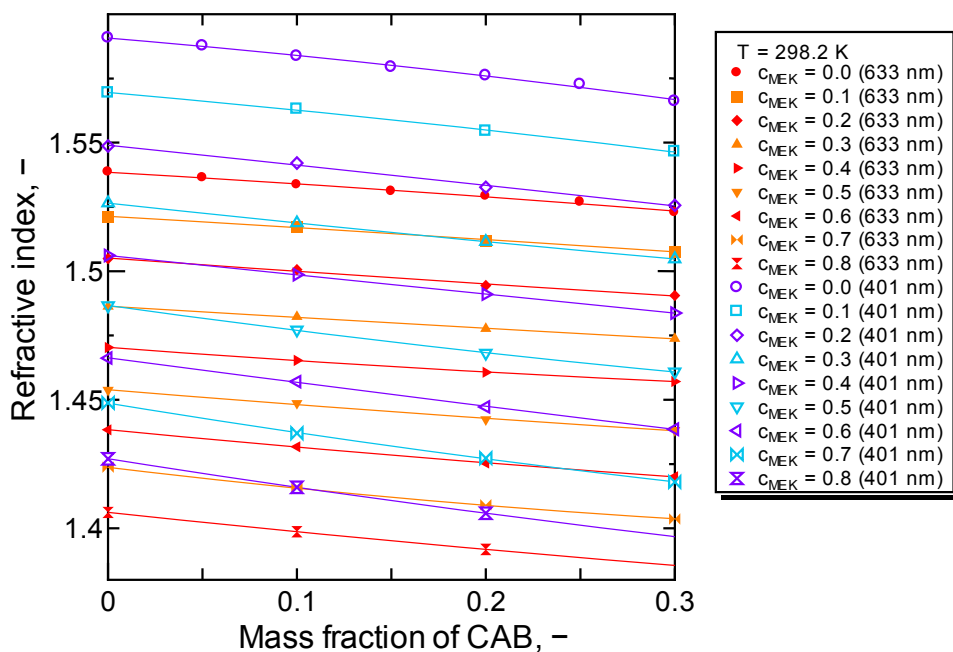

Figure A.5: Refractive index vs c_{CAB} for CAB/styrene/2-butanone at $T = 298.2$ K ($c_{2\text{-butanone}} = c_{MEK}$ is fixed).

Table A.6: Temperature dependence of refractive induces of CAB/styrene/2-butanone ($\lambda = 401$ nm).

			Temperature, K						
c_{CAB}	$c_{styrene}$	$c_{2\text{-butanone}}$	283.2	288.2	293.2	298.2	303.2	308.2	313.2
0.10	0	0.90	1.4041	1.4015	1.3991	1.3962	1.3935	1.3909	1.3880
0.10	0.10	0.80	1.4243	1.4217	1.4189	1.4160	1.4131	1.4108	1.4079
0.10	0.20	0.70	1.4446	1.4413	1.4387	1.4361	1.4337	1.4304	1.4279
0.10	0.30	0.60	1.4659	1.4622	1.4594	1.4571	1.4538	1.4507	1.4477
0.10	0.40	0.50	1.4866	1.4834	1.4798	1.4772	1.4744	1.4717	1.4687
0.10	0.50	0.40	1.5077	1.5036	1.5006	1.4987	1.4948	1.4921	1.4884
0.10	0.60	0.30	1.5286	1.5260	1.5222	1.5188	1.5167	1.5141	1.5113
0.10	0.70	0.20	1.5500	1.5470	1.5438	1.5413	1.5377	1.5349	1.5321
0.10	0.80	0.10	1.5718	1.5684	1.5656	1.5631	1.5598	1.5564	1.5534
0.10	0.90	0	1.5932	1.5898	1.5872	1.5837	1.5805	1.5775	1.5743

Table A.7: Temperature dependence of refractive induces of CAB/styrene/2-butanone ($\lambda = 633$ nm).

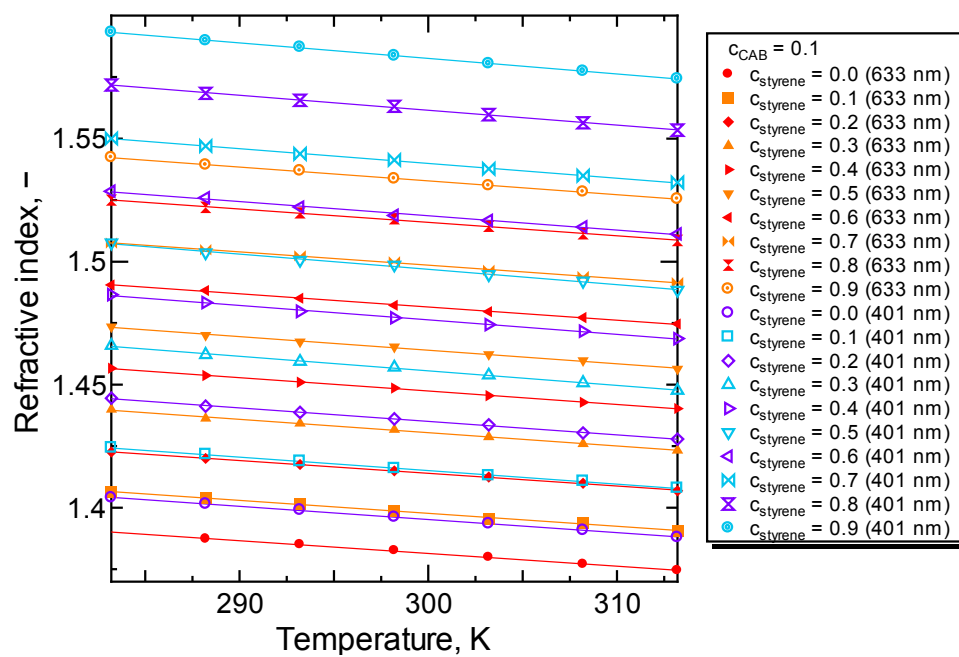|			Temperature, K						
c_{CAB}	$c_{styrene}$	$c_{2\text{-butanone}}$	283.2	288.2	293.2	298.2	303.2	308.2	313.2
0.10	0	0.90	–	1.3873	1.3851	1.3826	1.3798	1.3770	1.3745
0.10	0.10	0.80	1.4063	1.4040	1.4017	1.3987	1.3956	1.3937	1.3907
0.10	0.20	0.70	1.4226	1.4200	1.4176	1.4150	1.4125	1.4100	1.4068
0.10	0.30	0.60	1.4399	1.4363	1.4343	1.4317	1.4288	1.4260	1.4233
0.10	0.40	0.50	1.4567	1.4537	1.4510	1.4486	1.4455	1.4428	1.4403
0.10	0.50	0.40	1.4735	1.4701	1.4675	1.4654	1.4623	1.4599	1.4564
0.10	0.60	0.30	1.4905	1.4883	1.4851	1.4823	1.4797	1.4773	1.4747
0.10	0.70	0.20	1.5076	1.5049	1.5024	1.5000	1.4965	1.4940	1.4915
0.10	0.80	0.10	1.5250	1.5221	1.5198	1.5174	1.5144	1.5114	1.5086
0.10	0.90	0	1.5423	1.5393	1.5369	1.5337	1.5309	1.5283	1.5255

Figure A.6: Temperature dependence of refractive index of CAB/styrene/2-butanone (c_{CAB} = 0.10).